X-RAY DIFFRACTION USED IN OBSERVATION AND CHARACTERIZATION ON GUEST MOLECULES IN METAL-ORGANIC FRAMEWORKS

A Dissertation

by

YING-PIN CHEN

Submitted to the Office of Graduate and Professional Studies of
Texas A&M University
in partial fulfillment of the requirements for the degree of

DOCTOR OF PHILOSOPHY

Chair of Committee,	Hong-Cai Zhou
Committee Members,	Abraham Clearfield
	Perla Balbuena
	Hae-Kwon Jeong
Head of Department,	Ibrahim Karaman

May 2017

Major Subject: Materials Science and Engineering

ABSTRACT

Knowledge about the interactions between gas molecules and adsorption sites is essential to customize Metal Organic Frameworks (MOFs) as adsorbents. The dynamic interactions occurring during adsorption/desorption working cycles with several states are especially complicated. Even so, the gas dynamics based upon experimental observations and the distribution of guest molecules under various conditions in MOFs have not been extensively studied yet. In this work, a direct time-resolved diffraction structure envelope (TRDSE) method using sequential measurements by in situ synchrotron powder X-ray diffraction has been developed to monitor several gas dynamics processes taking place in MOFs: infusion, desorption, and gas redistribution on temperature change. The electron density maps indicate that gas molecules prefer to redistribute over heterogeneous types of sites rather than to exclusively occupy the primary binding sites. We found that the gas molecules are entropically driven from open metal sites to larger neighboring spaces during the gas infusion period, matching the localized-to-mobile mechanism. In addition, the partitioning ratio of molecules adsorbed at each site varies with different temperatures, as opposed to an invariant distribution mode. Equally important, the gas adsorption in MOFs is intensely influenced by the gas-gas interactions, which might induce more molecules to be accommodated in an orderly compact arrangement. This sequential TRDSE method is generally applicable to most crystalline adsorbents, yielding information on distribution ratios of adsorbates at each type of site.

DEDICATION

To my family and my friends

For their love and support

ACKNOWLEDGEMENTS

I would first like to thank my advisor, Dr. Hong-Cai Zhou for providing me with numerous excellent opportunities to train myself over these years. I would like to express my appreciation to my committee members, Dr. Perla Balbuena, and Dr. Hae-Kwon Jeong, Dr. Abraham Clearfield for strengthening my background in materials science. My gratitude is also extended to Dr. Joseph H. Reibenspies and Dr. Nattamai Bhuvanesh for instructing me in solving crystallography problems. Our department staff, Ms. Jan Gerston, Ms. Jules Henry, Ms. Lizzie West, Ms. Carrie Frederiksen have made my time at Texas A&M University a wonderful experience.

My fellow labmates have been incredible to work with. I would especially like to thank my mentor Andrey A. Yakovenko, who led me into the world of X-ray crystallography. Jinhee Park has been helpful in bouncing around ideas. Dr. Tian-Fu Liu, Yangyang Liu, Dr. Dahuan Liu, and Xuan Wang have aided me finish my projects efficiently. Stephen Fordham and Mathieu Bosch have polished my writing and oral skills. I am grateful to Dr. Qiang Zhang, Dr. Daqiang Yuan and Dawei Feng for insightful discussions.

Thanks also go to the collaborators in other institutes: Dr. Yu-Sheng Chen, Mr. Wenyang Gao and Dr. Gregory J. Halder in Argonne National Lab for setting up instruments for my gas-loading studies; Dr. Jinbo Liu and Dr. Sajid Bashir in Texas A&M University-Kingsville for guiding me to co-edit a book.

Finally, my friends deserve an acknowledgement for their companionship. You guys have been great during some very trying times in my life and have encouraged me to pursue my academic career.

CONTRIBUTORS AND FUNDING SOURCES

Contributors

This work was supervised by a dissertation committee consisting of Professor Hong-Cai Zhou [advisor], Professor Perla Balbuena, Professor Hae-Kwon Jeong of the Department of Materials Science and Engineering [Home Department] and Professor Abraham Clearfield of the Department of Chemistry [Outside Department].

The ligand synthesis and MOF crystallization for Chapter III were provided by Dr. Jinhee Park and the context was published in *J. Am. Chem. Soc*., 136, 16895, 2014. The compounds used in Chapter IV were prepared by Dr. Yangyang Liu of the Department of Chemistry and were published in *J. Am. Chem. Soc.*, 137, 2919, 2015. All other work for the dissertation was completed by the student independently.

Funding Sources

This work was supported as part of the Methane Opportunities for Vehicular Energy (MOVE) Program under the Award Number DE-AR0000249 and as part of the Center for Clean-Energy-related Gas Separation, an Energy Frontier Research Center (EFRC) funded by the U.S. Department of Energy (DOE), Office of Science, Office of Basic Energy Sciences under Award Number DE-SC0001015.

User Facility operated for the US Department of Energy (DOE) Office of Science by Argonne National Laboratory, was supported by the U.S. DOE under Contract No. DE-AC02-06CH11357.

Y.-P. Chen was partially paid on U.S. Department of Energy (DE-FC36-07GO17033) and partially on National Science Foundation (NSF CBET-0930079).

NOMENCLATURE

BET	Brunauer-Emmett-Teller
CCDC	Cambridge Crystallographic Data Centre
DED	Differential Electron Density
DFT	Density Functional Theory
DMF	*N*,*N*-Dimethyl Formamide
DMSO	Dimethyl Sulfoxide
DOE	United States Department of Energy
EDS/EDX	Energy Dispersive X-ray Spectroscopy
EtOH	Ethanol
MOF	Metal-Organic Framework
MOP(s)	Metal-Organic Polyhedron (Polyhedra)
NGV	Natural Gas Vehicle
NMR	Nuclear Magnetic Resonance
NbO	Niobium Oxide
PCN	Porous Coordination Network
PXRD	Powder X-Ray Diffraction
SBB	Supramolecular Building Block
SBU	Secondary Building Unit
SEM	Scanning Electron Microscope

TMQPTC	(2 ´ ,3″,5″,6 ´ -tetramethyl-[1,1 ´ :4 ´ ,1″:4″,1‴-quaterphenyl] 3,3‴,5,5‴ -tetracarboxylate ligand
TRDSE	Time-Resolved Diffraction Structure Envelope
ρ	Electron Density
Q_{st}	Isosteric Heat of Adsorption

TABLE OF CONTENTS

Page

LIST OF FIGURES

Page

Page

Page

Page

Page

LIST OF TABLES

Page

LIST OF CODES

Page

CHAPTER I

INTRODUCTION

Metal-Organic Frameworks (MOFs) are a new type of porous materials, which have attracted attention because they possess great gas adsorption/storage ability due to their high surface area and tailorable pores. Metal−organic polyhedra (MOPs) are a family of molecular self-assemblies containing inorganic metal units and organic linkers, which are potentially used in construction of nano-sized containers. This confined space can be applied in molecular recognition, sensing, and selective reactions. We moderated temperatures and introduced ligand configurations to direct 5 MOP formations. Most interestingly, a unique core−shell coordination molecular assembly, where a metal−organic polyhedron is encapsulated inside a metal−organic polygon, is a very rare example in the MOP field. Site-selective metal exchange was also discovered in this new structure, which was studied by single crystal X-ray diffraction analysis. Besides, introducing MOPs into MOFs can be considered a design concept. Because guest molecules prefer to be trapped in a cavity possessing similar dimensions, we can construct a pre-designed MOP with desired shape/size to selectively target specific molecules. After that, a new MOF with desired geometry and topology can be formed. Consequently, this design strategy, called Superpolyhedral Building Blocks strategy, was carried out to obtain a MOF with impressive BET surface area and gas uptake.

Among the concerned gas species, methane is considered a promising alternative energy source; however, its storage and transportation currently requires major

compromises compared to traditional fuels. Although gas liquefaction and gas compression are the most common used methods for gas storage, these inefficient approaches are often not cost-effective in separation, capture, and reversible storage of gases. MOFs have been regarded as a possibility in CH_4 storage. One of the advantages of such materials is that the desired structures of MOFs can be tailored by several synthetic strategies such as metal exchange, ligand extension, and introduction of functional groups. Therefore, identifying structural characteristic which enhance CH_4 uptake is of critical importance.

In this work, the structure solution and refinement of the sample coupled with analysis of Differential Electron Density maps have shown "trapped" methane and carbon dioxide molecules by visualization of electron density. A series of isostructural Cu-based MOFs assembled from functionalized diisophthalate ligands (PCN-30X) have been analyzed under CH_4 and CO_2 loading. Using *in situ* powder X-ray diffraction data we have developed a new technique which utilizes a charge flipping method and a calculated structure envelope to efficiently identify the gas adsorption sites in crystalline frameworks. The observation of methane migration in MOFs is the first time we were able to track a nonpolar gas, CH_4, and an easily polarizable gas, CO_2, in four MOF compounds: HKUST-1, PCN-12 and PCN-306/307. A general migration phenomenon observed in all adsorption systems revealed guest molecule behavior interacting with host framework geometry. Additionally, the open metal sites and the window openings emphasized in previous reports are not so crucial when more gas molecules were loaded. Even for polar gases, pore size and shape speak louder than the binding sites with

unscreened Coulomb force or van der Waal's force. These fundamental findings are helpful for engineers to design customized compounds because materials used in methane-powered vehicles unavoidably suffer from temperature variations. Our experimental observations together with those obtained from traditional Grand Canonical Monte Carlo simulation for CH_4 adsorption in MOFs provides better *in situ* gas loading information for researchers to design new materials.

CHAPTER II

CRYSTAL ENGINEERING ON SUPERPOLYHEDRAL BUILDING BLOCKS IN METAL-ORGANIC FRAMEWORKS APPLIED IN GAS ADSORPTION*

2.1 Introduction

Metal–organic frameworks (MOFs), consisting of inorganic nodes and organic linkers, are 3D-porous compounds potentially applied in energy-related fields, such as CO_2 capture in power plants and CH_4 storage in natural gas vehicles (NGVs).[1] Superior to conventional porous materials, MOFs provide the possibilities of customizing cavities, tailoring topologies and decorating functionalities. Particularly for practical applications in gas capture, storage and separations, these tunable structures are advantageous for engineers to design desired materials for specific needs. As an example of rational design potential, the single molecular trap is a concept that has constructed a pre-designed metal-organic polyhedron (MOP) with similar shape/size spanning the optimal conditions to selectively target a single molecule.[2] Achieving the realization to include MOPs into MOFs, the activated PCN-88 possessed a high BET surface area of 3308 $m^2\ g^{-1}$ and exceptionally high CO_2 uptake of 160 $cm^3\ g^{-1}$ at 273 K [2] (record-high Mg-MOF-74, 162 $cm^3\ g^{-1}$ at room temperature).

On the other hand, ligand extension within MOFs has been utilized to obtain high surface area [3], proportional to monolayer physisorption capacity. However, formation of interpenetrated structures is more thermodynamically favored with increasing ligand

*Reproduced with permission from Chen, Y.-P.; Liu, T.-F.; Fordham, S.; Zhou, H.-C., Crystal Engineering on Superpolyhedral Building Blocks in Metal-Organic Frameworks Applied in Gas Adsorption, *Acta Crystallogr., Sect. B: Struct. Sci.*, B71, 613-618, **2015**. Copyright 2015 by International Union of Crystallography.

length compared to the dimension of secondary building units (SBUs).[4] Such an interpenetrated framework might decrease the accessible porosity and increase spatial hindrances, diminishing the expected merits of the extended ligands approach. If the MOPs are considered a magnified SBU, therefore, adopting MOPs as super secondary building blocks (SBBs) [5] in MOFs will allow the critical ligand length to be extended to build non-interpenetrated structures. Furthermore, MOPs acting as SBUs usually have higher symmetry and connectivity than regular SBUs. These pre-designed units provide a toolbox of building blocks to construct MOFs with greater predictability rather than serendipity.

Based on our previous experience, cuboctahedral cages and octahedral cages are the most common SBBs in MOFs.[6] Yuan et al. reported that an isoreticular series of MOFs, PCN-6X, were made from square planar dicopper(II) paddlewheels and 120°-angular-hexacarboxylate ligands with dimension ranging from 6.9 Å to 13.8 Å.[7] In that work, all the structures incorporate 12-Å cuboctahedral cages as SBBs without interpenetrations. Another type of SBBs, octahedral cages, can be assembled with square planar building units and 90°-angular-carboxylate ligands.[8] With rational design, the linker unit can adopt 9H-carbazole-3,6-dicarboxylate groups (CDC) to form an intersection with right angle (Figure II. 1a). However, the synthesis of CDC-featuring ligand is more difficult. Herein, we have constructed a MOF sustained with 12-connected octahedra as SBBs but using easy synthesis of 120°-angular-carboxylate ligands (Figure II. 1b). This work demonstrated the generalization of the SBB strategy and found alternatives to avoid inconvenient synthetic processes.

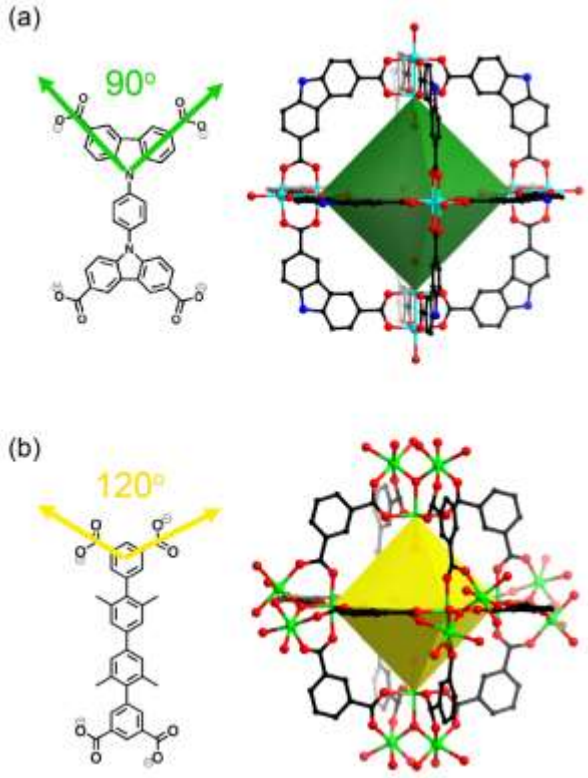

Figure II. 1 Schematic representation of molecular octahedral cages and the available ligands to construct such a MOP. (a) 90°-angular carboxylate ligand; (b) 120°-angular carboxylate ligand.

2.2 Experimental Section

2.2.1 Synthesis of H_4TMQPTC*

H_4TMQPTC (2′,3″,5″,6′-tetramethyl-[1,1′:4′,1″:4″,1‴-quaterphenyl] 3,3‴,5,5‴-tetracarboxylic acid) was chosen as the 120°-angular carboxylate ligand to construct a SBB unit. The synthesis of H_4TMQPTC exactly followed Liu's procedure [9] (Yield 68%). ^{1}H NMR (300 MHz, DMSO-d6): δ = 2.051 (s, 12H), 7.516 (s, 4H), 7.925 (d, 4H), 8.490 (t, 2H). Elemental analysis (%): Anal. Calcd for $C_{32}H_{26}O_8$: C, 71.37; H, 4.87. Found. C, 70.11; H, 5.02

2.2.2 Synthesis of PCN-426(Ni) and PCN-427(Cu)

To synthesize PCN-426(Ni), $Ni(NO_3)_2 \cdot 6H_2O$ (30 mg), H_4TMQPTC (10 mg), a solution of DMF, EtOH and H_2O (v:v:v= 4:1:1) 3 mL were homogeneously mixed in a Pyrex vial. The mixture was heated in 95 ℃ oven for 24 h, and the resulting green crystals were harvested. The synthetic recipe to obtain PCN-427(Cu) is similar to that of PCN-426(Ni), except 30 mg $Cu(NO_3)_2 \cdot 2.5H_2O$ was used instead of $Ni(NO_3)_2 \cdot 6H_2O$.

2.2.3 Sample Activation and Adsorption Measurements

As-synthesized PCN-426(Ni) and PCN-427(Cu) crystals were washed with fresh DMF, followed with methanol three times over a 1-day period, and then with dichloromethane three times over another 1-day period. Direct evacuation of both of the samples failed because the surface tension collapsed the frameworks upon solvent removal. A CO_2 supercritical drying procedure was employed to activate samples where the solvent molecules are exchanged with liquid CO_2. After the system had been heated

*Synthesis of H_4TMQPTC was conducted by Dr. Tian-Fu Liu.

above the carbon dioxide critical point (T = 31 ℃, P = 73 atm) for 30 min, it was slowly vented to 1 atm. The resulting dried crystals were quickly loaded into BET sample tubes and then measured using a Micrometritics ASAP 2020 instrument.

2.2.4 Single Crystal / Powder X-Ray Diffraction

Single crystal X-ray diffraction for PCN-426(Ni) and PCN-427(Cu) were recorded at 110 K using the Bruker Smart Apex diffractometer (Mo-Kα radiation, λ = 0.71073 Å). The multi-scan technique implemented in *SADABS* [10] was utilized for absorption and beam corrections of the intensity data. Both structures were solved by direct methods and refined by full-matrix least-squares on F^2 using *SHELXTL* (Sheldrick, Ver. 6.14, Structure Determination Software Suite, Bruker AXS, Madison, WI, 2003). Non-hydrogen atoms were refined with anisotropic displacement parameters while the organic hydrogen atoms were calculated with isotropic thermal parameters and set to 1.2 × U_{eq} of the attached atom. The scattering due to solvent molecules in the two structures were unsuccessfully refined and thus removed using the *SQUEEZE* routine of *PLATON* [11]. The accessible voids in the structures of PCN-426(Ni) and PCN-427(Cu) were estimated to correspond to 75.2% and 63.8% of the total volumes, respectively. Crystallographic data and structural refinements are summarized in Table II. 1.

The powder X-ray diffraction patterns (PXRD) for PCN-426(Ni) and PCN-427(Cu) were recorded at room temperature on a Bruker D8-Focus Bragg−Brentano X-ray Powder diffractometer (Cu sealed tube, λ = 1.54178 Å). The simulated PXRD patterns were obtained by the Mercury program based on the single-crystal CIF file.[12]

Table II. 1 Crystal data and structure refinements for PCN-426(Ni) and PCN-427(Cu).

	PCN-426(Ni)	**PCN-427(Cu)**
CCDC	1414843	1414844
Formula	$Ni_{3.17}C_{32}H_{22}O_{16}$	$Cu_2C_{32}H_{22}O_{10}$
Formula weight	848.41	693.58
Crystal System	Cubic	Tetragonal
Space Group	$Fm\bar{3}m$	$P4_2/mnm$
a (Å) = b (Å)	40.9779(8)	18.7570(5)
c (Å)	40.9779(8)	36.092(2)
α (º)= β (º)= γ (º)	90.000	90.000
V (Å^3)	68810(2)	12698.2(9)
Squeezed Volume	51776 (75.2%)	8102 (63.8%)
Z	24	8
$d_{calcd.}$ (g/cm^3)	0.491	0.726
μ(mm^{-1})	0.536	0.697
F(000)	10336	2816
θ_{max} [deg]	25.03	26.00
Completeness	99.5%	99.9%
Collected / Unique reflections	168914 / 2998	131327 / 6634
Parameters / Restraints	78 / 17	142 / 0
R_{int}	0.1168	0.0885
$R1$ [I > 2σ(I)]	0.0908	0.0705
$wR2$ [I > 2σ(I)]	0.2133	0.1452
$R1$ (all data)	0.1415	0.1009
$wR2$ (all data)	0.2392	0.1579
GOF on F^2	1.003	1.007
$\Delta\rho_{max}/\Delta\rho_{min}$ [e·Å^{-3}]	0.709 / -0.629	0.810 / -0.625

2.3 Results and Discussion

2.3.1 Structure and Topology Description of PCN-426(Ni)

Solvothermal reaction of H_4TMQPTC and $Ni(NO_3)_2 \cdot 6H_2O$ in the solvent mixture of DMF, EtOH and H_2O afforded green crystals of PCN-426(Ni) with a formula of $[Ni_3(\mu_3\text{-}O)O_7$ (TMQPTC)$]\cdot Ni_{0.17}$. The seven coordinated O atoms in metal cluster (Figure II. 2a) are from H_2O molecules and/or reaction solvents. Single-crystal X-ray diffraction studies revealed that the as-synthesized PCN-426(Ni) contains isolated Ni(II) ions located at the center of the small pores (yellow spheres in Figure II. 2b). To maintain the framework neutral charged, the isolated Ni(II) ions have to attract counter-ions coming from DMF fragments and/or OH^-, not included in the structure model due to uncertainty. However, after sample wash and activation, the Ni(II) ions and the counter-ions should be removed from the structure.

The obtained PCN-426(Ni) crystallizes in the $Fm\ \bar{3}m$ space group with a = 40.9779(8) Å. This cubic structure is constructed by disordered $[Ni_3(\mu_3\text{-}O)]$ clusters and TMQPTC ligands with molar ratio of 1:1. With further inspection of the $[Ni_3(\mu_3\text{-}O)]$ clusters, each unit consists of three octahedrally coordinated Ni(II) ions. Based on CCDC database, a saturated $[M_3(\mu_3\text{-}O)]$ cluster is fully coordinated by six carboxylates and three dangling solvents, giving rise to 6-connected nodes. In contrast, each of the presented $[Ni_3(\mu_3\text{-}O)]$ is connected with four carboxylate ligands and the remaining two coordination sites occupied by solvents.

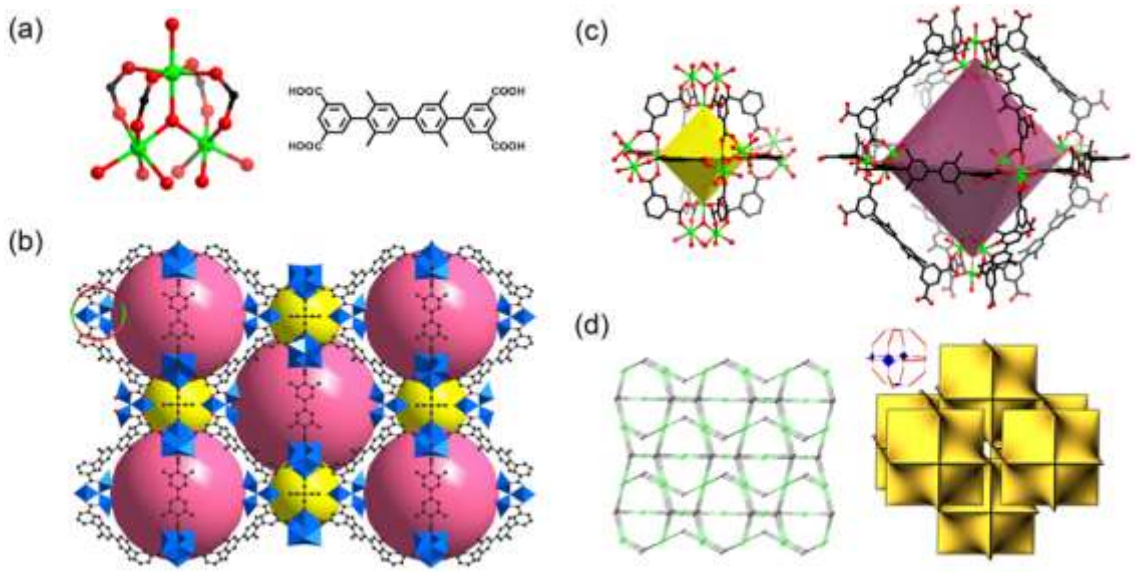

Figure II. 2 Structure details of PCN-426(Ni). (a) [$Ni_3(\mu_3$-O)] cluster and H_4TMQPTC; (b) packing of the PCN-426(Ni) viewed along [1 1 0]; the blue nodes are [$Ni_3(\mu_3$-O)] clusters shown above; (c) two types of octahedral cages incorporated in PCN-426(Ni) (Ni, green; C, black; O, red, H atoms have been omitted for clarity); (d) *nbo*-type topology and tiling (a face-to-face packing) for the *nbo* net. The inset sketch shows the skeleton of one tile.

As depicted in Figure II. 2b and c, the overall PCN-426(Ni) structure contains two types of octahedral cages packed with a 1:1 ratio. The small octahedron (yellow, ~11Å internal pore diameter) is assembled by six [$Ni_3(\mu_3$-O)] vertices and twelve isophthalate edges. Each small octahedron connects to another small octahedron through TMQPTC ligands. Similarly, the large octahedron (purple, ~21Å internal pore diameter) is composed of six metal nodes joined by twelve 120°-angular TMQPTC linkage units as well.

Topologically, each SBU and each linker in PCN-426(Ni) can be simplified into 4-connected nodes, and thus the resulting 4-c uninodal net mimics an NbO-type structure

with a Schläfli symbol of $\{6^4 \cdot 8^2\}$ (Figure II. 2d). From an alternative perspective, if the small octahedral cages (shown in Figure II. 2c) serve as 12-connected SBBs, the structure can be extended into $\{3^{24} \cdot 4^{36} \cdot 5^6\}$ net with *fcu* topology, which is well known for its characteristic of cubic closest sphere packing. It is worthy to mention that the reported PCN-82 adopts *tfb* net incorporating octahedrons constructed by 90°-angular carboxylate ligands (Figure II. 1a).[4] The same structure can also be described as *fcu* net if octahedral SBBs are taken as nodes. The SBB approach is rather powerful to reduce structure connectivity as predicted.

2.3.2 Structure and Topology Description of PCN-427(Cu)

With the rational design using the SBB approach, octahedral SBBs can be constructed by square planar paddlewheels and tetratopic ligands featuring 90°-angular carboxylate moieties, as opposed to the 120°-angular TMQPTC ligands. We were thus curious about what the geometrical constitution can be with square planar nodes and the 120°-angular linkers.

X-ray diffraction analysis suggests that PCN-427(Cu) crystallize in the space group of $P4_2/mnm$, with a formula of $[Cu_2O_2$ (TMQPTC)]. Each Cu(II) ions is coordinated by five O atoms in a pyramidal geometry; each pair of Cu(II) ions is bridged by four TMQPTC ligands and two O atoms representative of axially coordinated solvents, forming a paddle wheel unit. A view of the structure of PCN-427(Cu) along the *a* or *b*-axis illustrates two types of lantern-shaped cages with eight $[Cu_2O_2]$ vertices are embedded in the structure (Figure II. 3a). A view along the *c*-axis shows distorted tetragonal channels, instead of closed cages, that go through the framework (Figure II.

3b). As shown in Figure II. 3c, each paddle wheel unit and each linkage unit can be reduced to 4-c binodal network with an *ssb*-type topology symbolled as $\{4^2 \cdot 8^4\}$.

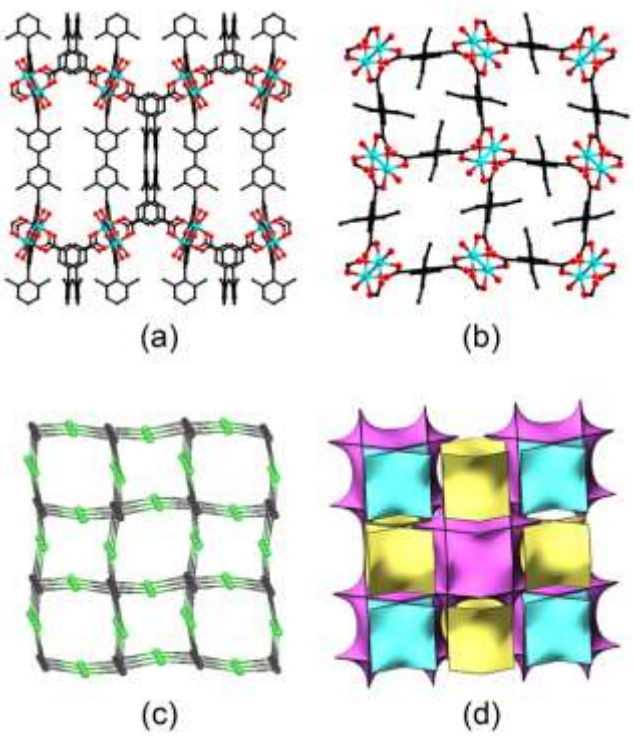

Figure II. 3 Structure details of PCN-427(Cu). (a) Packing of the PCN-427 viewed along the *b*-axis; (b) packing of the PCN-427 viewed along the *c*-axis (Cu, cyan; C, black; O, red). (c) *ssb*-type topology and (d) tiling for the *ssb* net.

In previous report [13], the relationship between pore volumes and H_2 adsorption in MOF materials has been explored by using a similar tetratopic ligand, quaterphenyl-3,3″,5,5″-tetracarboxylic acid (Figure II. 4 bottom). From a topological viewpoint, it has been known that the 4-c nets with square coordinated motifs might form the uninodal nets *nbo* and *lvt* or the binodal nets *ssa* and *ssb* [14]. In spite of very little difference in the

ligand conformation, Lin *et al.*'s structure adopts the uninodal *nbo* net while our PCN-427(Cu) adopts the binodal *ssb* net. Interestingly, it can be seen that the linkers of lantern-shaped cage are parallel in PCN-427(Cu) but crossed in Lin's structure (Figure II. 4). This difference is probably due to steric hindrance of the side methyl groups separating the neighboring ligands distantly.

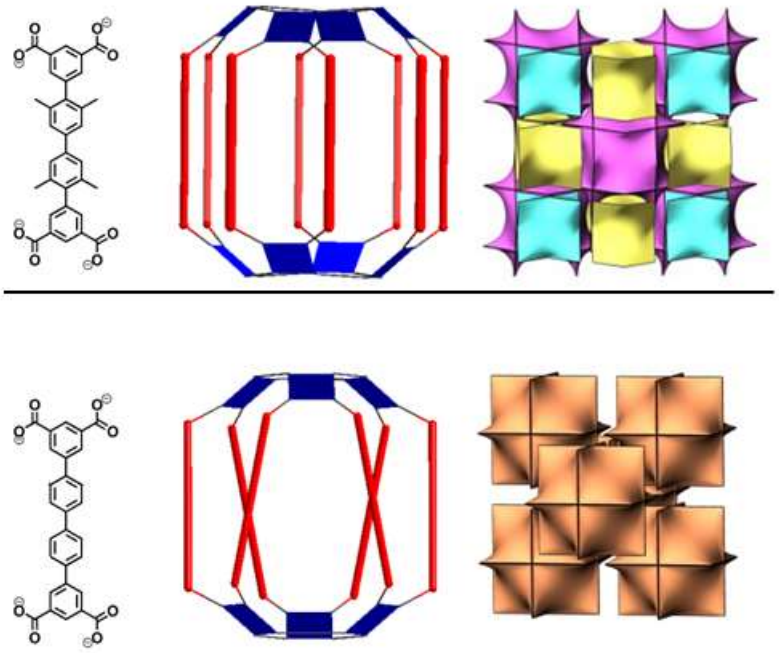

Figure II. 4 (top) Partial structure of PCN-427(Cu) constructed with *ssb*-type topology; (bottom) Reported structure analogous to PCN-427(Cu); it was described as *nbo*-type topology. Both cage sketches show the skeleton of one tile.

2.3.3 N_2 /CH_4 /CO_2 Gas Adsorption

In Figure II. 5, the crystallinity and phase purity of the two products were verified. The differences between experimental and calculated patterns can be explained due to different collection parameters, the PXRD was performed at room temperature while the single-crystal XRD was conducted at 110K.

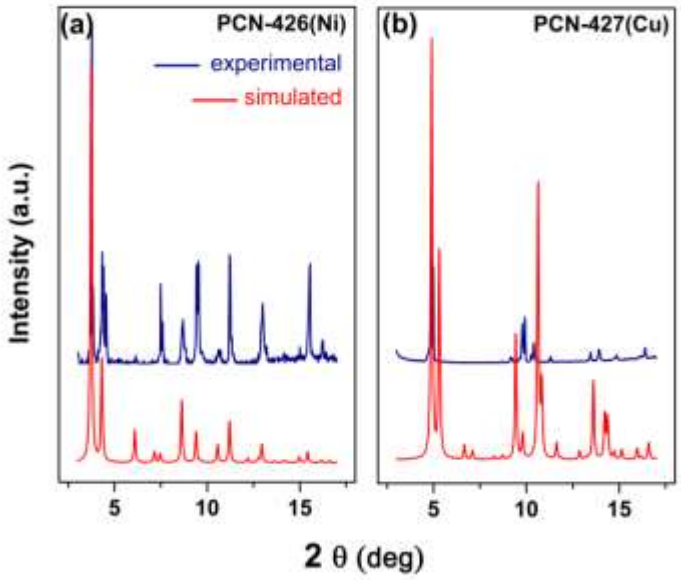

Figure II. 5 Powder X-ray diffraction patterns (λ = 1.54178 Å) of (a) PCN-426(Ni) and (b) PCN-427(Cu). The match between the experimental (blue) and the calculated curve (red) confirms the phase purity of the products.

To confirm the porosity of PCN-426(Ni) and PCN-427(Cu), the crystalline samples were activated by a CO_2 supercritical drying procedure, with successful degassing under a dynamic vacuum at 80 ℃ for 12 h. The N_2 sorption isotherm at 77 K for PCN-426(Ni) exhibits a reversible Type-I adsorption behavior (Figure II. 6a). The sorption result also suggested that PCN-426(Ni) possesses permanent micro-porosity

with considerably high N_2 uptake (ca. 1500 cm^3 /g) and corresponding Brunauer−Emmett−Teller (BET) surface area of 3935 m^2 /g. The high surface area of PCN-426(Ni) inspired us to further study other gas adsorption behaviors, especially for clean energy CH_4 and greenhouse gas CO_2. This showed that PCN-426(Ni) can take up 30 cm^3 /g of CH_4 and 78 cm^3 /g of CO_2 at 273 K and 1 bar (Figure II. 6b).

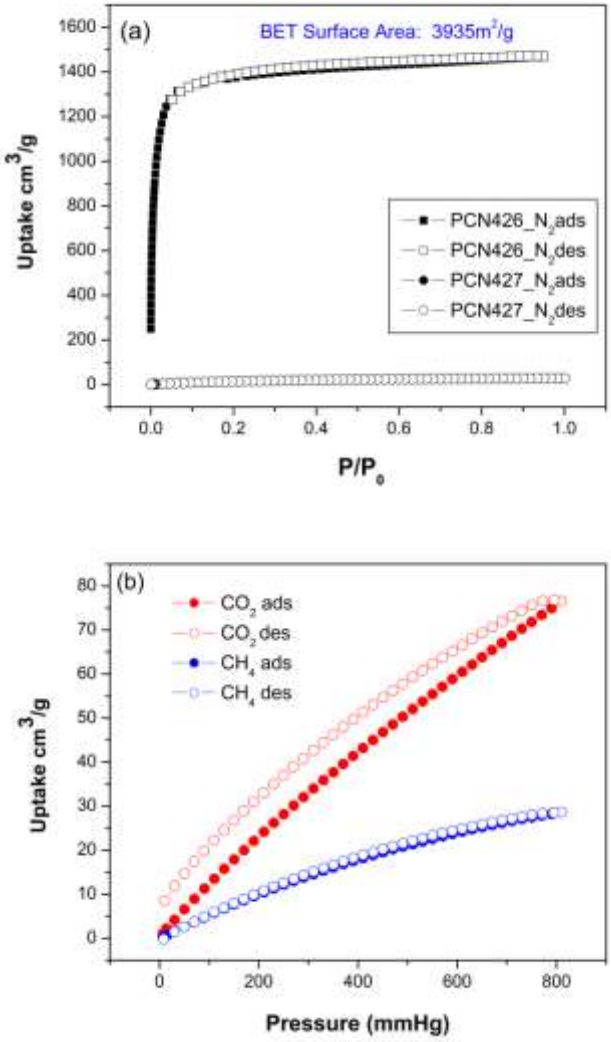

Figure II. 6 (a) N_2 sorption isotherms for PCN-426(Ni) and PCN-427(Cu) at 77 K, adsorption (solid)/desorption (hollow); (b) CO_2 and CH_4 sorption isotherms for PCN-426(Ni) at 273K.

Although the structure of the as-synthesized PCN-427(Cu) possesses considerable porosity (Figure II. 3), it failed to show substantial N_2 uptake as shown in Figure II. 6a. The bare N_2 uptake of PCN-427(Cu) originated from the framework collapse during solvent removal, even using a CO_2 supercritical drying procedure. However, based on octahedral SBBs, PCN-426(Ni) possesses a more mechanically robust framework with CO_2 uptake capacity similar to other notable MOFs (Table II. 2).

Table II. 2 CO_2 uptake capacity of selected MOFs at 1 bar.

MOF Sorbents	**BET Surface Area ($m^2. g^{-1}$)**	**CO_2 uptake (wt %)**	**Temperature (K)**	**Reference**
PCN-426(Ni)	3935	15.3	273	This work
HKUST-1	1781	15.2	298	Millward *et al.*[15]
Mg-MOF-74	1174	27.5	298	Bao *et al.*[16]
PCN-6	3811	15.9	298	Kim *et al.*[17]
Mmen-Cu-BTTri	870	15.4	298	Mcdonald *et al.*[18]

2.4 Conclusion

In this work, we have synthesized PCN-426(Ni) and PCN-427(Cu) by using a tetratopic ligand featuring 120°-angular carboxylate moieties. Based on the SBB design strategy, PCN-426(Ni) was constructed with pre-designed octahedral SBBs spanned by six $[Ni_3(\mu_3\text{-}O)]$ vertices. In contrast, PCN-427(Cu) containing $[Cu_2O_2]$ units cannot be synthesized as a SBB-based framework. After a CO_2 supercritical drying procedure, PCN-426(Ni) possesses Brunauer– Emmett–Teller (BET) surface area as high as 3935 $m^2\ g^{-1}$, taking up 1500 $cm^3\ g^{-1}$ of N_2 at 77K, 30 $cm^3\ g^{-1}$ of CH_4 and 78 $cm^3\ g^{-1}$ of CO_2 at 273 K and 1 bar. In the future perspective, we are attempting to study which SBBs favor gas storage in MOFs by direct measurements using PXRD analysis (CHAPTER IV).[19]

CHAPTER III

CHARACTERIZATION: SINGLE-CRYSTAL X-RAY DIFFRACTION APPLIED TO OBSERVE STRUCTURE TRANSITION*

3.1 Introduction

Over the past two decades, coordination driven molecular self-assemblies have been studied extensively due to their beautiful structures, unique physical/chemical properties, and potential applications. Among such self-assembled structures, a variety of metal-organic polygons/polyhedra (MOPs) have been designed and synthesized, using inspirations drawn from not only geometric entities such as Archimedean and Platonic solids but also biological systems with high symmetry.[5, 20-26] Both interior and exterior functionalizations[27-29] of MOPs have been carried out, allowing the isolation of the confined space to be explored toward molecular recognition,[28, 30] sensing,[31] catalysis,[32-36] regioselective[37-38] and self-sorting reactions,[39] molecular flasks,[40-41] storage of reactive species,[42] and other potential applications.[42-43]

Structures of the resulting MOPs are often controlled by the coordination geometry of the metal or metal units, and the bridging angles of the organic ligands.[21, 25, 43-47] Recently, a few new synthetic methods, such as bridging-ligand-substitution strategy and the use of mixed ligand systems, have been developed in our laboratory to expand the structural diversity of MOPs.[48-49] However, compared to natural systems, the

*Reproduced with permission from Park, J.†; Chen, Y.-P.† (†equal contribution); Perry, Z.; Li, J.-R.; Zhou, H.-C., Preparation of Core-Shell Coordination Molecular Assemblies via the Enrichment of Structure-Directing "Codes" of Bridging Ligands and Metathesis of Metal Units, *J. Am. Chem. Soc.*, 136, 16895–16901, **2014**. Copyright 2014 by American Chemical Society.

structural complexity of MOPs is still limited; new strategies need to be developed to enrich MOP chemistry.

Nature utilizes a variety of weak interactions such as H-bonding, π-π stacking, and hydrophobic interactions to build various biological systems with relatively simple building units containing structure-directing "codes". For example, DNA double strands are constructed based on Watson-Crick pairs which rely on complementary H-bonding interactions resulting from specific base pairs. In coordination driven molecular self-assemblies, the building blocks (organic linkers and metal-containing nodes) can be designed to possess structure-directing "codes" such as built-in multiple H-bonding interaction sites, intrinsic coordination modes, and variable coordination angles (Figure III. 1), leading to the formation of MOPs with desired structural features and functionalities.[21] As the "codes" directing the structure become more complicated, the complexity of the coordination assembly will increase (Figure III. 2).

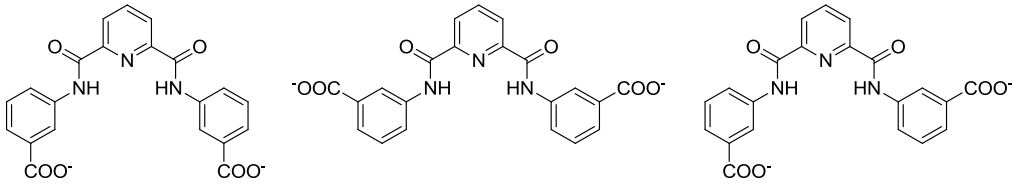

$H_2\,\alpha$-L^1 $H_2\,\beta$-L^1 $H_2\,\gamma$-L^1

Figure III. 1 Three different conformers of 3,3′-H_2PDBAD, L^1.

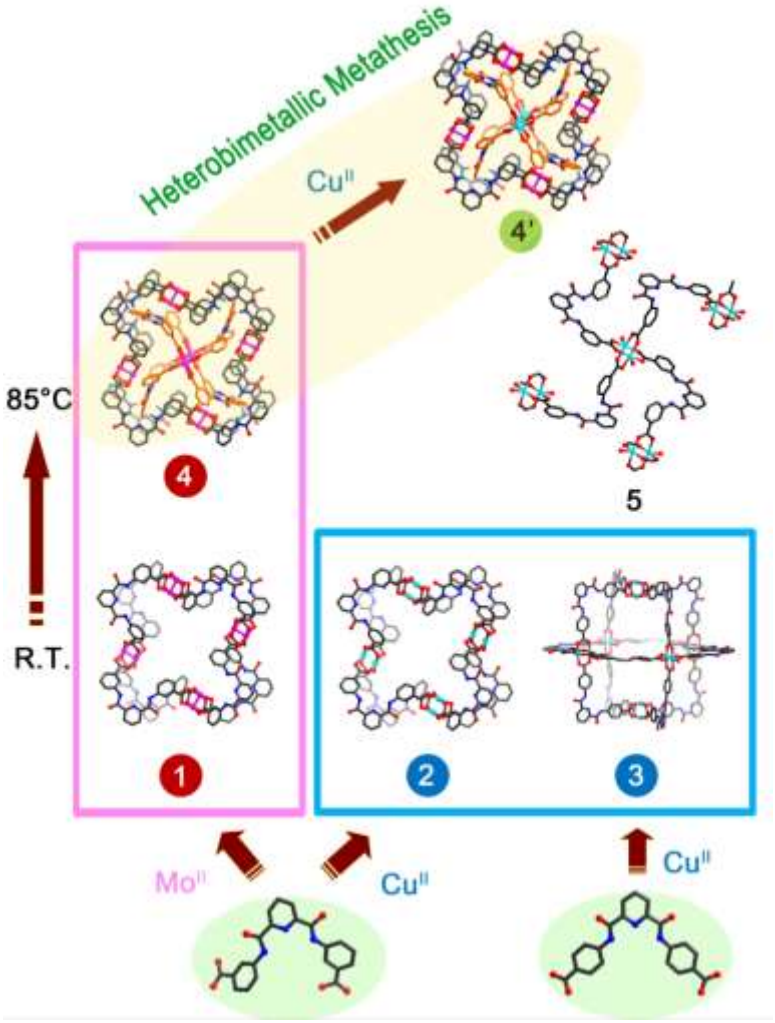

Figure III. 2 The overview scheme of all self-assembled structures in this work.

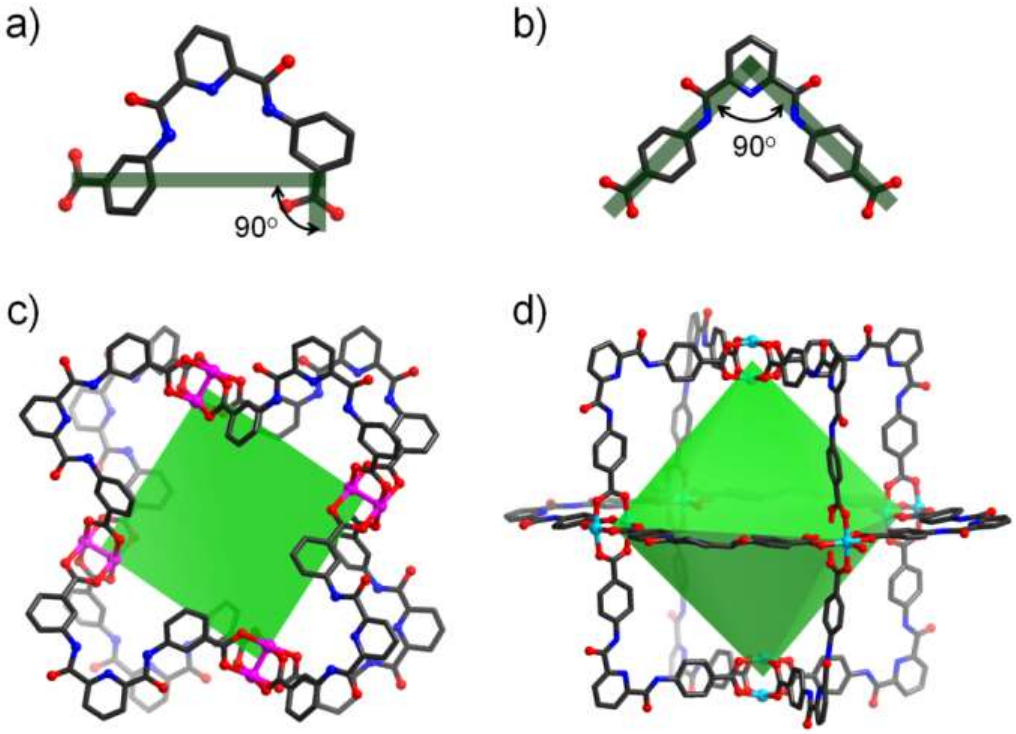

Figure III. 3 Structures of molecular assemblies 1 (c) and 3 (d) as well as their 90° bridging-angle ligands, L^1 (a) and L^2 (b), respectively (H atoms of ligands and coordinated solvent molecules were omitted for clarity). Color scheme: Mo, pink; Cu, cyan; O, red; N, blue; C, black. The green polygon and polyhedron represent geometries of 1 and 2 when considering metal clusters as vertices and ligands as edges.

3.2 Experimental Section*

3.2.1 Synthesis of 3,3'-H_2PDBAD, L^1

L^1 (Figure III. 1) was synthesized as follows. 2,6-pyridinedicarboxylic acid (2.0 g, 12.0 mmol) and thionyl chloride (40.0 mL, 0.55 mol) were mixed in a dried 250 mL round-bottomed flask. *N*,*N*-dimethylformamide (1.0 mL, 12.9 mmol) was carefully added dropwise, and the mixture was stirred and heated at 75 °C for 6 h under N_2 flow.

*The compounds were synthesized by Dr. Jinhee Park. All the recipes were obtained from *J. Am. Chem. Soc.*, 136, 16895–16901, **2014**.

The excess thionyl chloride was removed under vacuum, quenched with ethanol and then water. Due to the reactivity of 2,6-pyridinedicarbonyl chloride, the residual 2,6-pyridinedicarbonyl chloride was used without further purification. 2,6-pyridinedicarbonyl chloride (0.61 g, 3.0 mmol) was dissolved in 20 mL of anhydrous acetonitrile and added dropwise to a solution of 3-aminobenzoic acid (0.96 g, 7.0 mmol) in acetonitrile (20 mL). The resulting mixture was stirred at room temperature for 24 h and then refluxed for 2 h. The precipitated white solid was isolated by filtration and washed with 100 mL of acetonitrile followed by 500 mL of water and then overnight drying under vacuum. Yield for the two steps: 0.98 g, 81%. ^{1}H-NMR (300 MHz, DMSO-d_6) δ 11.19 (s, 2 H), 8.56 (s, 2 H), 8.45 (d, 2 H, J=7.2 Hz), 8.34 (t, 1 H, J=7.6 Hz), 8.20 (d, 2H, J=8.1 Hz). IR (ν max): 3379, 3329, 2816, 1678, 1604, 1589, 1519, 1454, 1408, 1315, 1288, 1242, 1184, 1118, 999, 933, 891, 856, 767, 740, 686 cm^{-1}. Elemental Analysis (% calc/found): C, 62.22/62.09; H, 3.73/3.76; N, 10.37/10.41.

3.2.2 Synthesis of 4,4'-H_2PDBAD, L^2

L^2 (Figure III. 3b) was isolated from the same procedure except using 4-aminobenzoic acid instead of 3-aminobenzoic acid. Yield of 0.96 g, 79% for two steps. ^{1}H-NMR (300 MHz, DMSO-d_6) δ 11.28 (s, 2 H), 8.46 (d, 2 H, J=7.5 Hz), 8.34 (t, 1 H, J=7.5 Hz), 8.13 (d, 2 H, J=7.8 Hz), 8.05 (d, 2H, J=7.8 Hz). IR (ν max): 3286, 3228, 2808, 1697, 1658, 1589, 1554, 1531, 1438, 1292, 1230, 1138, 1080, 999, 948, 898, 813, 756, 736, 659 cm^{-1}. Elemental Analysis (% calc/found): C, 62.22/61.97; H, 3.73/3.60; N, 10.37/10.20.

3.2.3 Synthesis of $Mo_2(OAc)_4$

Under nitrogen 2.99g of $Mo(CO)_6$ (11.3 mmol) was added to a stirring mixture of 100 mL glacial acetic acid and 20 ml acetic anhydride. A vacuum was applied and the flask was backfilled with nitrogen; this was repeated three times. The solution was allowed to reflux for 32 hours. At this point stirring was stopped and the flask was allowed to cool overnight, yielding crystals which appeared to be green in color. After washing three times with ethanol, the now bright yellow crystals were dried under reduced pressure. Yield: 1.0176 g (2.2 mmol), 39%.

3.2.4 Synthesis of $[Mo_2(\gamma\text{-}L^1)_2(DEF)_2]_4 \cdot S$ 1

A Mixture of $H_2\mathbf{L^1}$ (20 mg), $Mo(OAc)_2$ (20 mg), and *N*,*N*-diethylformamide (DEF) (1.5 mL) was placed in a 2 mL vial. The vial was purged with N_2 and allowed to sit in room temperature for 2 days. Yellow block crystals of **1** were obtained. IR (ν max): 3313, 3078, 1681, 1589, 1531, 1392, 1303, 1222, 1141, 1076, 979, 910, 840, 810, 756, 678 cm^{-1}. Elemental Analysis of activated **1** (% calc/found): C, 50.52/46.92; H, 2.62/3.66; N, 8.42/9.01.

3.2.5 Synthesis of $[Cu_2(\gamma\text{-}L^1)_2(DMA)_2]_4 \cdot S$ 2

$H_2\mathbf{L^1}$ (8 mg), $Cu(OAc)_2$ (8 mg) and *N*,*N*-dimethylacetamide (DMA) (1.5 mL) were added 2 mL vial. The reaction took place at 4 °C for 2 days. Green block crystals were collected. IR (ν max): 3294, 3078, 1678, 1531, 1431, 1392, 1307, 1222, 1145, 1080, 999, 910, 837, 759, 678 cm^{-1}. Elemental Analysis of activated **2** (% calc/found): C, 54.02/51.72; H, 2.81/4.58; N, 9.00/11.02.

3.2.6 Synthesis of $[Cu_2(L^2)_2(DMA)_2]_6$·*S* 3

2,6-Lutidine 0.1 mL added to the mixture of $H_2\mathbf{L^2}$ (40 mg), $Cu(NO_3)_2$ (25 mg) and DMA (15 mL) in 20 mL vial. The reaction took place at RT in 1 day. Blue plate crystals were collected. IR (ν max): 3260, 3101, 1662, 1600, 1527, 1384, 1315, 1176, 1110, 1080, 1014, 860, 779, 744, 682 cm^{-1}. Elemental Analysis of activated **3** (% calc/found): C, 54.02/50.65; H, 2.81/3.86; N, 9.00/8.97.

3.2.7 Synthesis of $[Mo_2(\gamma\text{-}L^1)_2(DMA)_2]_4[Mo_2(\alpha\text{-}L^1)_2(DMA)_2]_2$·*S* 4

A mixture of $H_2\mathbf{L^1}$ (20 mg) and $Mo(OAc)_2$ (20 mg) in 1.5 mL of DMA was prepared in a 2 mL vial, purged with N_2 and heated to 85 °C for 2 days. Light red block crystals were isolated. IR (ν max): 3290, 3082, 1658, 1589, 1531, 1388, 1300, 1222, 1138, 1076, 956, 914, 840, 813, 756, 675 cm^{-1}. Elemental Analysis of **4** (% calc/found): C, 50.52/48.14; H, 2.62/3.82; N, 8.42/8.73.

3.2.8 Metal Ion Metathesis for Cu-core Mo-shell $[Mo_2(\gamma\text{-}L^1)_2]_4[Cu_2(\alpha\text{-}L^1)_2]_2$·*S* 4′

Due to the oxygen sensitivity of Mo^{2+} complexes, the entire sample preparation steps were conducted in an Ar atmosphere glove box. The as-synthesized single crystals of **4** were briefly washed with fresh DMF. Approximately 20 mg of the crystals **4** were soaked in 2 mL of 100 mM $Cu(NO_3)_2$ in DMF for 6 h, 1 day, 2 days and 20 days. During the soaking process, the solution was refreshed with fresh $Cu(NO_3)_2$ solution every day. Single crystal X-ray diffraction analysis was performed on the crystals directly taken out from the solution without further washing process. For EDS analysis, the solution was exchanged with fresh DMF for 2 days to remove any remaining residues.

3.3 Results and Discussion

3.3.1 Single Crystal X-ray Crystallography

All MOP crystals were mounted onto a loop from mother liquid for single crystal X-ray data collection without further treatment. Diffractions were measured on a Bruker Smart Apex diffractometer equipped with a Mo-Kα sealed-tube X-ray source (λ = 0.71073 Å) and liquid nitrogen stream (110 K). The data frames were recorded using the program APEX2 and processed using the program *SAINT* (v7.68A routine within APEX2 (v2012.2.0). Absorption and beam corrections based on the multi-scan technique were applied to the integrated data using *SADABS* (v2008/1). All the structures were solved by direct method using *SHELXS* and refined by full-matrix least-squares on F^2 using *SHELXL* software.

Carbon atoms with enormous thermal ellipsoids were refined with the help of EADP restrains on each ligand to clear the warnings about non-positive definite matrices. All non-hydrogen atoms needed to be refined with anisotropic displacement parameters during the final cycles. Organic hydrogen atoms were located in calculated positions with isotropic displacement parameters set to 1.2 × U_{eq} of the attached atoms. The solvent molecules were highly disordered, and attempts to locate and refine the solvent peaks were not always successful. Contributions to scattering due to these highly disordered solvent molecules were removed using the *SQUEEZE* routine of *PLATON*. The refinement details and validation reply can be found in the following subsections. The CIF files can be obtained free of charge from the Cambridge Crystallographic Data Centre. CCDC numbers and the crystal information are listed in Table III. 1.

Table III. 1 Crystal data and results of structure refinement.

	1	**2**	**3**	**4**	**4′**	**5**
	Mo Shell	Cu Shell	Octahedral Cage	Mo Core-Shell	Mo Core/Cu Shell	Cu 2D sheet
CCDC	953691	953692	953693	953694	953695	953696
Formula	Mo_8 $C_{168}H_{104}N_{24}O_{56}$	Cu_8 $C_{168}H_{104}N_{24}O_{56}$	Cu_{12} $C_{252}H_{156}N_{36}O_{84}$	Mo_{12} $C_{252}H_{156}N_{36}O_{80}$	$Cu_{5.6}Mo_{6.4}$ $C_{252}H_{156}N_{36}O_{78}$	Cu_2 $C_{58}H_{62}N_{10}O_{16}$
Mol. weight	4122.27	3863.07	5794.61	6119.41	5905.97	1282.26
Color/Shape	Orange Octahedron	Green Octahedron	Blue Square plates	Yellow Rod	Green Rod	Green Chunk
Crystal system	Tetragonal	Orthorhombic	Triclinic	Tetragonal	Tetragonal	Monoclinic
Space group	*I*4/*m*	*Cmce*	*P*-1	*I*4/*m*	*I*4/*m*	$P2_1/c$
a (Å)	34.623(2)	23.524(5)	26.273(5)	31.220(10)	31.22(3)	8.9180(12)
b (Å)	34.623(2)	31.791(7)	26.687(5)	31.220(10)	31.22(3)	15.890(2)
c (Å)	16.4266(10)	48.797(10)	29.106(6)	24.656(8)	25.05(3)	20.734(3)
α (°)	90.00	90.00	90.067(3)	90.00	90.00	90.00
β (°)	90.00	90.00	108.930(2)	90.00	90.00	97.404(2)
γ (°)	90.00	90.00	105.381(2)	90.00	90.00	90.00
V (Å^3)	19691(2)	36493(13)	18527(6)	24032(14)	24416(44)	2913.6(7)
Z	2	4	1	2	2	2
$d_{calcd.}$ (g/cm^3)	0.695	0.703	0.519	0.846	0.803	1.462
μ(mm^{-1})	0.287	0.501	0.370	0.352	0.446	0.809
F(000)	4128	7840	2940	6128	5950	1332
θ_{max} [deg]	26.00	26.00	24.98	24.00	24.82	26.00
Completeness	99.9 %	99.5 %	97.8 %	99.7 %	98.2%	100.0%
Collected refln	103537	94146	132545	86231	25881	21574
Unique refln	10019	18320	63673	9669	10619	5724
Parameters	261	245	679	237	176	411
Restraints	15	39	116	21	23	9

(Table III.1 continued)

	1	**2**	**3**	**4**	**4′**	**5**
	Mo Shell	Cu Shell	Octahedral Cage	Mo Core-Shell	Mo Core/Cu Shell	Cu 2D sheet
CCDC	953691	953692	953693	953694	953695	953696
R_{int}	0.0741	0.0802	0.1041	0.1934	0.1836	0.0706
$R1$ [I > 2σ(I)]	0.0626	0.1591	0.0815	0.1353	0.1434	0.0441
$wR2$	0.1625	0.3077	0.1519	0.2555	0.2659	0.0764
$R1$ (all data)	0.0881	0.2137	0.2168	0.2542	0.3304	0.0872
$wR2$ (all data)	0.1693	0.3287	0.1634	0.2847	0.3150	0.0832
GOF on F^2	1.002	1.009	0.880	0.994	1.004	1.005
$\Delta\rho_{max}/\Delta\rho_{min}$ [e·Å^{-3}]	2.753 / -0.938	2.006 / -1.030	0.751 / -0.776	1.319 / -0.780	1.136 / -0.705	0.810 / -0.808

3.3.1.1 Refinement Details of MOP 1 (953691)

Diffraction frames were integrated in Tetragonal I by APEX2. *XPREP* also agreed that low R(sym) is 0.070 for this highest symmetric Bravais lattice. *I*4/*m* was the best choice with lowest CFOM factor (4.39); however, this failed to get an initial structure. Instead, Fourier peaks were easily found with $I\bar{4}$ space group. After geometry was fixed, *PLATON* were performed twice: one checking the heavy atom moiety; the other checking the final structure. Addsym unit in *PLATON* suggested that correct space group should be promoted from non-centrosymmetric $I\bar{4}$ to centrosymmetric *I*4/*m*. By using restraints of geometry and atomic displacement parameters (ADPs), R value is 0.1712 before *SQUEEZE* treatment and 0.0881 after *SQUEEZE* treatment. The squeezed void volume was 13337 Å^3, equivalent to 67.7% of the unit cell (Figure III. 3c and Figure III. 4).

3.3.1.2 Refinement Details of MOP 2 (953692)

Diffraction frames were integrated in Orthorhombic C by APEX2, and *XPREP* also agreed that the R(sym) is 0.095 for this highest symmetric Bravais lattice. Unfortunately, it was extremely hard to solve with all orthorhombic space groups. Alternatively, we applied low-symmetry strategy to get initial solution with *P*$\bar{1}$. Addsym unit in *PLATON* suggested that correct space group should be *Cmce* when most carbon atoms were found. By using restraints of geometry and ADPs, R value is 0.3663 before *SQUEEZE* treatment and 0.1591 after *SQUEEZE* treatment. The squeezed void volume was 23739 $Å^3$, equivalent to 65.1% of the unit cell (Figure III. 5).

3.3.1.3 Refinement Details of MOP 3 (953693)

Diffraction frames were integrated in Triclinic P by APEX2. *P*$\bar{1}$ was the best candidate with lowest CFOM factor (2.70), generating Fourier peaks by direct method. Most non-hydrogen atoms could be seen straightforwardly. Addsym unit in *PLATON* did not suggest any possible higher symmetric space group. By using restraints of geometry and ADPs for all ligands, R value is 0.2199 before *SQUEEZE* treatment and 0.0815 after *SQUEEZE* treatment. The squeezed void volume was 13731 $Å^3$, equivalent to 74.1% of the unit cell (Figure III. 3d).

Validation Reply Form

PROBLEM: Ratio Observed / Unique Reflections too Low .... 21 Perc.

RESPONSE: Experiments were performed on Bruker SMART APEXII Diffractometer with Mo X-ray tube. Unfortunately, the diffraction from the crystal was very weak and there were almost no reflections after 2Theta=40deg, even after we used data collection

time 90s/frame. This can be explained by the presence of large molecule unit and empty pores (74% void ratio). Also, the plate shape (thin thickness) of the crystals is bad for collection of certain hkl, which is the dominant reason to make the average intensity inaccurate.

3.3.1.4 Refinement Details of MOP 4 (953694)

Diffraction frames were integrated in Tetragonal I by APEX2. Since we knew that MOP **1** is constructed with *I*4/*m*, we were trying to solve this structure with the same space group. The heavy Fourier peaks and rough ligand shape could be seen in the initial Fourier difference map. After geometry was fixed atom by atom, *PLATON* were performed to seek higher symmetry, but no suggestions were proposed. We obtained R value is 0.2202 before *SQUEEZE* treatment and 0.1353 after *SQUEEZE* treatment. The squeezed void volume was 13337 $Å^3$, equivalent to 59.4% of the unit cell (Figure III. 6).

3.3.1.5 Refinement Details of MOP 4′ (953695)

Since the metathesis occurred on MOP **4**, we started this job analogous to MOP **4** structure solution. As expected, the metal-metal bond length of the M_2 units in the core turned to be 2.560 Å, while that in the shell remained 2.217 Å. Based on CCDC database, 2.560 Å is the typical distance from Cu to Cu in a Cu-Cu paddle wheel; in contrast, 2.217 Å is similar to Mo-Mo quadruple bond length. From this clue, around 88% of M_2 units in the core and 6% in the shell were refined as Cu by *SHELX*. For two metal atoms sharing the same site with identical thermal ellipsoids, the xyz and U_{ij} parameters may be equated using the EXYZ and EADP constraints respectively. However, the anisotropic solution failed to converge even when DAMP 5000 was

applied. For reducing the calculation loading of this refinement, the metal composition was determined with the support of element analysis namely SEM-EDS. Mo/Cu ratios are about 1.1, remaining consistent with two samples soaked in $Cu(NO_3)_2$ solution for 6 hours and 2 days. We assigned 100% Cu for the inside M_2 units and 20% Cu for the outside ones on account of simplicity. Consequently, the structure solution was successfully converged with $Mo_{6.4}Cu_{5.6}$.

Validation Reply Form

PROBLEM: Ratio Observed / Unique Reflections too Low .... 17 %

RESPONSE: Experiments were performed on Bruker SMART APEXII Diffractometer with Mo X-ray tube. Unfortunately, the diffraction from the crystal was very weak and there were almost no reflections after 2Theta=40deg. Even after we collected data with 80s/frame and operated the initial measurement to a range up to 26 deg/ 2Theta, it did not help. Nevertheless, the refined structure has a unique reflection-to-parameter ratio of 60.27. (10609 unique reflections, 176 parameters). We believe this proposed structure is well determined. This alert can be explained by the presence of large molecule unit but empty pores.

3.3.1.6 Refinement Details of Cu Coordination Polymer (953696)

Diffraction frames were integrated in Monoclinic P by APEX2. *XPREP* further pointed out that 2_1 screw axis and *c*-glide plane exist based on statistics of systematic absence. $P2_1/c$ was the only choice which is well-transformed to get Fourier peaks by direct method. By using restraints of geometry and ADPs for all solvent molecules, R value is 0.0441 without *SQUEEZE* (Figure III. 7).

3.3.1.7 The Difference between Space Group of 1 and 2

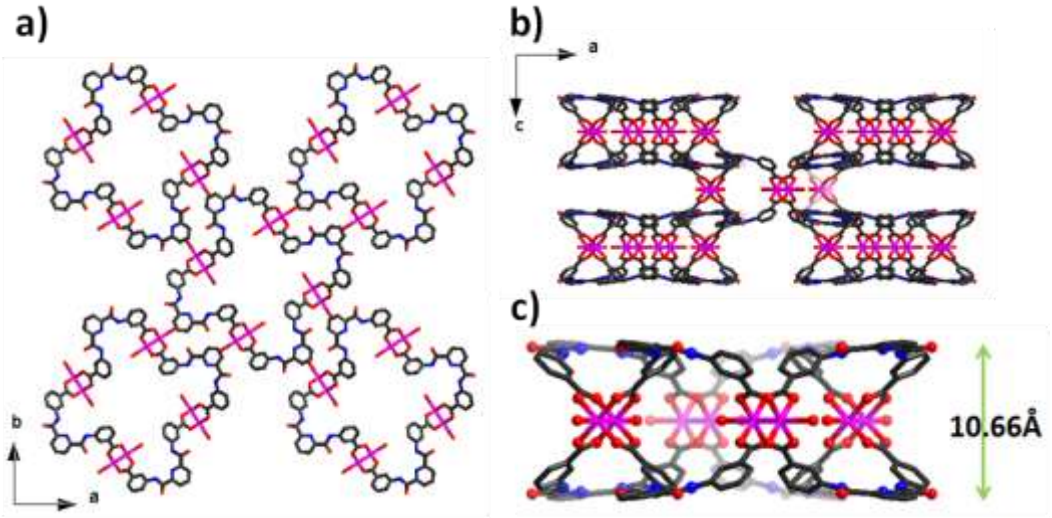

Figure III. 4 Detailed architectures of molecular square 1. H atoms of the ligands were omitted for clarity. The color schemes: Mo, pink; O, red; N, blue; C, black.

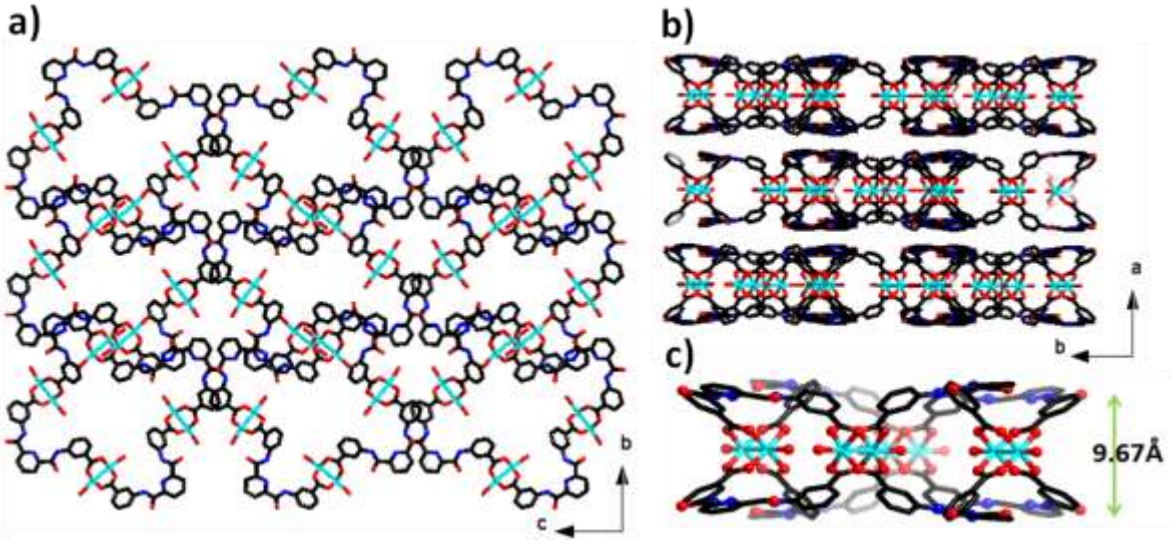

Figure III. 5 Detailed architectures of molecular square 2. H atoms of the ligands were omitted for clarity. The color schemes: Cu, cyan; O, red; N, blue; C, black.

Singular MOPs of **1** and **2** are isostructural (Figure III. 4 and Figure III. 5), derived from four M_2 units coordinated with four pairs of γ-L^1 ligands, which is kinetically trapped at low temperature. The sizes of the molecules are 11.1 and 10.9 Å in the edge length of the M_2 units in equilateral squares of **1** and **2**, respectively. This slight inequality of molecule sizes is originated from the M_2 unit dimensions, which is 2.1 Å for Mo-O bond and 1.9 Å for Cu-O bond. Regardless of the similarity of these two MOP units, **1** is packed in *I4/m* whereas 2, in *Cmce*. As can be seen in Figure III. 4 and Figure III. 5, MOP **1** crystalized with *I4/m* space group is located in alternate layers, but MOP **2** with *Cmce* is arranged parallel. The heights along *c*-axis are 10.66 and 9.67 Å for **1** and **2**, respectively, inferring that Mo-molecular squares have more space to be "hooked" by another unit than Cu-molecular squares do. However, the difference between these two architectures might not only be induced by the "thickness" of the molecular squares, but also affected solvent species.

The single crystal density and void volume ratio (fraction of void volume to total volume) of Mo-molecular squares are 0.695 g/cm^3 and 67.7% (13337/19691= 67.7%), while those of Cu ones are 0.703 g/cm^3 and 65.1% (23739/36493=65.1%). It agrees that single crystal **1** contains more considerable solvent-accessible void space, as also observed directly from Figure III. 4 and Figure III. 5. However, the BET and Langmuir surface area of **1** is 92.9 and 282.34 m^2/g, and those of **2** is 139 and 471 m^2/g, respectively. This inconsistency between void volume ratio and surface area comes from the relative position shift among individual MOP units after sample activation.

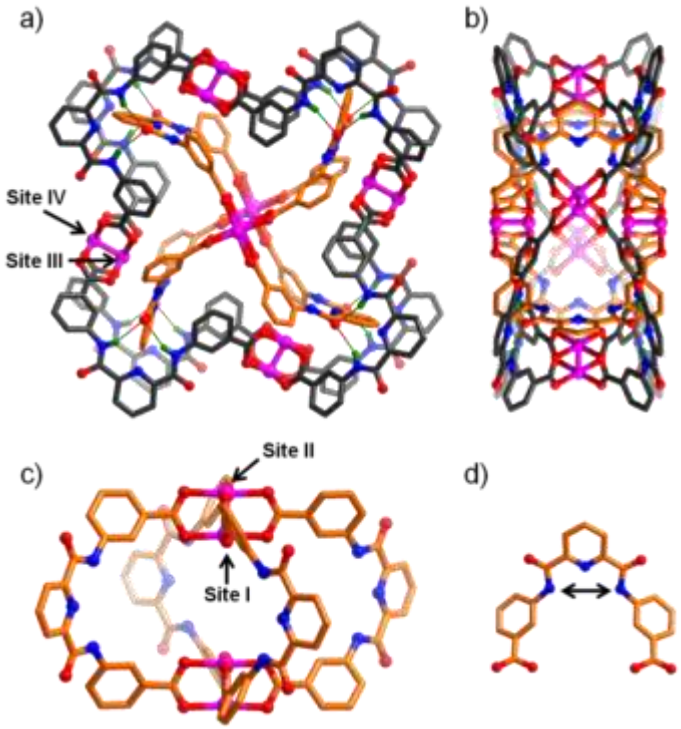

Figure III. 6 (a) and (b) Structure of the core-shell molecular assembly 4 viewed from the *c* direction and *a/b* directions, respectively (H-bond interactions are shown in thin green/red bonds); (c) structure of the core molecular cage in 4; and (d) α-L^1 in the core of 4. Figures (a) and (c) also show sites I, II, III, and IV of Mo_2 units. Color scheme: Mo, pink; O, red; N, blue; H, dark green; C, black (in shell) or orange (in core).

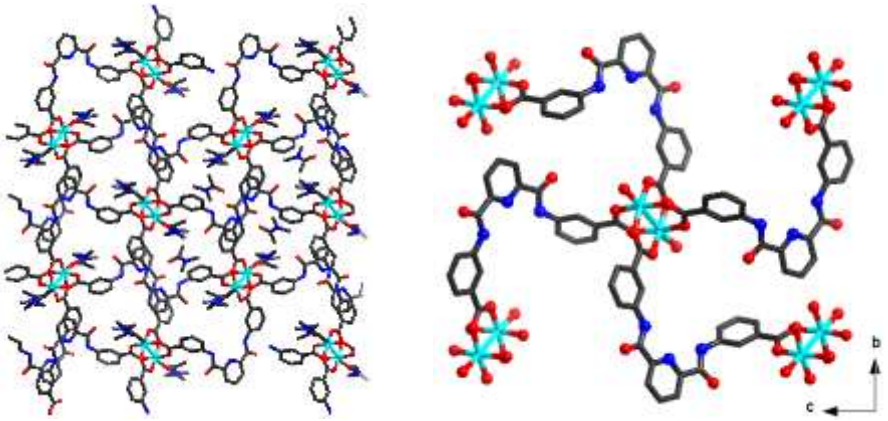

Figure III. 7 Structures of 2-dimensional coordination polymer 5, in which the L^1 ligands adopt a γ conformation. H atoms of ligands were omitted for clarity. The color schemes: Cu, cyan; O, red; N, blue; C, black.

3.3.2 Atomic Displacement Parameters and Reactivity

Thermal ellipsoids, namely atomic displacement parameters, can be expressed by a 3 x 3 tensor, which defines scale and direction of atomic vibration with respect to three principle axes and their cross-correlations.[50-51] In crystallography, it devotes either six anisotropic U_{ij} components or one isotropic B-factor (both in $Å^2$) to characterize the displacement of each atom. Besides thermal motion, the B-factor could be regarded as spreading of electron diffusion around their equilibrium positions on account of positional disorder.[52] Comparing different sites located in the same structure, atoms with low B-factors come from a well-ordered texture while those with high B-factors, a more flexible part.[53] Since the flexibility and mobility of enzyme's active sites might adopt more than one conformation, which is linked to the protein's functions, biochemists have analyzed B-factors for enzyme activity.[51-52, 54] This phenomenon encourages us to investigate MOP reactivity by B-factor analysis. For convenience, we analyze U_{ij} instead of B-factor.

The U_{ij} tensor, anisotropic displacements, could be regarded as a Gaussianly distributed ellipsoid. The relative dimensions of an ellipsoid could be determined by diagonalizing the ADP matrices.[55] The resulting eigenvalues (λ_i) define the mean-square atomic fluctuations, whereas eigenvectors represent the three principal axes of the ellipsoids. The matrices of mean square atomic displacements U_{ij} (in $Å^2$) could be written as $\begin{bmatrix} U_{11} & U_{12} & U_{13} \\ U_{21} & U_{22} & U_{23} \\ U_{31} & U_{32} & U_{33} \end{bmatrix}$, where $U_{ij} = U_{ji}$ due to symmetric tensor. The observed U_{ij} values were simply extracted from single crystal data, as following:

$$ADP_{(4/core/site\ I)} = \begin{bmatrix} 0.07058 & 0 & 0 \\ 0 & 0.07058 & 0 \\ 0 & 0 & 0.04670 \end{bmatrix} \quad [3.1]$$

$$ADP_{(4'/core/site\ I)} = \begin{bmatrix} 0.07730 & 0 & 0 \\ 0 & 0.07730 & 0 \\ 0 & 0 & 0.09610 \end{bmatrix} \quad [3.2]$$

where site I is the inside one of the M_2 unit in core entity while site II, outside one (Figure III. 6).

Comparing [3.1] and [3.2], it is noticed that, for metal sites in the core entity, the magnitudes of U_{11} and U_{22} are similar for both compounds whereas those of U_{33} show significant difference. U_{33}, standing for the electron spreading along the third principal axis, is more strictly confined than the other two. Since the third principal axis of the thermal ellipsoid of core atoms happens to be the crystallographic *c*-axis as well as the orientation of Mo-Mo quadruple bonds, it is expected to show less electron diffusion along this direction. Supposedly, after metathesis by Cu, the U_{33} should be increased, approaching to U_{11} and U_{22} values, owing to weaker Cu-Cu attractive force than Mo-Mo attractive force. From the single crystal data, we observed that U_{33} clearly increases no matter what metal is assigned. Evidence coming from the thermal parameter's change is in agreement to the tension release along the *c*-axis (Mo-Mo bond direction) after Cu substitution. (Note: the crystallographic axes are not necessarily the principal axes of the ellipsoid, it is only true for $U_{ij} = 0$, $i \neq j$.)

The tension release could be observed not only in core entities but also in shell entities. However, the tensor forms are more complicated. Since the U_{ij} values are not zero in the matrices of shell entities, we cannot simply figure out the ellipsoid axes from

the ADP tensors (see Table III. 2). In order to obtain the ellipsoid's parameters, we overlapped the observer's coordinates and ellipsoid principal axes using diagonalization of matrices. The eigen values (λ_i) and eigen vectors were calculated for the ADP matrices; then, the diagonalization of matrice could be given as $\begin{bmatrix} \lambda_1 & 0 & 0 \\ 0 & \lambda_2 & 0 \\ 0 & 0 & \lambda_3 \end{bmatrix}$.

$$\text{ADP}_{(4/\text{shell/site III})} = \begin{bmatrix} 0.14359 & 0.01641 & 0 \\ 0.01641 & 0.08439 & 0 \\ 0 & 0 & 0.11898 \end{bmatrix} \quad [3.3]$$

$$\text{ADP}_{(4'/\text{shell/site III})} = \begin{bmatrix} 0.10077 & 0.00986 & 0 \\ 0.00986 & 0.10804 & 0 \\ 0 & 0 & 0.14346 \end{bmatrix} \quad [3.4]$$

$$\text{Diagonalization of ADP}_{(4/\text{shell/site III})} = \begin{bmatrix} 0.14781 & 0 & 0 \\ 0 & 0.08016 & 0 \\ 0 & 0 & 0.11898 \end{bmatrix} \quad [3.5]$$

Corresponding eigen vectors are [3.72, 1, -0.09], [-0.26, 1, 0], [-0.67, 1, -2278] for eigen values are 0.14781, 0.08016, 0.11898, respectively.

$$\text{Diagonalization of ADP}_{(4'/\text{shell/site III})} = \begin{bmatrix} 0.11491 & 0 & 0 \\ 0 & 0.09390 & 0 \\ 0 & 0 & 0.14346 \end{bmatrix} \quad [3.6]$$

Corresponding eigen vectors are [0.69, 1, 0], [-1.46, 1, 0.01], [0.23, 1, 71.00] for eigen values are 0.11491, 0.09390, 0.14346, respectively.

Applying the same calculation to site IV of **4** and **4′**, we obtained:

$$\text{Diagonalization of ADP}_{(4/\text{shell/site IV})} = \begin{bmatrix} 0.15550 & 0 & 0 \\ 0 & 0.10637 & 0 \\ 0 & 0 & 0.12818 \end{bmatrix} \quad [3.7]$$

$$\text{Diagonalization of ADP}_{(4'/\text{shell/site IV})} = \begin{bmatrix} 0.15866 & 0 & 0 \\ 0 & 0.10824 & 0 \\ 0 & 0 & 0.13688 \end{bmatrix} \quad [3.8]$$

where the U_{ii} values represent the true mean square atomic displacements related to the corresponding ellipsoid semi-axes, which appear to be the eigen vectors.

Unlike how the stress in the core entity is released along *c*-axis, the tension behaves more complicatedly for the shell entity. Ellipsoid volume is employed to describe this problem. It is found that $(\lambda_1\lambda_2\lambda_3)^{1/2}$ (relative term to ellipsoid volume) of **4′** is always larger than that of **4** at all sites, implying that the electron locations become more flexible after Cu substitution. In detail, from Figure III. 8, it shows that in **4** the ellipsoid of core entity are more compressed than that of shell entity, indicating Cu substitution prefers these stressed positions in core entity. After metathesis, site II releases the stress (Figure III. 9), enlarging the ellipsoid, demonstrating that it is the driving force directing Cu substitution.

$$Ellipsoid\ volume = \frac{4}{3}\pi\lambda_1\lambda_2\lambda_3 \qquad [3.9]$$

Further investigation for the stressed orientations is depicted in Figure III. 10. As can be seen, at site III, the blue ellipsoid, which describes the mean square ADP in shell part of **4′**, is roughly spherical, representing the electrons are evenly distributed with no marked preference in *a*-*b* plane. In contrast, the pink ellipsoid, the mean square ADP with respect to **4**, is flattened along the direction with intersection angle 6° off *a*-axis. It shows that the stressed ellipsoid at site III recovers itself in *a*-*b* plane and transfers the ellipsoid deformation to *c*-axis instead after metathesis. However, there is no pronounced change in *a*-*b* plane and *c*-axis at site IV after Cu substitution (Figure III. 9). The tension release is equally distributed in all directions.

It is concluded that the tension primarily releases along the *c*-axis (metal bond direction) at the core entity while it partially releases along [-1.46, 1, 0.01] direction and *c*-axis (the direction perpendicular to shell entity's metal bond) at the shell entity. A useful calculator for eigen vectors: http://easycalculation.com/matrix/eigenvalues-and-eigenvectors.php

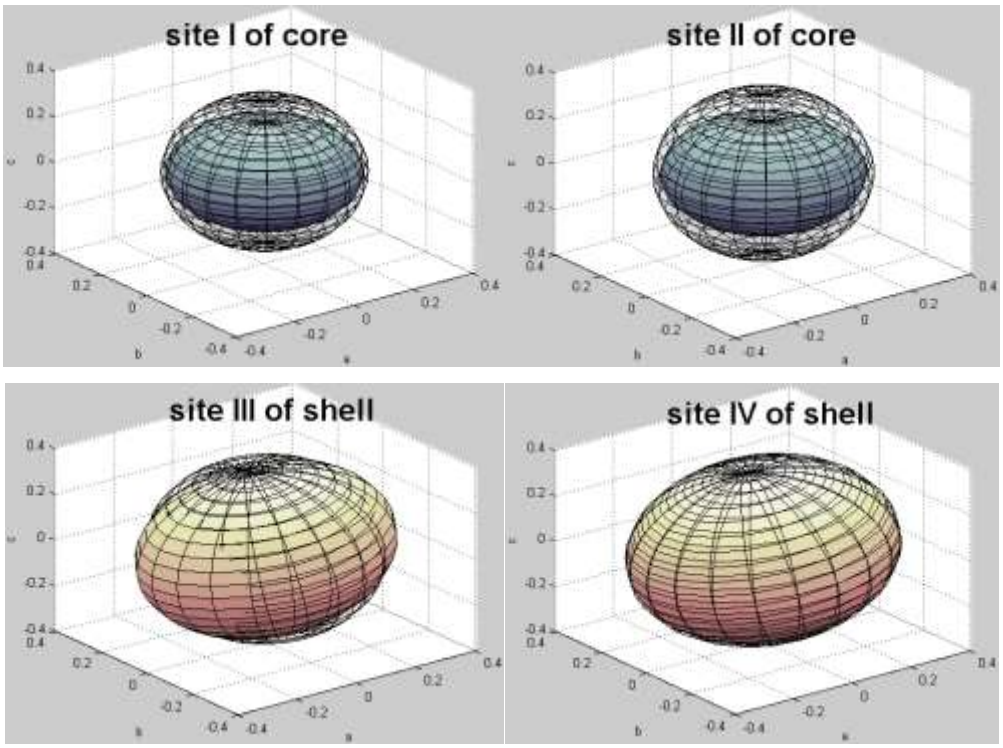

Figure III. 8 The stressed ellipsoid volume differences of site I, II, III, and IV in 4 (colored ellipsoid) and 4′(transparent ellipsoid).

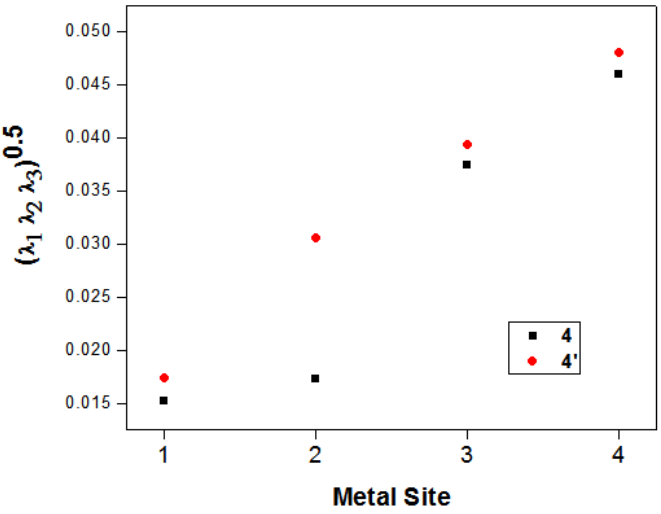

Figure III. 9 The stressed ellipsoid volumes of site I, II, III, and IV in 4 and 4′.

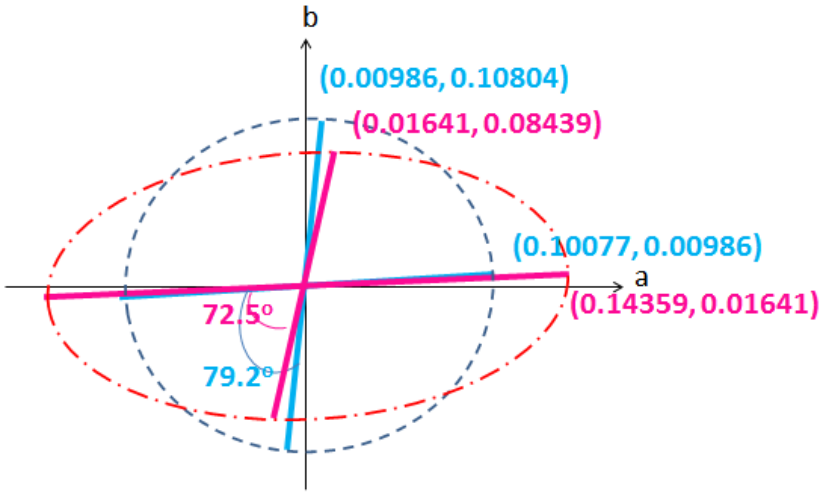

Figure III. 10 Pink ellipsoid and blue ellipsoid at site III are viewed along *c* direction for core-shell molecular assembly **4** and **4′**, respectively. The observer's coordinate axes are black. The vectors were extracted from ADP tensors, representing mean square atomic displacements instead of true amplitudes for enhancement of stress difference.

Table III. 2 Anisotropic atomic displacement parameters for 4 and 4′.

Compound	position	U_{11}	U_{22}	U_{33}	U_{23}	U_{13}	U_{12}
4 (Mo-Core-Shell)	Site I core	0.07058	0.07058	0.04670	0.00000	0.00000	0.00000
	Site II core	0.07692	0.07692	0.05090	0.00000	0.00000	0.00000
	Site III shell	0.14359	0.08439	0.11898	0.00000	0.00000	0.01641
	Site IV shell	0.15502	0.10685	0.12818	0.00000	0.00000	-0.00483
4′ (Mixed-Core-Shell)	Site I core	0.07730	0.07730	0.09661	0.00000	0.00000	0.00000
	Site II core	0.08870	0.08870	0.11927	0.00000	0.00000	0.00000
	Site III shell	0.10077	0.10804	0.14346	0.00000	0.00000	0.00986
	Site IV shell	0.12694	0.13996	0.13688	0.00000	0.00000	0.02436

3.3.3 Core-Selective Metathesis

The core-selective metathesis observed in the compound 4 (Mo→Cu, Figure III. 11a-c,) could be attributed to the several reasons. First, a close inspection of the packing of the core-shell structure from both the crystallographic *a* and *b* directions reveals that the site II of the Mo_2 units in the core are directly accessible from a 1-D channel (Figure III. 11e). Even with axial ligands on the two Mo atoms, there is still enough space for solvated Cu^{2+} ions to easily reach the Mo_2 units, which is why the exchange reaction is fast. In fact, once the Cu salt was added, an immediate color change of the crystal was observed. The M_2 units in the shell (sites III and IV), on the other hand, are not directly accessible due to the coordinated ligands.

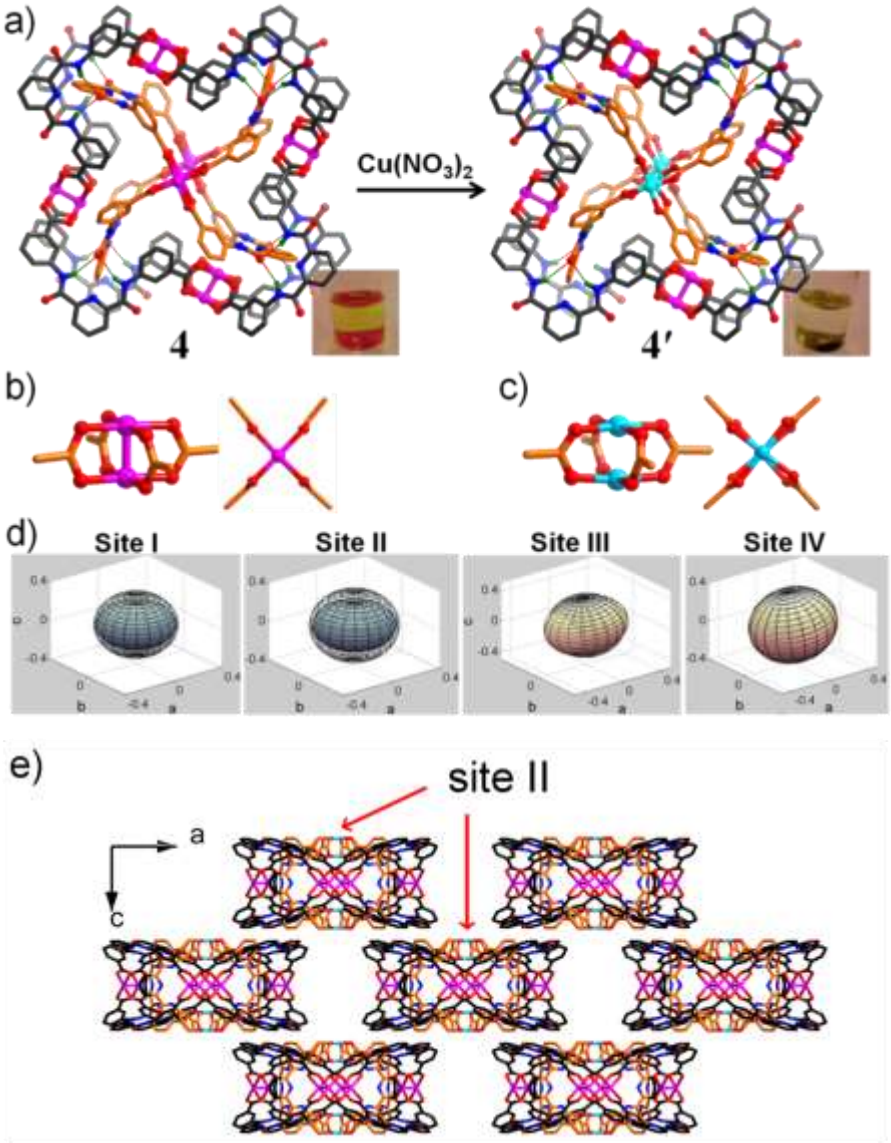

Figure III. 11 (a) Metal ion metathesis in core-shell assembly 4 to give 4′. Photographs show the color change of the crystals from red orange to dark green during the metathesis; (b) and (c) views of the paddlewheel metal-carboxylate centres in the core cages of 4 and 4′, respectively. Color scheme: Mo, pink; Cu, cyan; O, red; N, blue; H, black green; C, black (in shell) or orange (in core). (d) Thermal ellipsoids before (colored) after metathesis (transparent) at site I, II, III, and IV. (e) The close packed structure of 4′viewed along –*b* axis.

We postulate that during the metathesis reaction, the quadruply bonded Mo_2 units must be solvated and then Cu^{2+} ions replace them. The excess Cu^{2+} ions could then participate in the shell metathesis. The shell metathesis, however, was not complete. Once the 1:1.1 molar ratio of Cu:Mo has been reached (Figure III. 12, Figure III. 13 and Table III. 3), either elongating the reaction time (2 weeks) or increasing the concentration of Cu^{2+} solution did not lead to further metathesis. Mn^{2+} /Ni^{2+} /Co^{2+} /Zn^{2+} solutions do not precede metathesis with Mo_2 units, Figure III. 14 and Table III. 4.

This phenomenon can be described by a process of thermodynamic equilibrium. It has been reported that metal centers connected by flexible ligand environments can participate in competing equilibria due to environmental conditions and cation identity.[56-57] For the core, the α-**L**$^{\mathbf{1}}$ ligand produces stress on the Mo_2 units, which energetically favors relatively flexible Cu_2 units to release their tension. We believe the quadruply bonded Mo-Mo species, which is positionally locked due to orbital symmetry, prevents the release of this tension. As there is no bond in the Cu_2 unit, the torsional strain can be relieved by a twist in the core conformation. In contrast, the shell possesses less stress than the core does thus a partial substitution between the Mo_2 units and Cu^{2+} ions is enough to release their tension.

Anisotropic atomic displacement parameters (ADP, $U_{ij,}$) of the metals in **4** and **4′** were analyzed in order to confirm the complete metathesis in the core and partial one in the shell. ADP, namely thermal ellipsoids, could be regarded as spreading of electron diffusion around their equilibrium positions on account of positional disorder, inverse-proportionally reflecting confinement of atoms.[58-60] It can be quantified and compared

by the ellipsoid volumes proportional to multiplicity of eigenvalues of the ADP matrices. In Figure III. 11d, the volume of thermal ellipsoids before metathesis at site III and site IV is obviously larger than that at site I and site II. Since the thermal ellipsoids reflect local flexibility of a structure, which is potentially related to the reactivity[59-60], Figure III. 11d implies that the reactivity of the four sites is different. As a result, the Mo_2 units at site I and II have constrained thermal motion of the electrons, like a compressed spring, thus being more reactive. Graphically, the shape of the thermal ellipsoids at site I and II transformed from flat ellipsoids to spherical ellipsoids after metathesis, indicating a release of the torsional strain along *c*-axis. In addition, the H-bonds stabilized the core structure during the metal substitution process, resulting in the selective substitution of the core without the collapse of the cage. It should be pointed out that the direct synthesis for such a heterobimetallic molecular assembly from Cu^{2+} and Mo^{2+} mixtures yielded amorphous powders. Consequently, the core-shell assembly can be used as a template for other hereobimetallic molecular assemblies. The site-specific metal substitution provides a good synthetic strategy to broaden the structures of coordination driven molecular assemblies, which are difficult to access through the direct assembly process. Furthermore, the preparation of the heterobimetallic molecular assemblies is a meaningful step in realization of enzyme-mimetic supramolecules. In biological systems, various heterometallic complexes are involved in cooperative enzymatic reactions.[61-62]

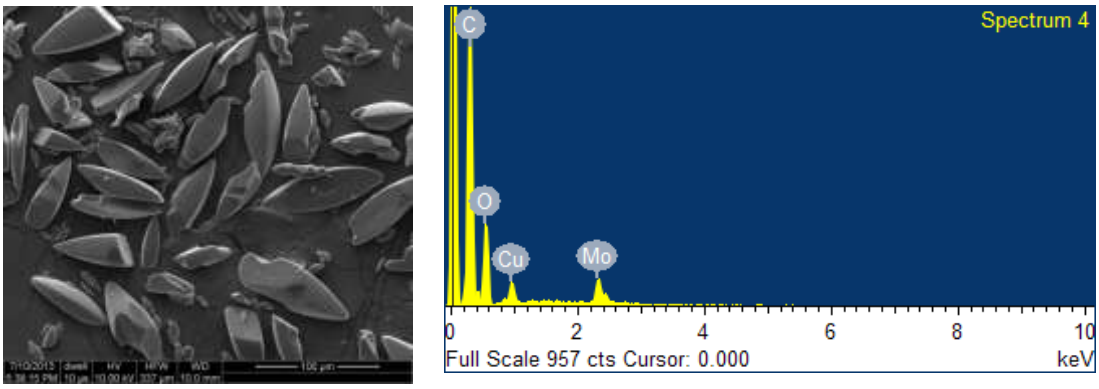

Figure III. 12 SEM image (left) and SEM-EDS spectrum (right) of **4′**.

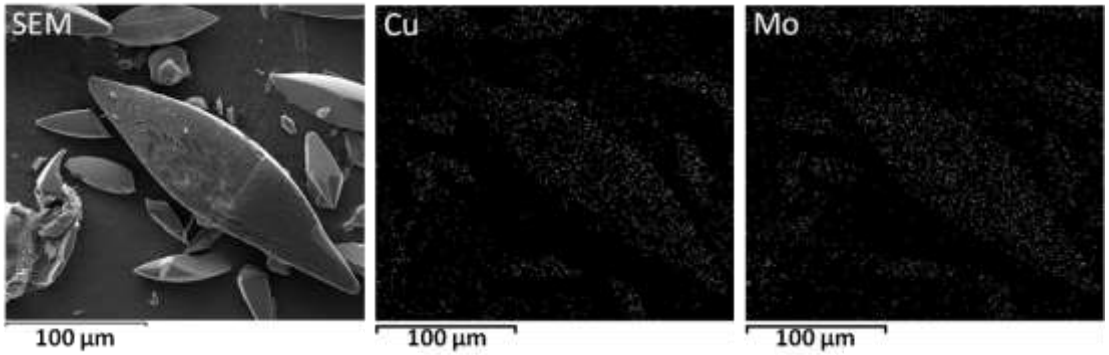

Figure III. 13 SEM-EDS analysis of 4′: SEM image (left), EDS mapping picture of Cu (middle), and Mo (right).

Table III. 3 SEM-EDS data for Cu^{2+} exchange.

		Metathesis for 6 hrs			Metathesis for 2 days				
Dried sample	Cu	1.31	1.41	1.68	1.22	1.02	1.39	1.25	1.54
	Mo	1.41	1.32	1.74	1.3	0.96	1.66	1.23	1.96
	Mo/Cu	1.08	0.94	1.04	1.07	0.94	1.19	0.98	1.27
	Average	1.016			1.092				
Ground sample	Cu	1.61	1.31		1.46	1.51	1.28		
	Mo	1.94	1.64		1.25	1.82	1.61		
	Mo/Cu	1.21	1.25		0.86	1.21	1.26		
	Average	1.229			1.106				

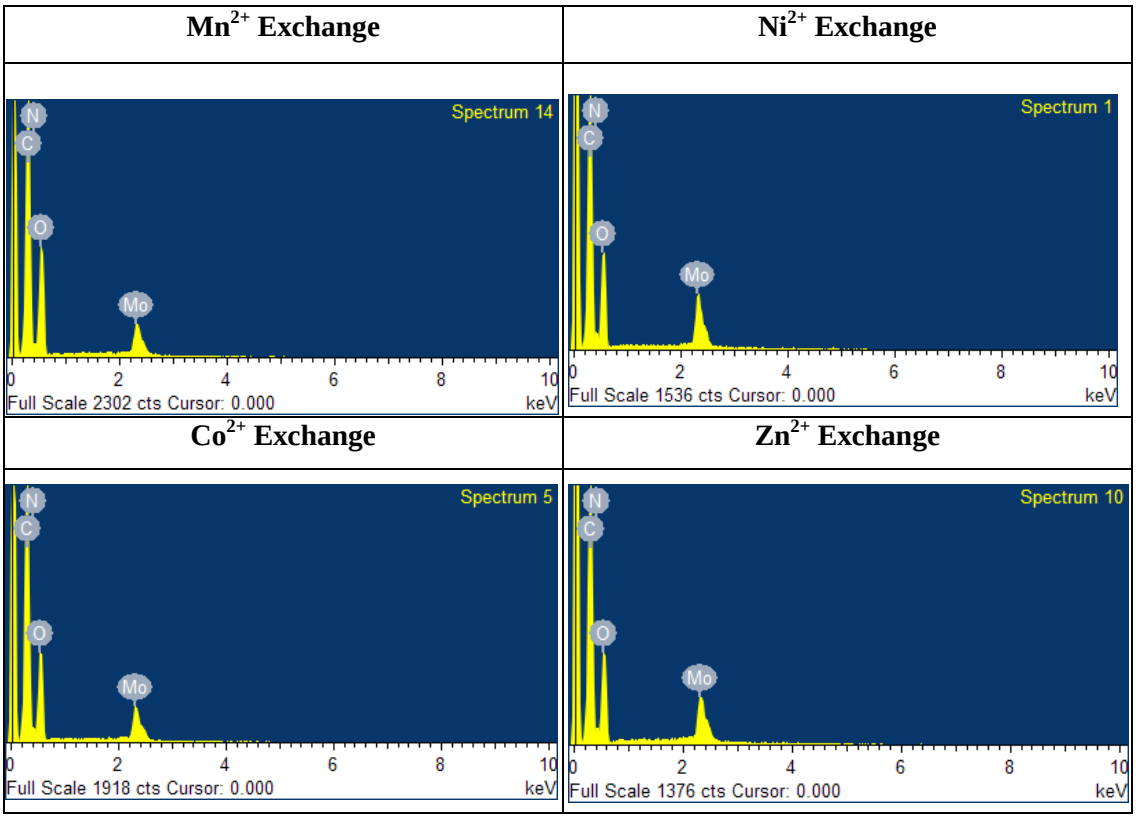

Figure III. 14 SEM-EDS data for Mn^{2+}/ Co^{2+}/ Ni^{2+}/ Zn^{2+} exchange for 2 days.

Table III. 4 SEM-EDS data for Mn^{2+}/ Co^{2+}/ Ni^{2+}/ Zn^{2+} exchange for 5 days.

	Metathesis for 5 days			
Mn (Atomic %)	0	0	0	
Mo (Atomic %)	2.72	2.55	2.87	
Mo/Mn	-	-	-	
Co (Atomic %)	0.19	0.18	0.48	
Mo (Atomic %)	2.99	2.90	2.79	
Mo/Co	15.7	16.1	5.8	
Ni (Atomic %)	0.26	0	0.10	0.11
Mo (Atomic %)	2.99	3.00	2.90	3.18
Mo/Ni	11.5	-	29.0	28.9
Zn (Atomic %)	0.21	0.14	0.20	0.21
Mo (Atomic %)	2.81	2.55	3.01	2.72
Mo/Zn	13.4	18.2	15.1	13.0

3.4 Conclusion

A series of molybdenum- and copper-based MOPs was synthesized through coordination-driven process of a bridging ligand and dimetal paddlewheel clusters. Three conformers of the ligand exist with an ideal bridging angle between the two carboxylate groups of 0^o ($H_2\alpha$-$\mathbf{L^1}$), 120^o ($H_2\beta$-$\mathbf{L^1}$), and of 90^o ($H_2\gamma$-$\mathbf{L^1}$), respectively. At ambient or lower temperature $H_2\mathbf{L^1}$ and $Mo_2(OAc)_4$ or $Cu_2(OAc)_4$ were crystallized into a molecular square with γ-$\mathbf{L^1}$ and Mo_2 /Cu_2 units. With proper temperature elevation, not only the molecular square with γ-$\mathbf{L^1}$ but also a lantern-shaped cage with α-$\mathbf{L^1}$ formed simultaneously. Similar to how Watson-Crick pairs stabilize the helical structure of duplex DNA, the core-shell molecular assembly possesses favorable H-bonding interaction sites, dictated by the ligand conformation in the shell, which facilitate the formation and stabilization of the central lantern shaped core which was not observed without this complementary interaction. Based on the crystallographic implications, a heterobimetallic cage was obtained through a post-synthetic metal ion metathesis, showing different reactivity of coordination bonds in the core and shell. As an innovative synthetic strategy, the site-selective metathesis broadens the structural diversity and properties of coordination assemblies.

CHAPTER IV

CHARACTERIZATION: POWDER X-RAY DIFFRACTION APPLIED TO OBSERVE ADSORBED GAS REDISTRIBUTION IN METAL-ORGANIC FRAMEWORKS[*]

4.1 Introduction

Metal-Organic Frameworks (MOFs), a family of advanced porous compounds, have been considered a promising candidate for CO_2 capture and CH_4 storage.[63-64] Superior in porosity and customizability to the conventional zeolite materials, desired architectures of MOFs can be easily tailored by elegant choice of metal clusters and organic linkers.[65] Accordingly, perceiving which structural characteristics contribute to high gas uptake is of critical importance in the design of materials with better adsorption ability.[66-67] There have been several endeavors to develop this fundamental knowledge: density functional theory (DFT),[68-72] molecular simulations,[73-76] and powder neutron diffraction experiments.[73, 77-80, 81-85] Unfortunately, some discrepancies were found between these reports, arising from different methods or force fields adopted in computational simulations. On the other hand, neutron diffraction successfully identified the precise adsorption sites in several classical MOFs, yet most diffraction experiments were done below CH_4 condensation temperatures (111K),[77-79] which might not reflect real gas behaviors under practical conditions.

[*]Reproduced with permission from Chen, Y.-P.; Liu, Y.; Liu, D.; Bosch, M.; Zhou, H.-C., "Direct Measurement of Adsorbed Gas Redistribution in Metal-Organic Frameworks", *J. Am. Chem. Soc.*, 137 (8), 2919–2930, **2015**. Copyright 2015 by American Chemical Society.

Granted that some mechanisms are proposed accurately in certain MOF systems, in practice, MOFs do not simply sit in these static and monotonous situations.[86] MOFs can be potentially used under a wide range of environments, such as in the flues of power plants and cold chambers of NGV cylinder tanks (Natural Gas Vehicle).[64] Even a specific system might undergo several state shifts in one working cycle. It is possible that structural features can be beneficial for one stage but harmful in another stage. Moreover, MOF regeneration requires a process of pressure and/or temperature change to desorb gases. How the gas kinetic behaviors facilitate a fast and complete thermodynamic equilibrium of adsorption/desorption remains an unexplored field, even though understanding gas kinetics in MOFs may allow significantly more effective design.[86]

In an attempt to overcome the drawbacks of the investigation methods mentioned above, chronological Differential Electron Density (DED) maps were three-dimensionally visualized for the positional evolution of guest molecules under reasonable ambient conditions. This structure envelope concept has been applied in identifying the guest molecules in crystalline adsorbents,[87] distinguishing the positively and negatively charged ions,[88] separating interpenetrated MOF networks,[89] and detecting diffusion of indicator molecules.[90] In this article, we particularly focused on elucidating the time- and temperature-dependence of gas kinetics in MOFs. Synchrotron-based X-ray measurements were necessarily employed due to the insufficient resolution of regular diffractometers. For this time-resolved diffraction structure envelope (TRDSE) method, we took sequential X-ray exposures on a crystal under specific gas atmospheres,

recording a series of powder patterns as a function of gas-loading time and temperatures. It can be seen that the intensity of certain (*hkl*) reflections was increased or decreased due to electron scattering from these gas molecules adsorbed on the corresponding (*hkl*) planes. Intersections of several (*hkl*) planes are able to correlate to structural features in the unit cell of MOFs; hence, the preeminent adsorption sites were pronounced. Combining this with an adequate statistical cut-off level for the series of DED maps, different maps are objectively compared.

Four gas kinetic processes were successfully observed via DED interpretation (Figure IV. 1), which is the first example of experimental crystallographic measurement of gas migration. Additionally, we explore a general consequence of thermodynamics for the gas kinetics in MOFs. These measurements reveal how the guest molecules conduct the redistribution over the host framework surfaces to reach the minimum of free energy. Our studies also show that the open metal sites and the window openings emphasized in earlier efforts are not always so crucial.[68-69, 78-79] The entropic driving force, appropriate accessibility, and the gas-gas interactions might be as or more important than the binding sites with unscreened Coulomb force or van der Waals force under certain conditions.

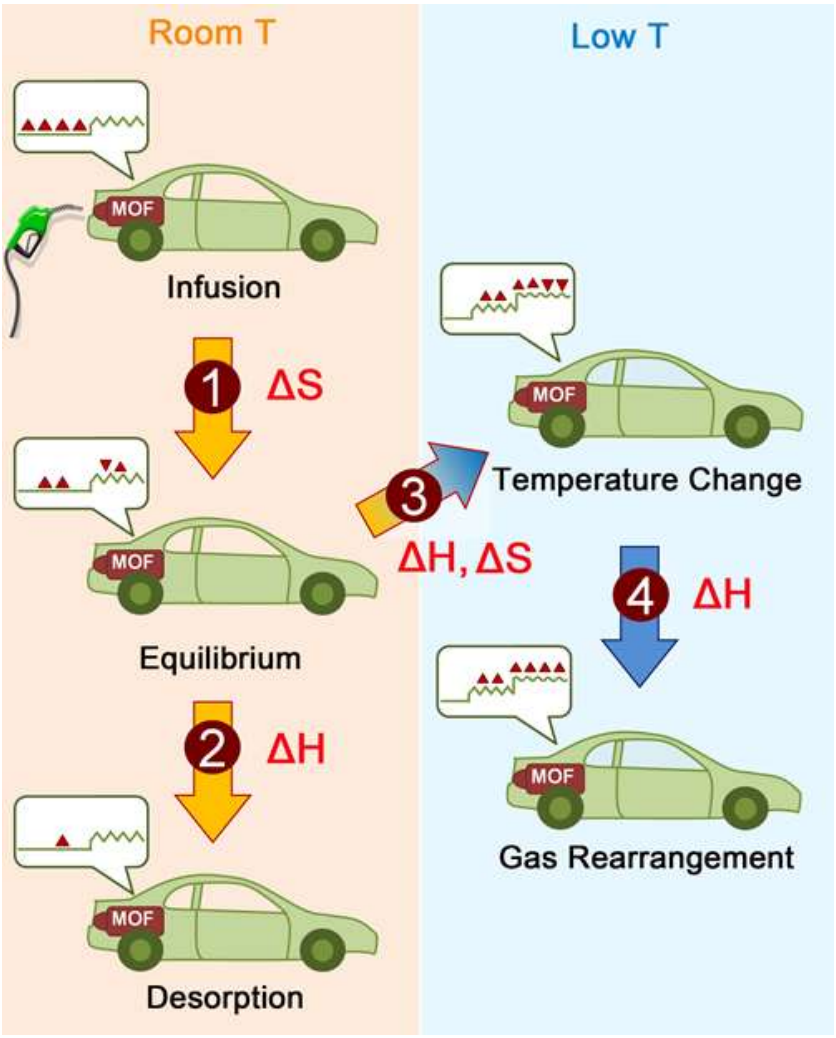

Figure IV. 1 Four CH_4 kinetic processes taking place in MOFs were observed in our work: (1) kinetic transition during the gas infusion period, (2) desorption residues, (3) molecular redistribution upon temperature change, and (4) gas-gas interactions at low temperature. Process 1 is entropically driven, while processes 2 and 4 are enthalpically driven. The molecular distribution over various energetic sites on MOF surfaces is depicted in the dialogue boxes, which will be explained below. The orientations of the triangles conceptually denote the orientations of gas molecular arrangements. Similar work about CO_2 behavior can be found later.

4.2 Methodology and Theory

Differential Electron Density (DED) maps are 3-D iso-surfaces, which are constructed of the differences between two structure envelopes. Building a structure envelope is a procedure to describe crystal structures with hyperbolic surfaces.[88-91] These surfaces can be mathematically expressed by a Fourier summation with structure factor phases φ_{hkl} and the normalized structure factor amplitudes $|E_{hkl}|$ of a few selected reflections (*hkl*), which are given by:[92]

$$\rho(x,y,z) = \sum_{hkl}|E_{hkl}|\cos[2\pi(hx+ky+lz)-\varphi_{hkl}] \qquad [4.1]$$

where ρ(x,y,z) denotes the electron density distribution of the structure envelope. Structure envelopes also divide a unit cell into areas of rich and deficient electron density. In the MOF field, this contrast surface characterizes the framework atoms as appearing on the positive side and the pore spaces on the negative side.[93] Furthermore, envelope surfaces assembled by Fourier series are derived as fundamental invariants of structured matter.[89, 92] This means that if the crystallographic symmetry and unit cell parameters remain unchanged, the sheathing envelope will still be similar.

Accordingly, an observed porous crystal filled with various gas molecules should have an analogous envelope to its reference model. The difference between these two envelopes (ρ_{obs} and ρ_{ref}) comes from the electron scattering of gas molecules, which is written as [87]

$$\rho_{gst} = \rho_{obs} - k\rho_{ref} \quad [4.2]$$

where k is the scaling factor defined as the quotient of maximum values of ρ_{obs} and ρ_{ref}. The contouring of ρ_{gst} , according to the DED map, will constitute a 3-D distribution in the unit cell, visualizing the position of the guest molecules.

In this work, the electron scattering of gas molecules in all examples is only responsible for the amplitude changes of certain reflections, not for phase switching. Note that the TRDSE method is only valid when there is a negligible breathing effect [94] or phase transition in the framework on gas adsorption. Therefore, the structure factor phase will be fixed for both ρ_{obs} and ρ_{ref} while the structure factor amplitudes will be replaced with $|E_{hkl}{}^{ref}|$ for ρ_{ref} and $|E_{hkl}{}^{obs}|$ for ρ_{obs}. The operational details will be described in the next section.

4.3 Experimental Section

4.3.1 MOF Synthesis and Activation*

Four MOF compounds, HKUST-1,[95] PCN-12,[96] and PCN-306 / PCN-307 [97] were chosen as representatives for their exceptional CH_4 uptake and diverse structural features of interest, such as open Cu(II) sites, window pockets, cage corners and empty cages (Figure IV. 2 and Figure IV. 4). All compounds were crystallized according to the original procedures, followed by solvent exchange with methanol and dichloromethane, and then vacuumed at 150℃ for 10 hours. These Cu-MOFs changed from blue to purple, exhibiting successful solvent removal from the Cu_2 units. The activated crystals were preserved in dichloromethane before diffraction experiments.

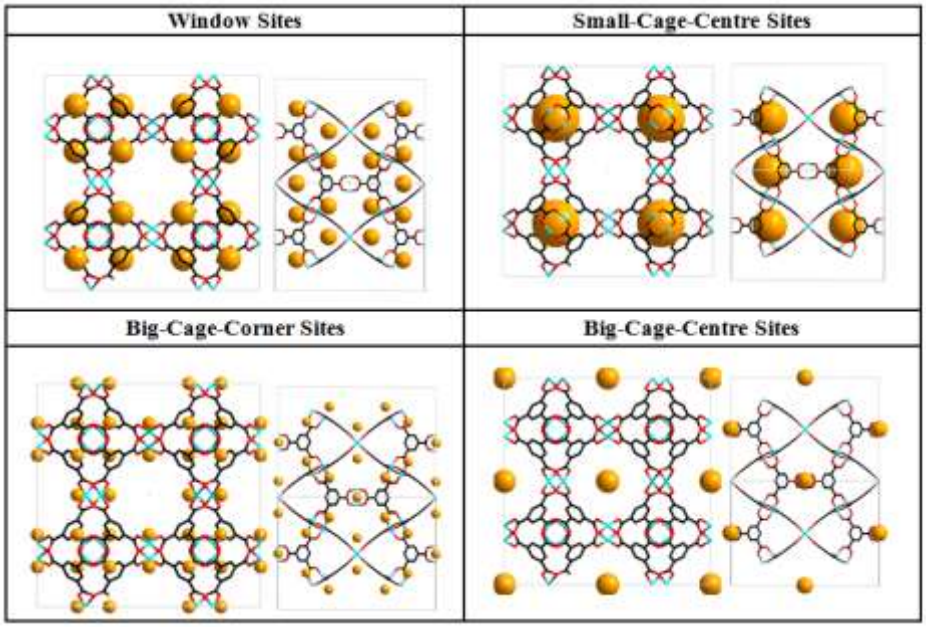

Figure IV. 2 Definition of adsorption sites in HKUST-1.

*PCN-306/ PCN-307 (Figure IV. 3) were synthesized by Dr. Yangyang Liu.

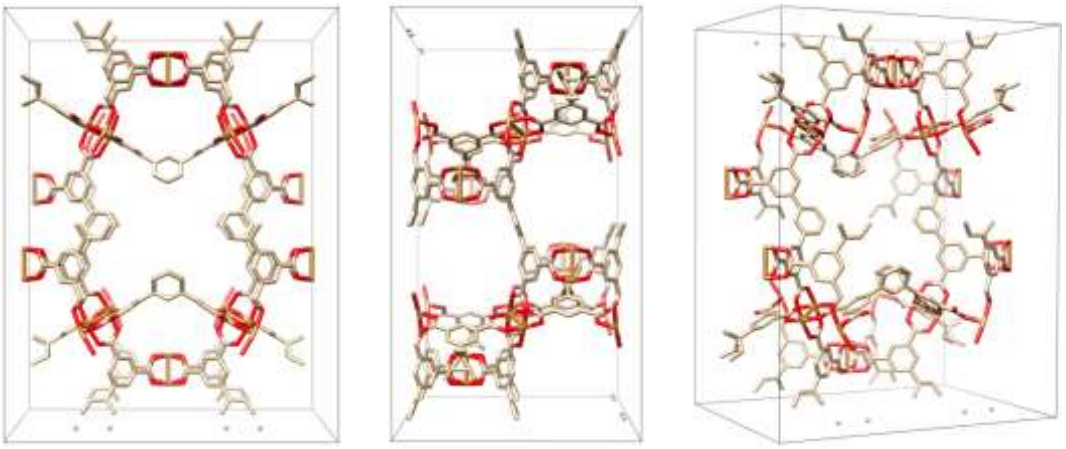

(a)

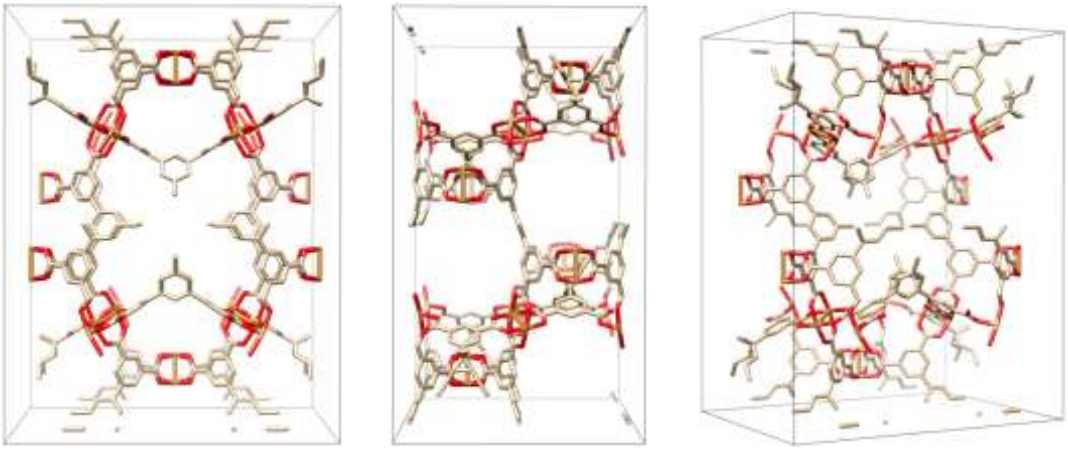

(b)

Figure IV. 3 The crystal structure of (a) PCN-306 and (b) PCN-307.

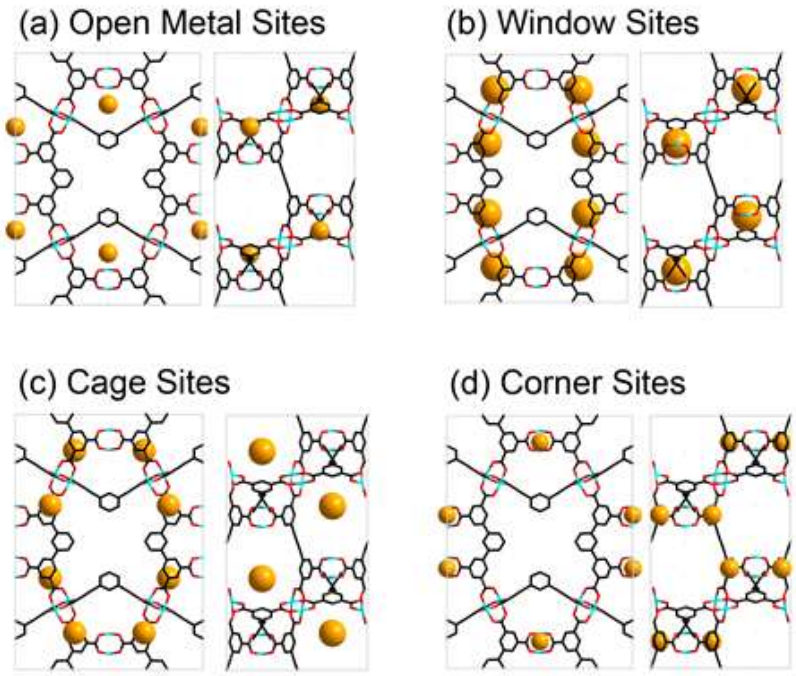

Figure IV. 4 Common structural features in MOFs: (a)-(d) Definition of four adsorption sites for PCN-306, viewed along the *c*-axis (left) and *a*-axis (right). The copper, oxygen and carbon atoms are cyan, red and black respectively. The hydrogen atoms are omitted for clarity.

4.3.2 Experimental Setup and Data Collection

In situ synchrotron-based powder diffraction experiments were performed at the 17-BM beamline of the Advance Photon Source in Argonne National Laboratory (IL, USA). The incident beam wavelength was 0.72959 Å for HKUST-1, 0.72808 Å for PCN-12, and 0.72910 Å for PCN-306/ PCN-307 (Figure IV. 3), respectively. The ground powdery samples were packed in a 0.8 mm inner diameter polyimide capillary installed on a flow-cell.[98]

Before PXRD data collection, the samples were activated at 423K for an hour to evacuate coordinated water molecules. An intensity-2θ pattern was diffracted from the flow cell and then collected at 295, 200, and 150 K under an atmosphere of He (as reference and flush), CO_2, and CH_4. In each gas loading period, patterns were recorded by sequential exposures at an interval of 30 seconds taking 10-20 minutes to obtain a kinetic process. A Perkin-Elmer amorphous-Si flat panel area detector (XRD 1621 CN3-EHS) was set perpendicularly to the beam path. The resulting raw images were processed within Fit-2D, integrating with a step interval of 0.015° (as shown in Figure IV. 5, Figure IV. 6 and Figure IV. 7). An external LaB_6 standard (put in a capillary) was required to calibrate the sample-to-detector distance and tilt angle of the detector relative to the beam.

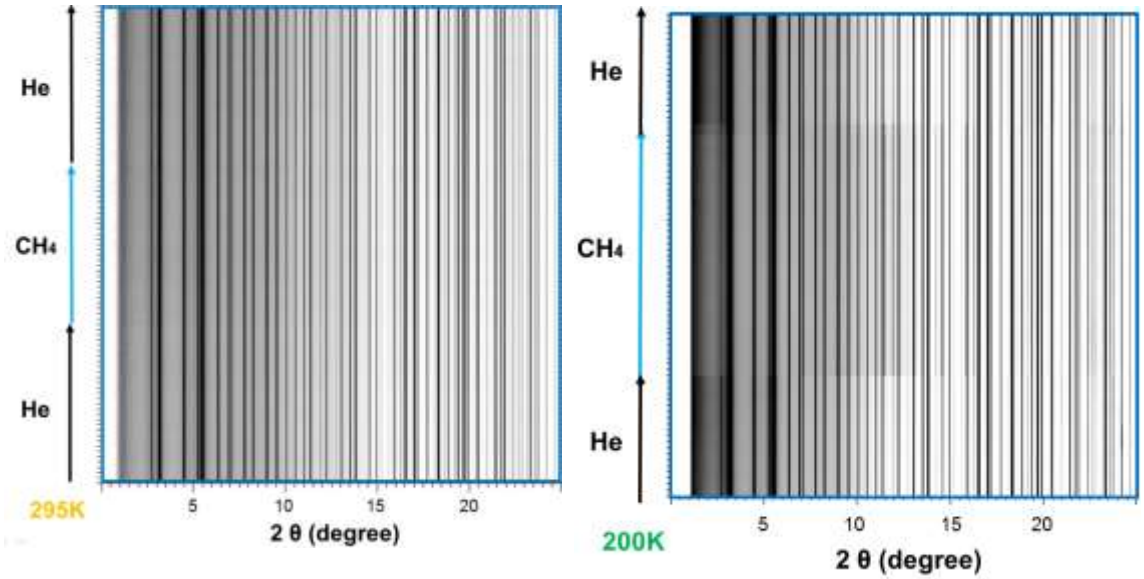

(a) (b)

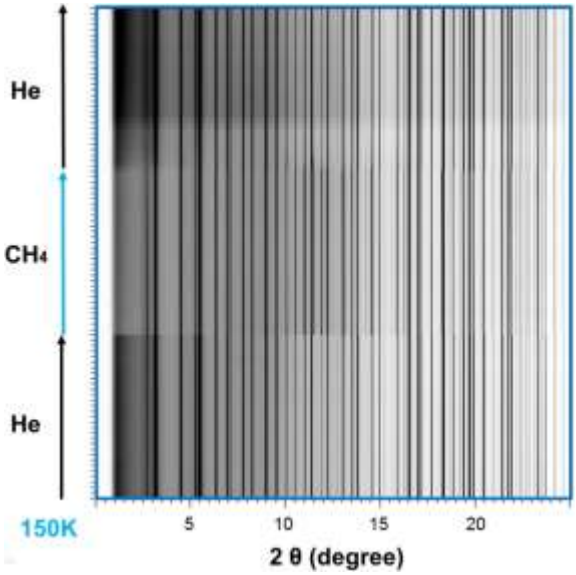

(c)

Figure IV. 5 Top view of the *in situ* gas-loading dependent PXRD patterns of activated HKUST-1, as recorded at (a) 295K, (b) 200K, and (c) 150K.

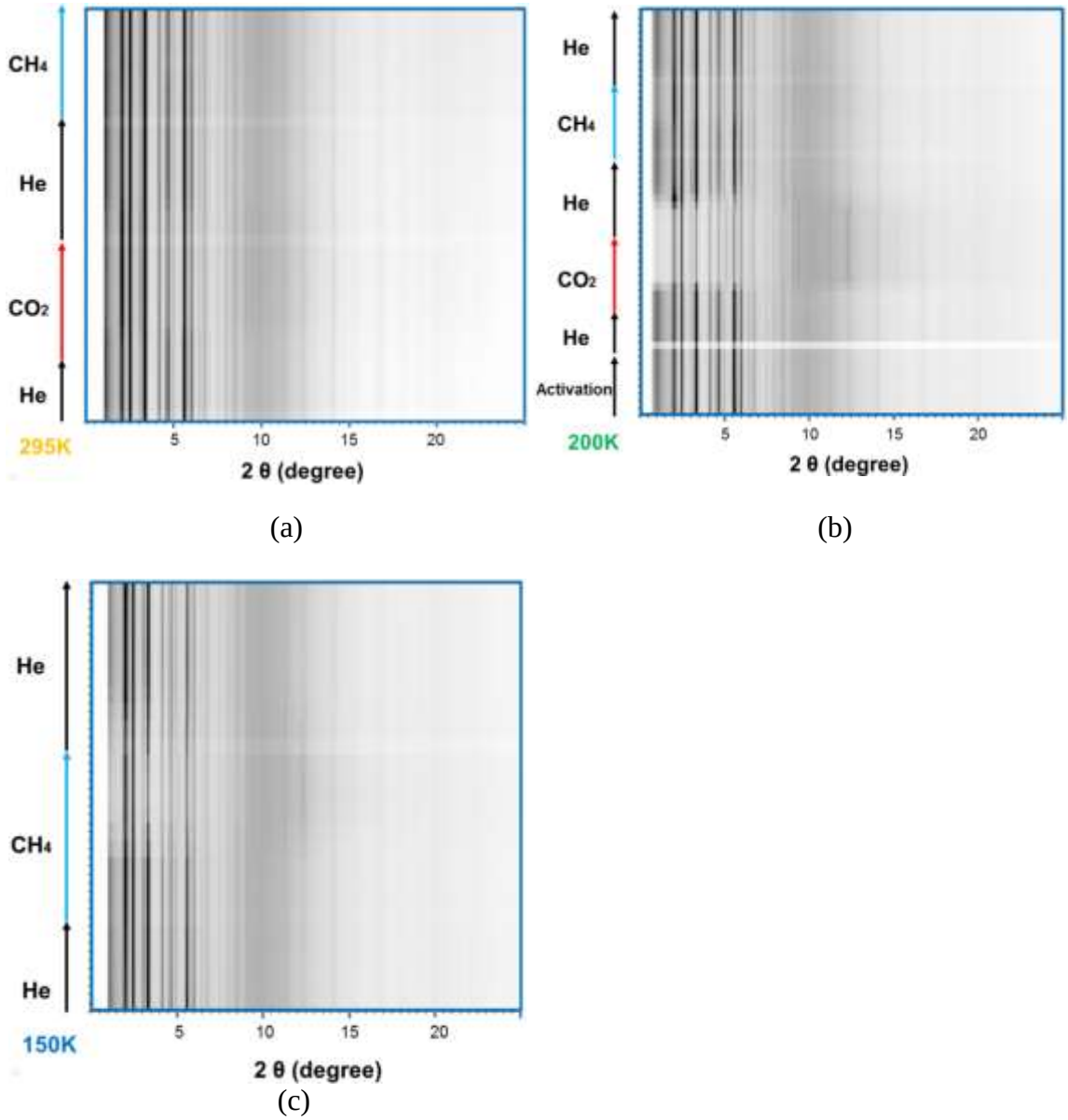

Figure IV. 6 Top view of the *in situ* gas-loading dependent PXRD patterns of activated PCN-306, as recorded at (a) 295K, (b) 200K, (c) 150K.

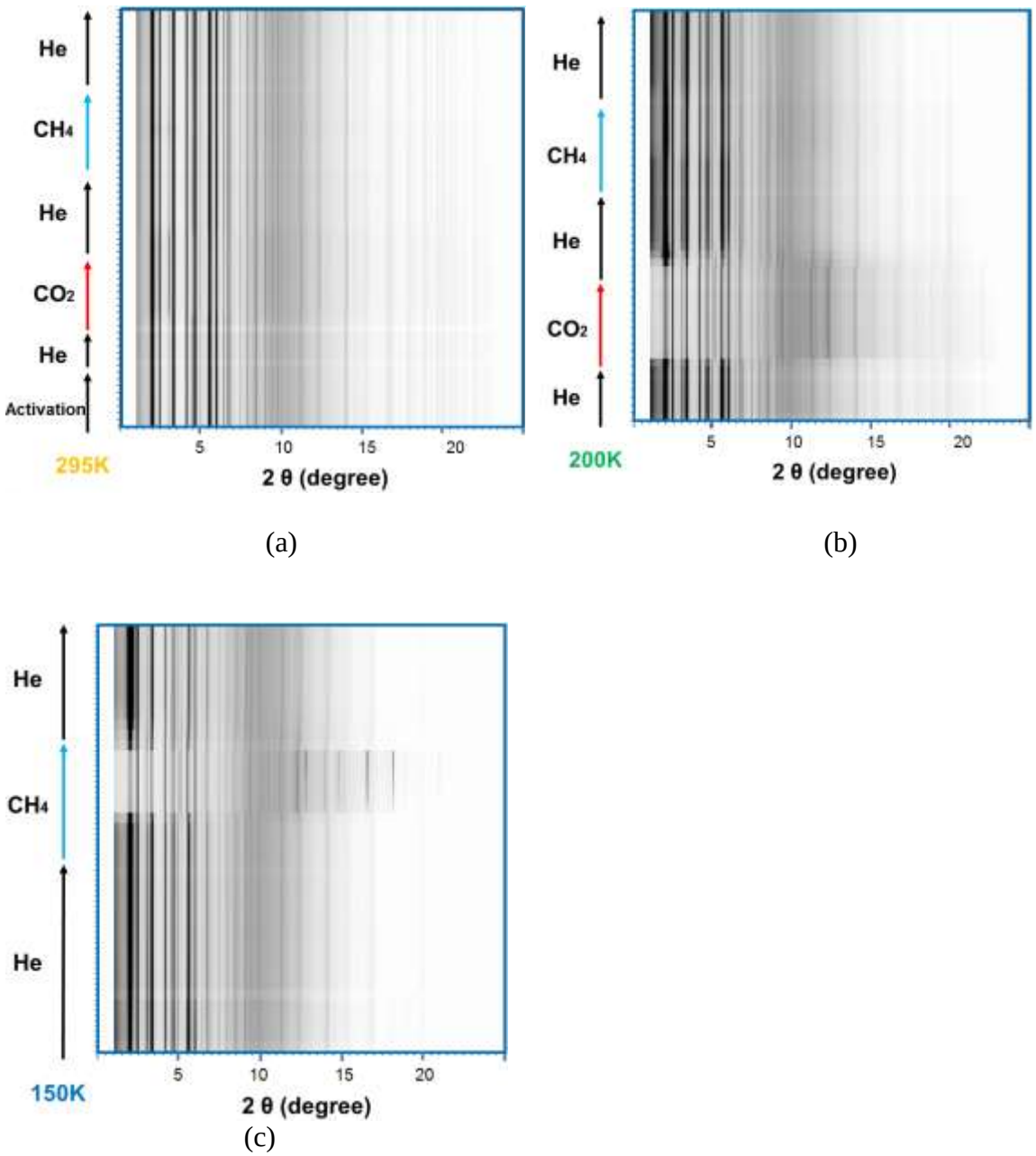

Figure IV. 7 Top view of the *in situ* gas-loading dependent PXRD patterns of activated PCN-307, as recorded at (a) 295K, (b) 200K, (c) 150K.

4.3.3 Amplitude Extraction of $\left|E_{hkl}^{ref}\right|$ and $\left|E_{hkl}^{obs}\right|$ by Le Bail Fitting

According to Eq. 4.1, the normalized structure factor amplitudes $|E_{hkl}|$ and the structure factor phases φ_{hkl} are the two sets of data needed to construct the DED maps. The intensity amplitude of measured PXRD patterns was extracted by Le Bail refinement built in to the *JANA2006* software (.xy file is needed).[99] It also works by using Pawley refinement in commercial software *TOPAS 4.2*, giving similar results for the electron density map.

The refinement steps were described as follows. Data recorded at 2θ smaller than 2° and larger than 16° were ignored. There were no reflections observed in the range of 0~2 degrees. The reflections within 16 degrees are sufficient to describe a molecular distance of 2.6Å, which is much shorter than the kinetic diameter of CH_4 or CO_2.

The pattern backgrounds were modeled with 20-term Legendre polynomials, and the zero shift term was corrected for experiments performed in transmission geometry (Debye-Scherrer form). The refinement of unit cell parameters was initially started from the axial length of the single crystal proposed in the original publications.[95,96,97] The peak profiles were fitted with the pseudo-Voigt function,[100] a weighted sum of a Lorentz and Gaussian function. GU, GV, GW and LX are the halfwidth parameters of Gaussian and Lorentz function, respectively.[100] Note that GV is necessarily negative while others, positive, to avoid negative halfwidths but ensure slightly linear decrease with scattering angles at low 2-θ regions.

Since GW term is the FWHM squared at zero scattering angle bearing clear physical meaning, we prefer refining GW first and accepting a similar magnitude of GW in one series of experiments; in this work, it was supposed to be 3 in the *JANA2006* program. To achieve that, the refining priority of GU, GV and LX depends on the case. The asymmetry parameter was not refined because there should be no asymmetry for this diffraction geometry (Debye ring). As for other refinements, such as preferred orientation and anisotropic broadening were not employed for simplicity. Structure factor amplitudes and the corresponding (*h k l*) values were extracted and indexed from the fitting profile of the intensity pattern; both were exported to an hkl file.

The agreement of Le Bail fittings with the measured data was evaluated by the residuals in final whole pattern decomposition plots (Figure IV. 8), and by the R-factors shown in Table IV. 1. It can be seen that the final unit cell parameters do not shift obviously, denoting no phase transition or material deterioration in the crystal. This is a prerequisite for the systems which can be analyzed with the TRDSE method.

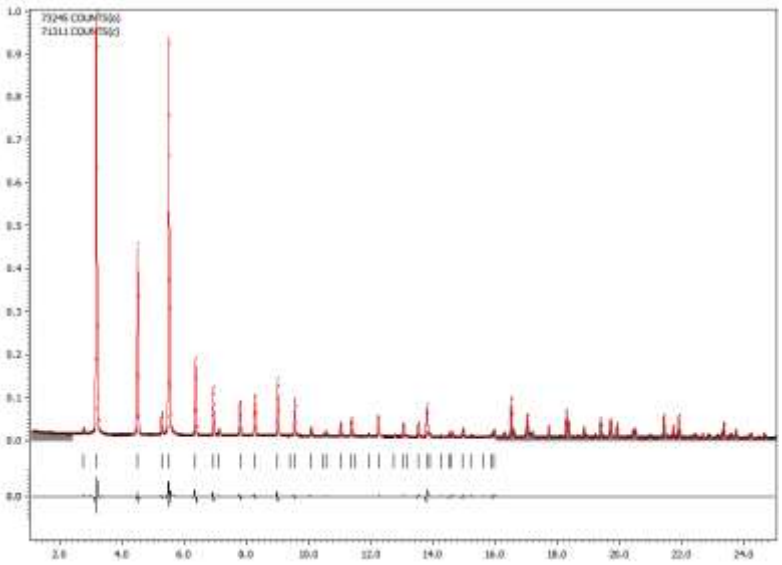

(a)

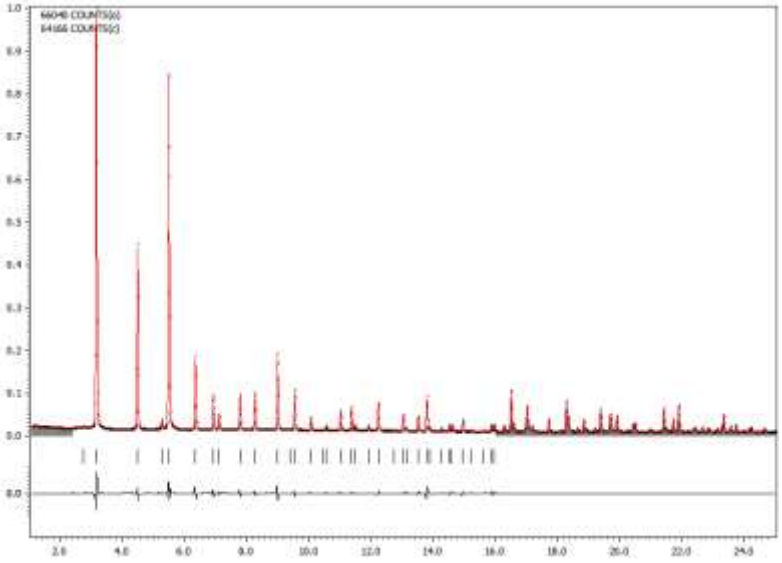

(b)

Figure IV. 8 Measured data and calculated profiles are shown in black points and a red solid line, respectively. The difference is drawn as black curves below the profiles. Tick marks indicate the calculated peak positions of the corresponding compound. This powder pattern was diffracted by HKUST-1 under (a) He, (b) CH_4 atmosphere at room temperature.

Table IV. 1 The summary of the data collection conditions, cell and refinement parameters from the synchrotron powder diffraction performed on HKUST-1 using Le Bail whole pattern decomposition.

Condition	**Gas**	**Time(s)**	**λ(Å)**	***a*(Å)**	***V*(Å^3)**	**GW**	**GoF**	**R_p**	**wR_p**
295K 1 bar	Ref	0	0.72959	26.26	18109	2.64	5.36	8.09	12.91
	CH_4	50	0.72959	26.26	18109	2.65	5.38	8.10	12.94
	CH_4	1500	0.72959	26.26	18109	2.62	5.42	8.06	12.87
200K 1 bar	Ref.	0	0.72959	26.29	18170	2.37	2.67	4.36	6.41
	CH_4	50	0.72959	26.29	18170	2.50	2.59	4.27	6.33
	CH_4	1500	0.72959	26.29	18170	2.41	2.59	4.23	6.30
	He	100	0.72959	26.29	18170	2.46	2.59	4.23	6.19
150K 1 bar	Ref.	0	0.72959	26.28	18150	2.45	2.81	3.91	6.00
	CH_4	50	0.72959	26.30	18191	3.01	2.67	3.72	6.02
	CH_4	1500	0.72959	26.31	18212	2.63	2.64	3.70	5.94
	He	100	0.72959	26.28	18150	2.40	2.64	3.72	5.76
	He	540	0.72959	26.29	18170	2.66	2.77	3.63	5.58

4.3.4 Reflection Selection

Since the main purpose of this study is to observe the distribution change, precision in the interatomic distances and displacement parameters reflected from high angles is not our focal point in this work. In fact, it is also not possible to get high quality data at high 2θ angles, because our study was focused on the states at relatively high temperature (compared with 4K-90K in most diffraction literature), at which the gas molecules are supposed to be highly disordered in the pores. These disorders and scatterings might lead to serious peak overlaps and weak diffractions at high angles, obstructing the accurate determination of the interatomic distances and displacement parameters. Therefore, the envelope difference, a low-resolution ED map, is sufficient to get the rough distributions of guest molecules in this work.

Taking HKUST-1 (space group: $Fm\ \bar{3}m$) as an example, 8 reflections, (1 1 1), (0 0 2), (2 0 2), (1 1 3), (2 2 2), (0 0 4), (3 1 3), (2 2 4) were chosen for fitting surface generation in all gas-loaded crystals (Figure IV. 9 and Table IV. 2). For PCN-306/ PCN-307 (space group: *Cmcm*), 12 reflections, (1 1 0), (0 2 0), (1 1 1), (0 2 1), (2 0 0), (2 2 0), (0 0 2), (1 3 1), (2 2 1), (2 0 2), (3 1 1), (2 4 0), (1 5 0), (0 4 2), and their corresponding phases were chosen for envelope generation in all gas-loading cases (Figure IV. 10, Figure IV. 11, Table IV. 3, Table IV. 4).

The “threshold resolution” has to be calculated as the selection criteria. For example, if the narrowest part of the structure is 5.7Å (the width of the window openings), the threshold will be 2θ of 7.3° that the reflection selection has to go beyond. Note that these reflections (hkl) have to be selected such that all directions in reciprocal

space are represented and that their indices should be lower to avoid serious peak overlap.[91, 101] It is also noted that systematically absent reflections might produce the best surface, which could not be adopted due to the irrational crystallographic models.

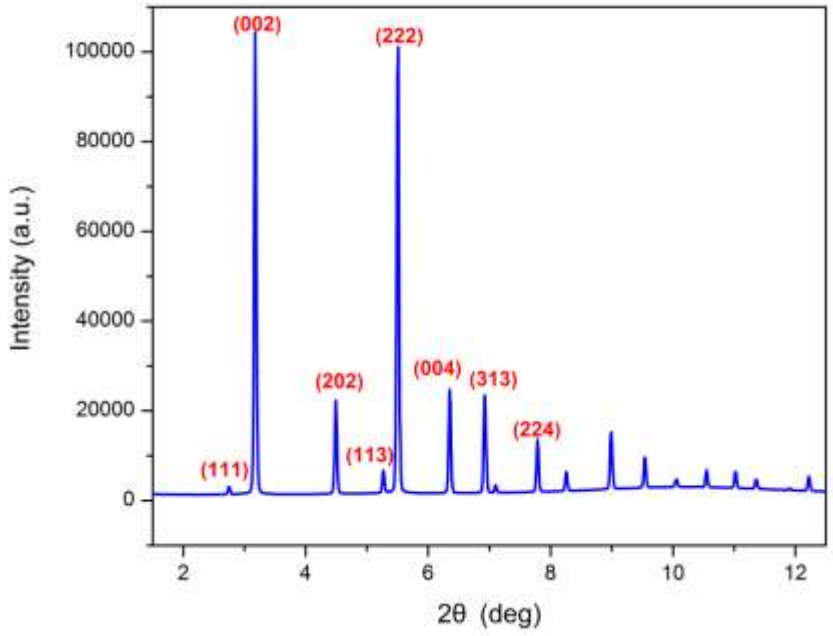

Figure IV. 9 Indexing for the powder pattern of HKUST-1. The structural envelope (fitting surface) is generated by the Fourier summation of the selected reflections and the corresponding phases.

Table IV. 2 The selected reflections and the corresponding phases for the structure envelope generation of HKUST-1.

hkl	1 1 1	0 0 2	2 0 2	1 1 3	2 2 2	0 0 4	3 1 3	2 2 4
φ_{hkl}^{calc}	180	180	180	0	0	0	180	180

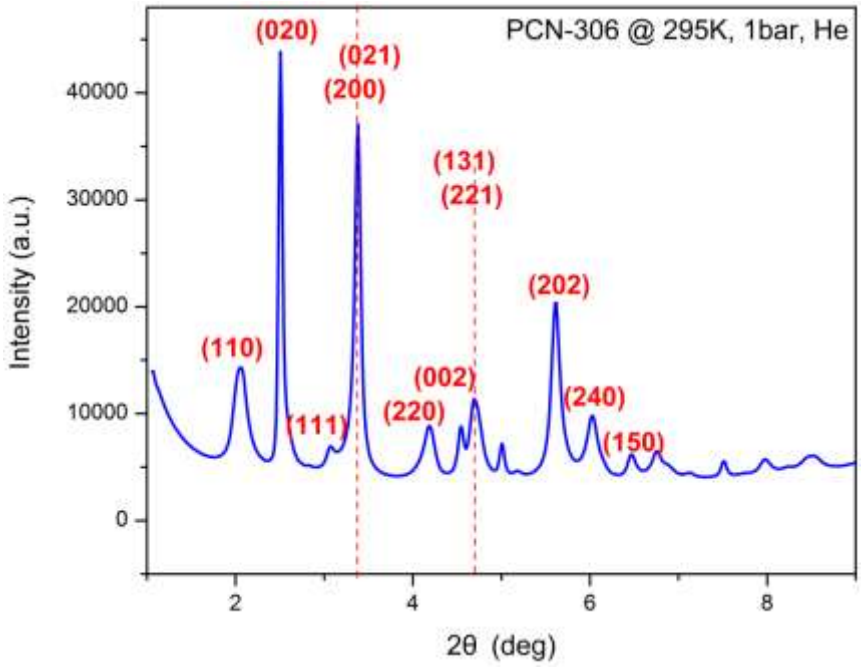

Figure IV. 10 Indexing for the powder pattern of PCN-306. The structural envelope (fitting surface) is generated by the Fourier summation of the selected reflections and the corresponding phases.

Table IV. 3 The selected reflections and the corresponding phases for the structure envelope generation of PCN-306.

hkl	1 0 0	0 2 0	1 1 1	0 2 1	2 0 0	2 2 0	0 0 2	1 3 1	2 2 1	2 0 2	2 4 0	1 5 0
φ_{hkl}^{calc}	180	180	0	180	180	0	0	0	180	180	180	0

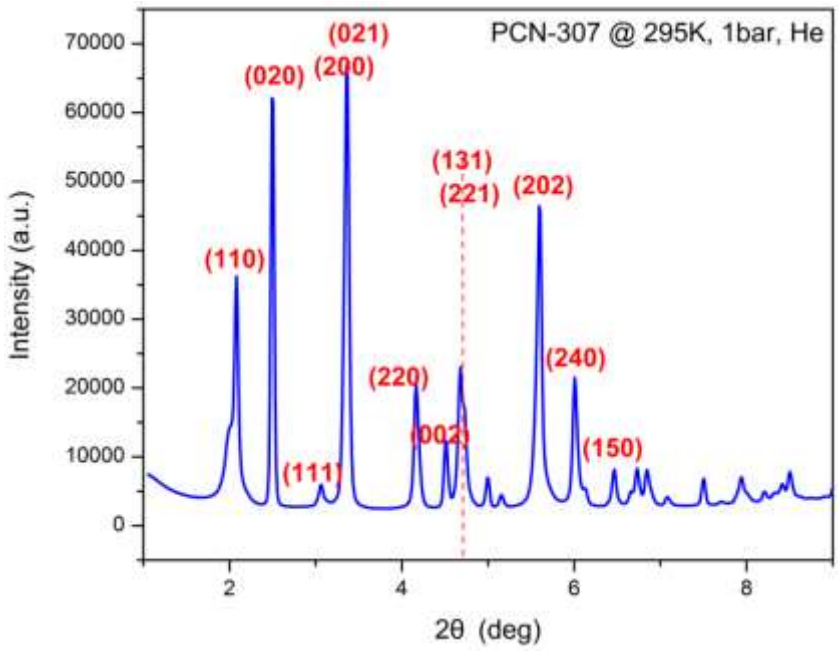

Figure IV. 11 Indexing for the powder pattern of PCN-307. The structural envelope (fitting surface) is generated by the Fourier summation of the selected reflections and the corresponding phases.

Table IV. 4 The selected reflections and the corresponding phases for the structure envelope generation of PCN-307.

hkl	1 0 0	0 2 0	1 1 1	0 2 1	2 0 0	2 2 0	0 0 2	1 3 1	2 2 1	2 0 2	2 4 0	1 5 0
φ_{hkl}^{calc}	180	180	180	0	180	0	0	180	0	180	180	0

4.3.5 Phase Determination

This set of reflections needs to be checked for structure factor phase changes during the investigated process. If the phases are switching, the intensity of that peak will go to zero. In all 4 cases, no reflections disappeared in the PXRD patterns, suggesting the corresponding phases remain the same. The phases were obtained from known MOF structures, for which ideal structure factor phases, φ_{hkl}^{calc} were calculated.[93] As a reliability inspection, it is necessary to overlap the generated envelope with the known crystal model [93] to confirm that no other unreasonable experimental artifacts are introduced.

Ideal structure factor phases φ_{hkl}^{calc} are obtained from a single crystal structure. To construct the tree of phase relationships, a reliable reflection file (.hkl) is required. There are 2 methods to get hkl reflections: an experimental method from measuring single crystals or a simulated method by running the *XFOG* program with an INS-file. A correct INS format file, which could be made from the CIF file deposited in the CCDC database, is critical for *XFOG* to generate an ideal HKL-file (.pow) and ideal squared structure factor F_{calc}^2. Using a HKL-file and INS-file instructed with LIST 2 command, FCF-file will come out with a φ_{hkl}^{calc} list.

4.3.6 Structure Envelopes and Difference of Electron Density

The resulting electron density maps were reconstructed on unit cell grids using the inverse discrete Fourier transform in the *SUPERFLIP* program.[102] An INFLIP setup file for *SUPERFLIP* was initialized by assigning the selected reflection set containing ideal phases and the extracted squared amplitudes (format in Code IV. 1/ Code IV. 2). After the algorithm, a 3-D matrix in XPLOR format representing the electron density, ρ(x,y,z), at each grid point in real space was generated. This is so-called "structure envelope" as shown in Figure IV. 12 and Figure IV. 13. The subtraction of two density maps ($\rho_{obs} - k\rho_{ref}$) and the visualization of the density difference (ρ_{gst}) can be made using *UCSF Chimera* software (calculated command in Code IV. 3).[103-104] The absolute value of ρ_{gst} in the unit of "electrons per Å^3" can be obtained by scaling with the electron density of the framework.[105]

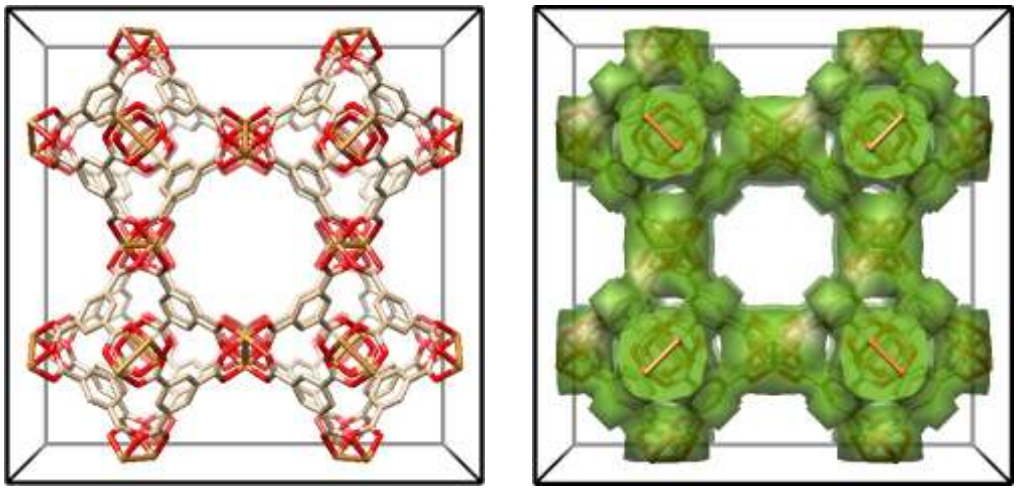

Figure IV. 12 (left) the crystal structure of HKUST-1 viewed along *c*-axis; (right) the structure envelope generated by the selected reflection set of HKUST-1.

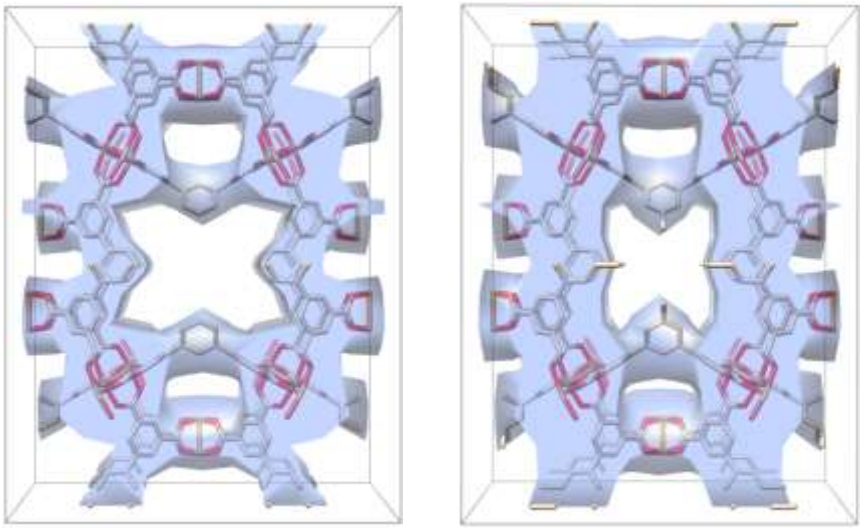

(a) (b)

Figure IV. 13 The structure envelope generated by the selected reflection set of (a) PCN-306 and (b) PCN-307.

Code IV. 1 *SUPERFLIP* setup files (INFLIP-format) used for envelope generation of HKUST-1:

```
title   HKUST1_295K_He envelope from activated powder

# crystallographic data

#----------------------

cell    26.2500   26.2500   26.2500   90.00   90.00   90.00

# spacegroup Fm-3m

spacegroup Fm-3m

centro yes

centers

  0.000000  0.000000  0.000000

  0.000000  0.500000  0.500000

  0.500000  0.000000  0.500000

  0.500000  0.500000  0.000000

endcenters

symmetry

   x1   x2   x3

  -x1  -x2   x3

  -x1   x2  -x3

   x1  -x2  -x3

   x3   x1   x2

   x3  -x1  -x2
```

(Code IV.1 continued)

```
-x3 -x1  x2
-x3  x1 -x2
 x2  x3  x1
-x2  x3 -x1
 x2 -x3 -x1
-x2 -x3  x1
 x2  x1 -x3
-x2 -x1 -x3
 x2 -x1  x3
-x2  x1  x3
 x1  x3 -x2
-x1  x3  x2
-x1 -x3 -x2
 x1 -x3  x2
 x3  x2 -x1
 x3 -x2  x1
-x3  x2  x1
-x3 -x2 -x1
-x1 -x2 -x3
 x1  x2 -x3
 x1 -x2  x3
```

(Code IV.1 continued)

```
-x1   x2   x3
-x3  -x1  -x2
-x3   x1   x2
 x3   x1  -x2
 x3  -x1   x2
-x2  -x3  -x1
 x2  -x3   x1
-x2   x3   x1
 x2   x3  -x1
-x2  -x1   x3
 x2   x1   x3
-x2   x1  -x3
 x2  -x1  -x3
-x1  -x3   x2
 x1  -x3  -x2
 x1   x3   x2
-x1   x3  -x2
-x3  -x2   x1
-x3   x2  -x1
 x3  -x2  -x1
 x3   x2   x1
```

(Code IV.1 continued)

```
endsymmetry
# Grid definition for density maps
#--------------------------------
dimension  3
voxel   AUTO
# control parameters for Superflip run
#----------------------------
maxcycles   200
repeatmode  1
bestdensities  1
outputfile HKUST1_295K_He_25.xplor
expandedlog yes
# Keywords for charge flipping
#----------------------------
perform fourier
delta  AUTO
weakratio  0.0
Biso  0.0
randomseed AUTO
searchsymmetry average
# input data
```

(Code IV.1 continued)

```
#-----------

dataformat intensity phase

fbegin

#   h    k    l      F^2obs       phase

    1    1    1      406.00       0.5

    0    0    2    42924.00       0.5

    2    0    2     9012.00       0.5

    1    1    3     1487.00       0.0

    2    2    2   100000.00       0.0

    0    0    4    39171.00       0.0

    3    1    3    11610.00       0.5

    2    2    4     7467.00       0.5

Endf
```

Code IV. 2 *SUPERFLIP* setup files (INFLIP-format) used for envelope generation of PCN-30X:

```
title   PCN-306_295K_He intensities envelope simulation

# crystallographic data

#----------------------

cell    25.1924   33.4985   18.5795   90.00   90.00   90.00

# spacegroup Cmcm

spacegroup Cmcm

centro yes

centers

  0.000000  0.000000  0.000000

  0.500000  0.500000  0.500000

endcenters

symmetry

   x1   x2   x3

  -x1  -x2   x3+1/2

  -x1   x2  -x3+1/2

   x1  -x2  -x3

  -x1  -x2  -x3

   x1   x2  -x3+1/2

   x1  -x2   x3+1/2

  -x1   x2   x3
```

(Code IV.2 continued)

```
endsymmetry
# Grid definition for density maps
#--------------------------------
dimension  3
voxel   AUTO
# control parameters for Superflip run
#----------------------------
maxcycles   200
repeatmode  1
bestdensities  1


outputfile PCN306_295K_He_57.xplor
expandedlog yes
# Keywords for charge flipping
#----------------------------
perform fourier
delta  AUTO
weakratio  0.0
Biso  0.0
randomseed AUTO
searchsymmetry average
```

(Code IV.2 continued)

```
# input data
#-----------
dataformat intensity phase
fbegin
#   h    k    l      F^2obs       phase
    1    1    0     9323.00        0.5
    0    2    0   100000.00        0.5
    1    1    1     1464.00        0.0
    0    2    1    62648.00        0.5
    2    0    0    18262.00        0.5
    2    2    0    26954.00        0.0
    0    0    2    42729.00        0.0
    1    3    1    22769.00        0.0
    2    2    1     7499.00        0.5
    2    0    2    67432.00        0.5
    2    4    0    83770.00        0.5
    1    5    0    24121.00        0.0
Endf
```

Code IV. 3 Useful commands about subtraction of two density maps in *Chimera UCSF*

```
vop cover #1 fbox 0,0,0,1.01,1.01,1.01
vop cover #2 fbox 0,0,0,1.01,1.01,1.01
vop subtract #2 #1 ScaleFactors 1,k
```

where k is the scaling factor defined as quotient of maximum values of ρ_{obs} and ρ_{ref}.

4.3.7 Contour Plots, Sigma Levels, and Validity Tests

To track down the gas adsorption sites by mapping the evolution of the electron density, a consistent cut-off point for contouring different density maps with varied measuring conditions was required. There is a statistical description for the ρ(x,y,z) distribution to solve this problem: the mean and the standard deviation (σ) of ρ(x,y,z) across the entire mapping space. The relative density of every grid point presented in ρ(x,y,z) can be represented in sigma units away from the mean.[106] An appropriate contour level was anticipated to find the absent matter or missing fragments from the reference model. In this case, the fragments represent CH_4 or CO_2 molecules. For the system of HKUST-1 and PCN-306/ PCN-307, the cut-off level of DED maps (ρ_{gst}) was contoured around 1.5 σ above zero; For PCN-12, it was 1.7 σ.

Note that the termination errors usually occur on a center of inversion, presenting spurious peaks in the pore environments. The DED maps should be carefully examined to see if strong peaks shown in pores come from the termination errors. The benchmarking procedure not only provides a way to evaluate the validity of the DED maps but eliminate the spurious peaks in the pores as well.[87]

To perform the benchmarking procedure, one of the light atoms in the frameworks, such as C, N, or O, was selected as the benchmark atom and removed from the calculated structural model of the investigated crystal. This incomplete model was used to generate ρ_{ref}, and the resulting DED maps (ρ_{gst}) consisted of the benchmark peaks and the guest peaks.

4.3.8 Error Sources and Potential Problems

DED mapping might be meaningless without considering two major error sources.[87] One is the Fourier truncation error caused by the limited number of the selected reflections. This error can be decreased by using a greater number of reflections. However, selecting those reflections within the threshold angle is sufficient to construct a well-fitting envelope with an acceptable error.

Another source of error is the structural transformations caused by the temperature /pressure /atmosphere changes during the measurements. In this work, the empty MOFs (in He atmosphere) at various temperatures were adopted to be the reference envelope (ρ_{ref}), which is helpful to minimize this second error.

It is known that DED maps are affected by errors coming from the number of the reflections (hkl) used in Eq.[4.1]. The more reflections are used in the DED calculation, the more similarity is achieved to the regular difference Fourier electron density map. In other words, this error can be regarded as the difference between the regular difference Fourier electron density map and the DED map. If the difference is small enough, we will say the number of reflections is sufficient to construct the best-fitting surface of the envelope. Therefore, the problem is: Is the envelope good enough by using reflections just going beyond the threshold angle?

Taking HKUST-1 as an example, we can obtained the closed volume of the envelope constructed with 5~11 reflections, respectively (Table IV. 5). The peak #8 is the threshold angle (7.80°) for 5.4-Å resolution, the resulting envelope forming a closed volume of 5989 $Å^3$. By adding one more reflection in the Fourier summation, the

corresponding closed volume changed with -12.86%. After adding 3 more reflections, the percentage of volume change is +1.86%, which can be considered convergence in the Fourier summation. If the DED map (ρ_{gst}) constructed with 8 reflections (the threshold) is satisfying with an acceptable error, it will show a very small difference compared with the DED map constructed with 11 reflections.

Table IV. 5 The reflection number used in Fourier summation (Eq.[4.1]) and the corresponding closed volume of the envelope. The reflections were labelled as follows: #1(1 1 1), #2(0 0 2), #3(2 0 2), #4(1 1 3), #5(2 2 2), #6(0 0 4), #7(3 1 3), #8(2 2 4), #9(4 0 4), #10(2 0 6), #11(4 4 4).

Peak #	5(5.5°)	6(6.4°)	7(6.9)	**8(7.8°)**	9(9.0°)	10(10.1°)	**11(13.0°)**
Volume	6713	6115	6665	**5989**	5219	5541	**5644**
Volume change	-8.91%	+8.99%	-10.14%	-12.86%	+6.17%	+1.86%	

Setting the cut-off level at 1.5 σ above zero, the closed volumes of distribution in the DED map are 741 $Å^3$ for the one using 8 peaks and 705 $Å^3$ for the one using 11 peaks. As shown in Figure IV. 14 a/b (contoured at 1.5σ), the distribution using 11 reflections presents additional tiny fragments around the window openings, as definitely originated from the peak #9, #10, and #11. However, the volume difference is only 5.1%, and the strongest signals are identically located at the center of the small cages based on the 2.5-σ contours (Figure IV. 14 c/d). Hence, we can state that the envelope using 8 reflections in HKUST-1 is acceptable with a volume error of 5.1%. Also, we can see that the distribution outline does not change with different numbers of reflections; more reflections just depict the details. The same contours can be applied for samples measured at 200K (Figure IV. 15) and 150K (Figure IV. 16).

For PCN-306/ PCN-307, there are no significant non-overlapping reflections beyond the threshold angle. Therefore we cannot estimate the exact error with the above steps. On the other hand, in previous work using the envelope method,[87, 91-92] the researchers have usually selected about 5~6 reflections for the cubic system and 7 reflections for the orthorhombic system. Since this study is only focused on the distribution outline of gas molecules, using 8 reflections in the cubic system and 12 reflections in the orthorhombic system should be sufficient with relatively low error.

(a) DED map with 8 reflections at 1.5σ	(b) DED map with 11 reflections at 1.5σ
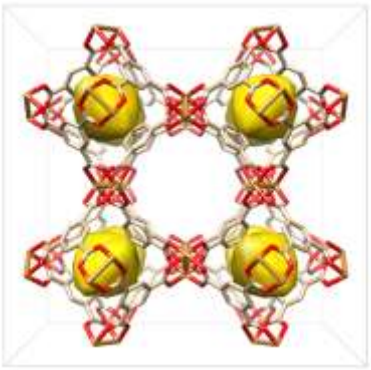	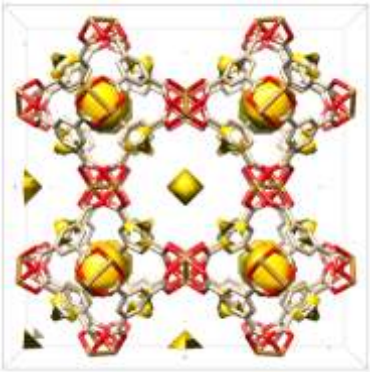
(c) DED map with 8 reflections at 2.5σ	**(d) DED map with 11 reflections at 2.5σ**
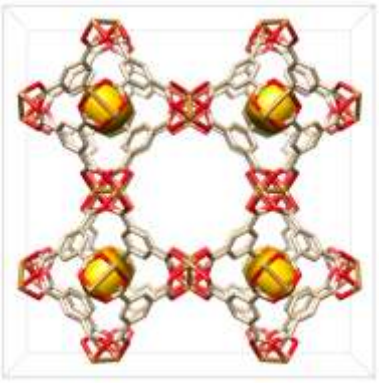	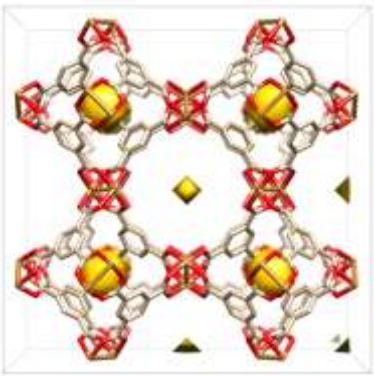

Figure IV. 14 The DED maps using 8 or 11 reflections at 295K.

(a) DED map with 8 reflections at 1.5σ	(b) DED map, 11 reflections at 1.5σ
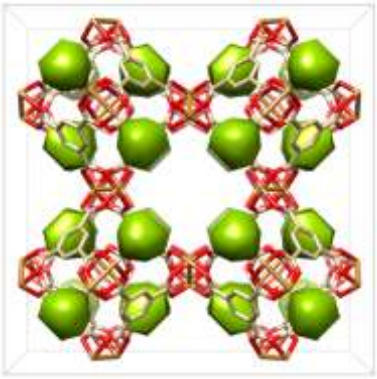	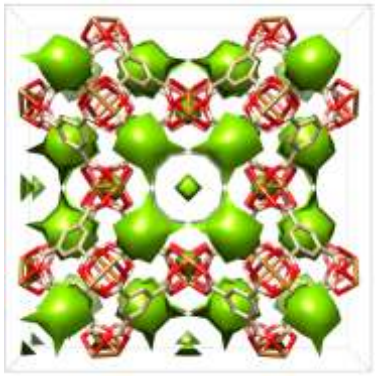

Figure IV. 15 The DED maps using 8 or 11 reflections at 200K.

(a) DED map with 8 reflections at 1.5σ	(b) DED map, 11 reflections at 1.5σ
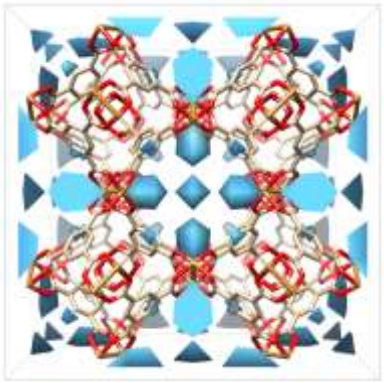	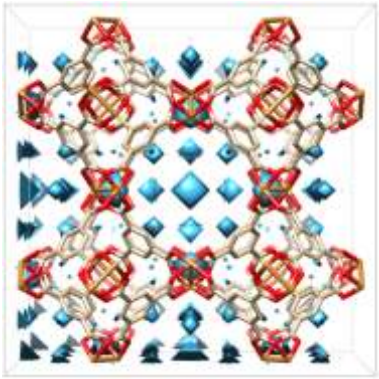

Figure IV. 16 The DED maps using 8 or 11 reflections at 150K.

4.3.9 Potential Problem: Inhomogeneous Sampling and Thermal Gradient

Inhomogeneous sampling might cause a potential problem in the experiment processes. Even if care is taken to use slow loading, it is likely that the gas molecules are not spread homogeneously over the whole powder sample. In our experimental setup, a 0.3 mm round X-ray beam through the center of a capillary with 0.8 mm inner diameter covers over 45% of the cross section area (Figure IV. 17). The measurement averages the diffraction from thousands of microcrystallites, which is evidence that the gas redistribution events happen consistently in the bulk material.

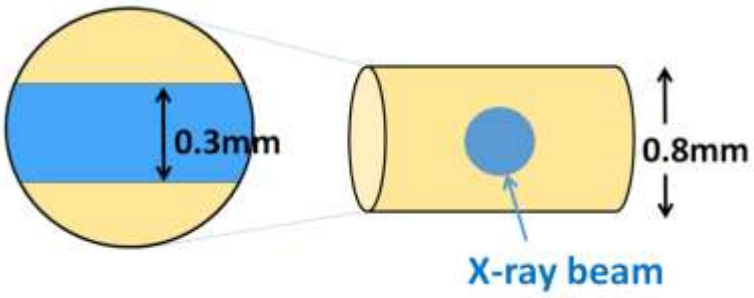

Figure IV. 17 The relative dimension between the beam size and the inner diameter of the capillary.

Apart from the problem with sample inhomogeneity, many states of order/disorder and transport in the material might be sampled simultaneously, resulting in peak width broadening. The F^2(h k l) difference integrated from the profile function, instead of the intensity maximum difference, can take the peak width change into account in the calculation. In this work, we can see that the peak widths in the *in situ* PXRD patterns (Figure IV. 5, Figure IV. 6, Figure IV. 7) barely change after gas loading at room temperature, suggesting the state change is trivial. Although the peak width changes at low temperatures, using the maximum difference is sufficient to obtain gas distribution profiles because it usually happens at the low intensity reflections.

Upon temperature changes, thermal gradients might cause the parts of the sample sampled by the beam to not be homogeneous. As shown in Figure IV. 18, the DED maps measured for HKUST-1 did not show an obvious difference after the loading time of 50 seconds at 200K/ 150K. For PCN30X, it also did not change a lot after 400 seconds at 200K/ 150K. Therefore, we can claim that the thermal gradients are not an issue in the study. The algorithm for the TRDSE method was schemed in Figure IV. 19.

(a) DED measured at 200K, 50sec	(b) DED measured at 200K, 1500sec
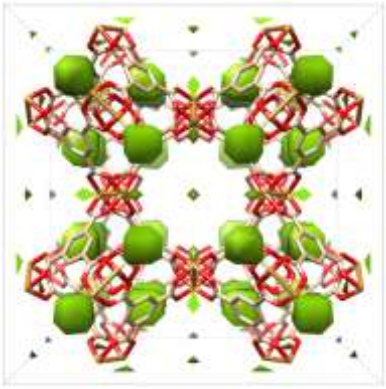	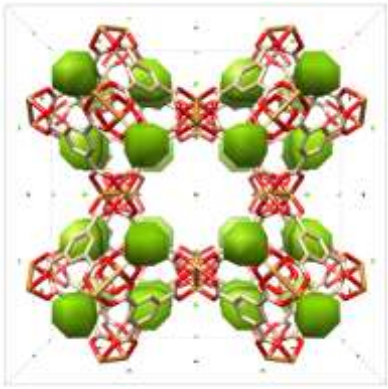
(c) DED measured at 150K, 50sec	**(d) DED measured at 150K, 1500sec**
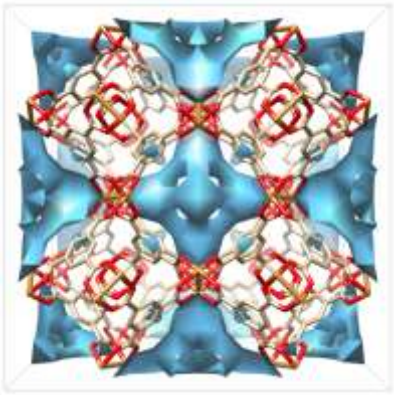	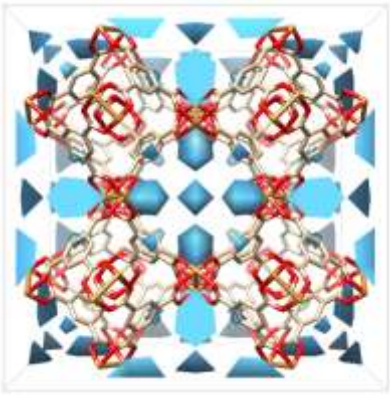

Figure IV. 18 The DED maps measured at 200K/150K, confirming the thermal equilibrium was achieved in a very short period.

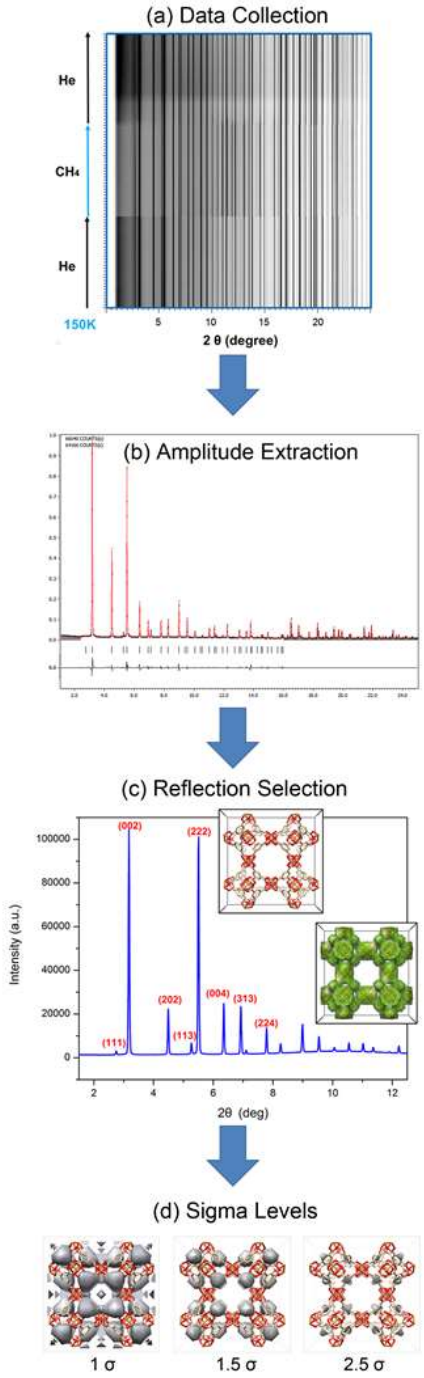

Figure IV. 19 The algorithm for the TRDSE method: (a) Top view of the *In situ* synchrotron-based powder diffraction; (b) Le Bail refinement to extract the intensity amplitudes; (c) Structure envelope generation using selected reflections; (d) Different sigma levels to describe the DED maps.

4.4 Results and Discussion

4.4.1 Experimental DED Mapping Results and Simulations

Monte Carlo simulations were employed to calculate the adsorption sites of CH_4 in the selected MOFs at RT/200K/150K using *Materials Studio* package.[107] The structures of MOFs were constructed from their corresponding experimental single-crystal diffraction data, and were treated as rigid frameworks with atoms frozen at their crystallographic positions. Universal force field[108-111] was used to describe the adsorbed molecules and MOFs. An atom-based method was applied to determine non-bond energies. For each state point, MC simulations consisted of 2×10^7 steps to ensure the equilibration, followed by another 2×10^7 steps to sample the desired properties. A detailed description of the simulation method can be found elsewhere.[112]

Past research has shown that gas molecules are located at up to eight distinct sites in MOF-5 and HKUST-1.[66-67, 84] For CH_4 storage in HKUST-1, the open Cu(II) sites and the window openings were proposed to be the primary adsorption sites while the center of the small octahedral cages and the corner of large cuboctahedral cages were the secondary adsorption sites.[73] In our DED maps (Figure IV. 20, right column), strong electron density is located in the small octahedral cages at 295K, at the window openings at 200K, and around the large cage corners at 150K, respectively. This is also found in the ensemble-averaged maps predicted by the Monte Carlo simulation in *Materials Studio*[107] (Figure IV. 20, left column).

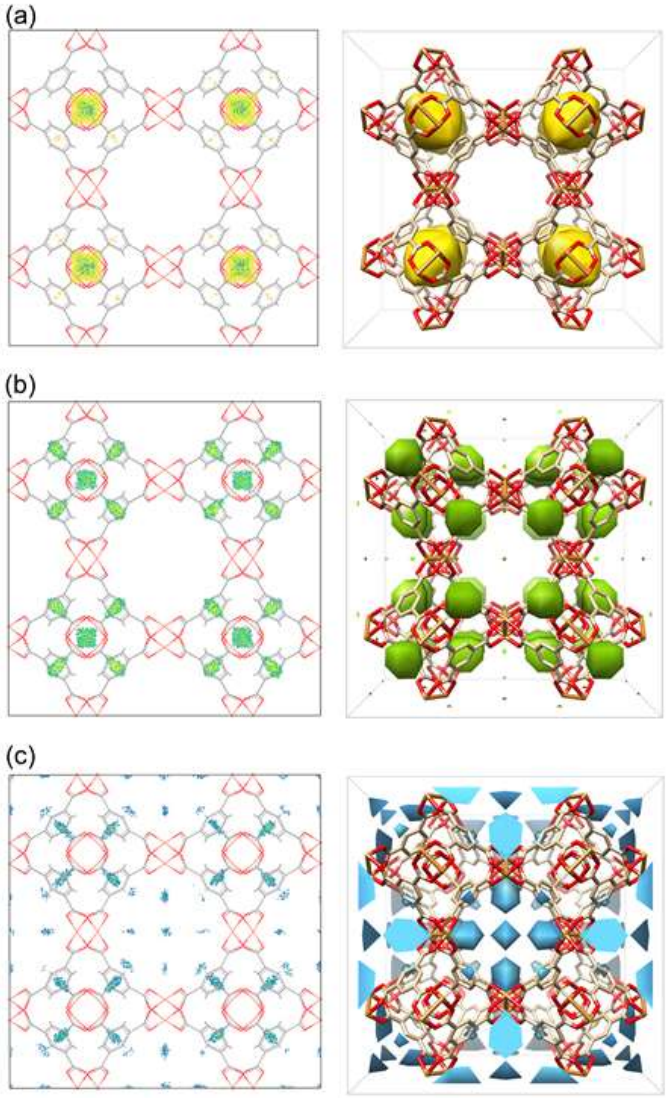

Figure IV. 20 Agreement between the computational (left) and experimental (right) results of CH_4 adsorption at (a) 295K, (b) 200K, (c) 150K in HKUST-1.

These consistent outcomes were also recognized in the noble gas system, where the gas molecules could be considered CH_4-like particles.[80] Both the published literature and our simulations confirm the validity of the TRDSE method. It is worth mentioning that the open metal sites show adsorption of CO_2 molecules at room temperature. In the following sections, four gas kinetic processes are graphically demonstrated. Infusion and desorption as well as temperature evolution and gas rearrangement are elucidated by the chronological DED maps, and possible enthalpic and entropic rationalizations are discussed. Finally, a comprehensive examination describes the minute differences between a pair of analogues, PCN-306 and PCN-307. All the maps in this chapter were made yellow for the samples measured at 295K, green for 200K, and blue for 150K.

4.4.2 Initial Adsorption in MOFs

Gas infusion into MOFs is the most common process in all gas-related applications. However, the gas kinetics in the initial CH_4 adsorption are still unclear. To capture the instantaneous changes at the early stage, the gas flow rate should be as slow as possible. Herein, the CH_4 flow rate was regulated as approximately 0.4mm^3/sec. The studied objects, PCN-30X and PCN-12, have 3-fold window openings (Figure IV. 26c), which will be the focus in this section.

Interpreted from the differences between the reference and the CH_4-loaded crystals, a molecular transport path was observed between the coordinately unsaturated metal units and the window sites. In Figure IV. 24 measured at 295K, the CH_4 molecules approached the open Cu sites along the *c*-axis at the very beginning (Figure IV. 24a), followed with the increasing CH_4 population at the open Cu sites and in the window

pockets (Figure IV. 24b). Successively, the major portion of CH_4 molecules migrated[113] from the open Cu sites to the window pockets (Figure IV. 24c), completing a "kinetic transition". This indicates that the open metal sites perform as kinetic first attractors that direct CH_4 molecules to thermodynamically stable adopters.[114] Also, the first docked molecule is a directing agent of subsequent molecules, as it facilitates the sorption to spread throughout the whole structure starting from the open metal sites.[115]

This phenomenon of kinetic transition did not occur only at room temperature; it also happened near the condensation temperature of CH_4 (Figure IV. 21). At 150K, a small amount of CH_4 molecules were attracted to the open Cu sites at the onset. In seconds, the incoming CH_4 molecules navigated to the adjacent cages (Figure IV. 4c) rather than moving into the window pockets, reaching another thermodynamically favored site. With continuous CH_4 addition, the large pores were gradually filled along the *a*-axis of the crystal (Figure IV. 22). The temperature effect on the final states of gas migration will be discussed in section 4.4.4 describing gas redistribution with temperature change. Although the CH_4 destinations at the two temperatures (295/150K) were different, both of the surface/volume ratios of the observed CH_4 electron clouds decreased with loading time (Table IV. 6). This displays a visible tendency of surface minimization upon CH_4 infusion. The parallel results of PCN-307 can be found in Figure IV. 23. To the best of our knowledge, this is the first example of experimental evidence of the kinetic transition of gas molecules in MOFs.

(a) X-ray shot taken after CH_4 loading for 150 sec

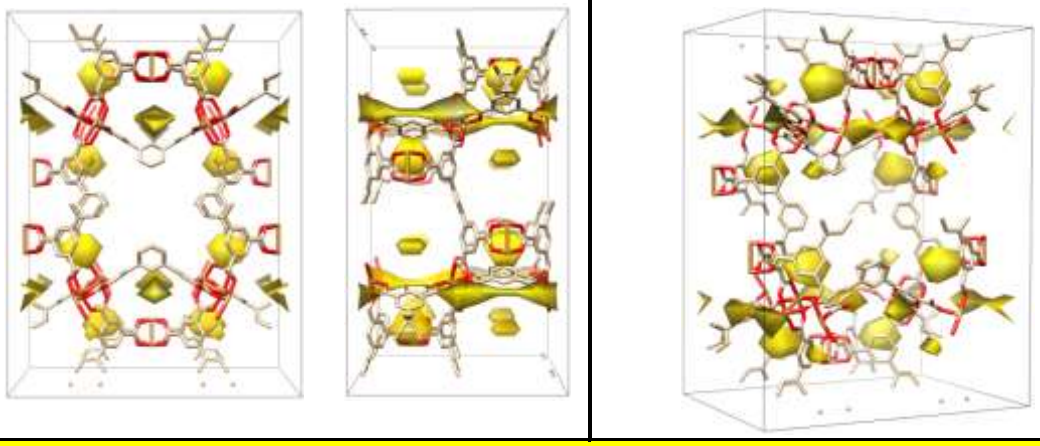

(b) X-ray shot taken after CH_4 loading for 330 sec

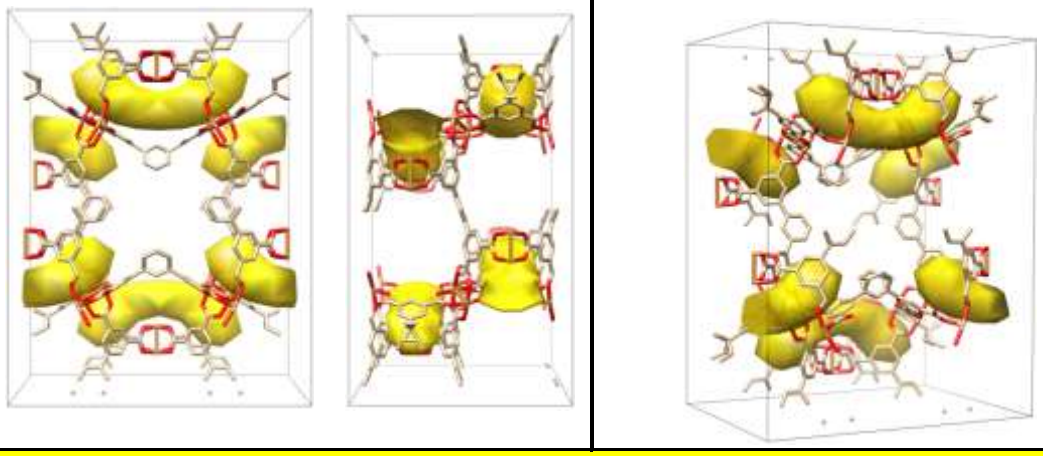

(c) X-ray shot taken after CH_4 loading for 510 sec

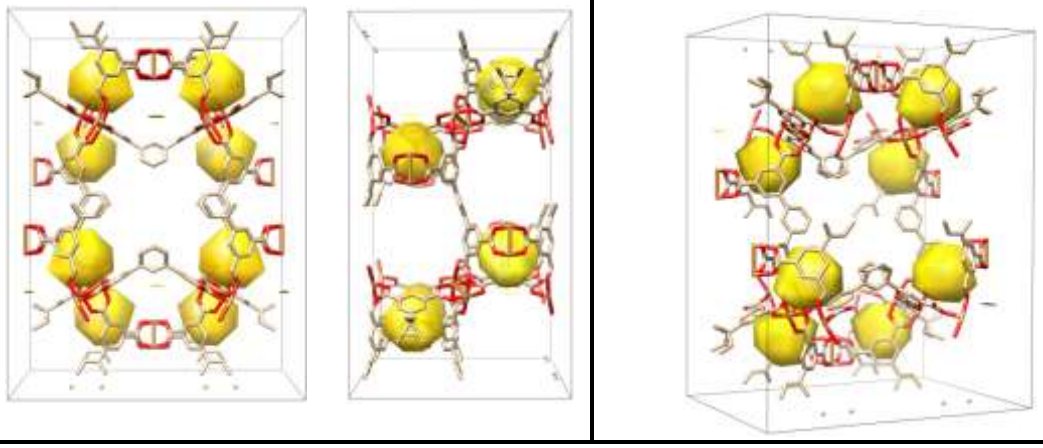

Figure IV. 21 Time-dependent CH_4 migration in PCN-306 at 295K and 1 bar.

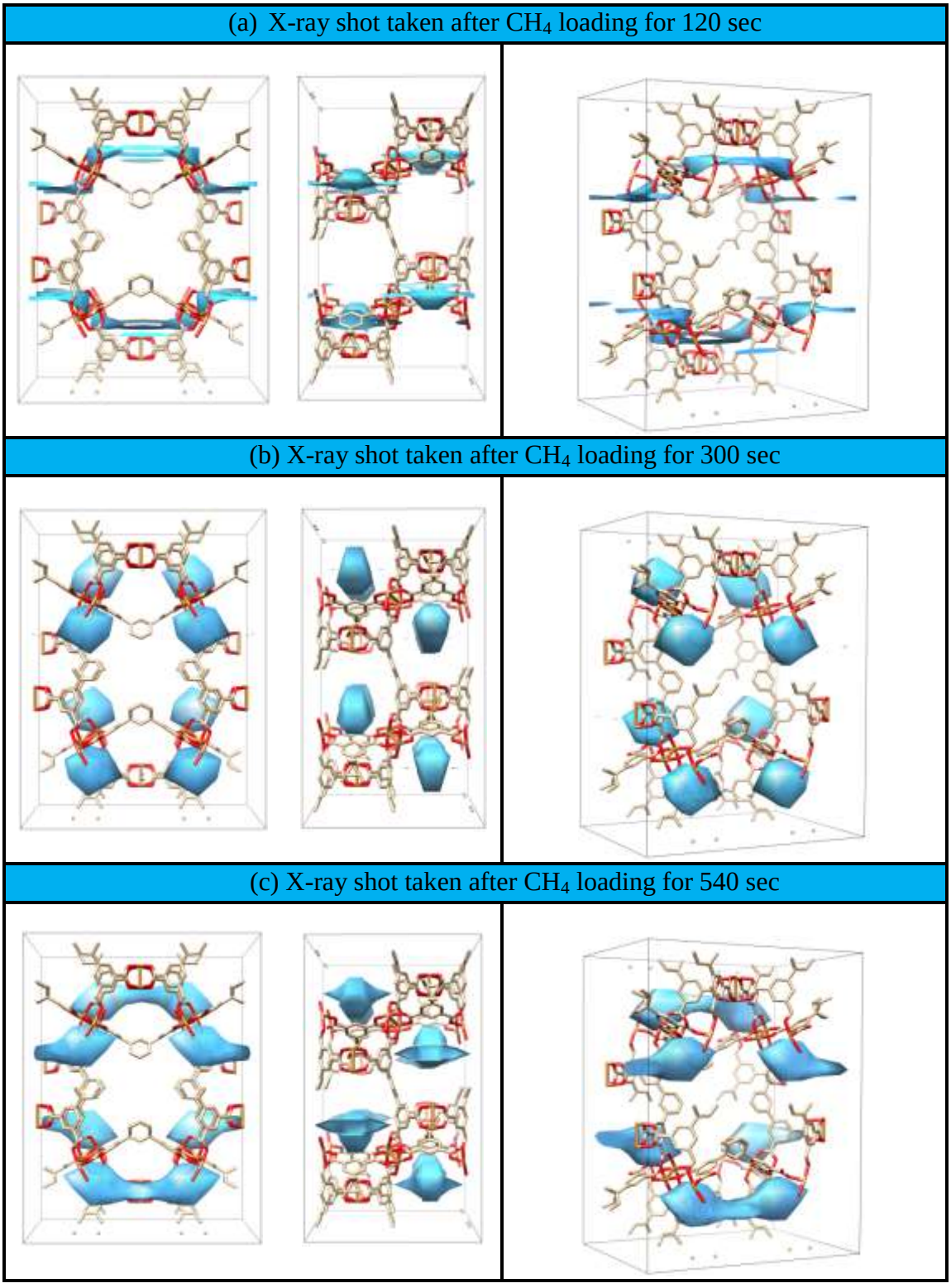

Figure IV. 22 Time-dependent CH_4 migration in PCN-306 at 150K and 1 bar.

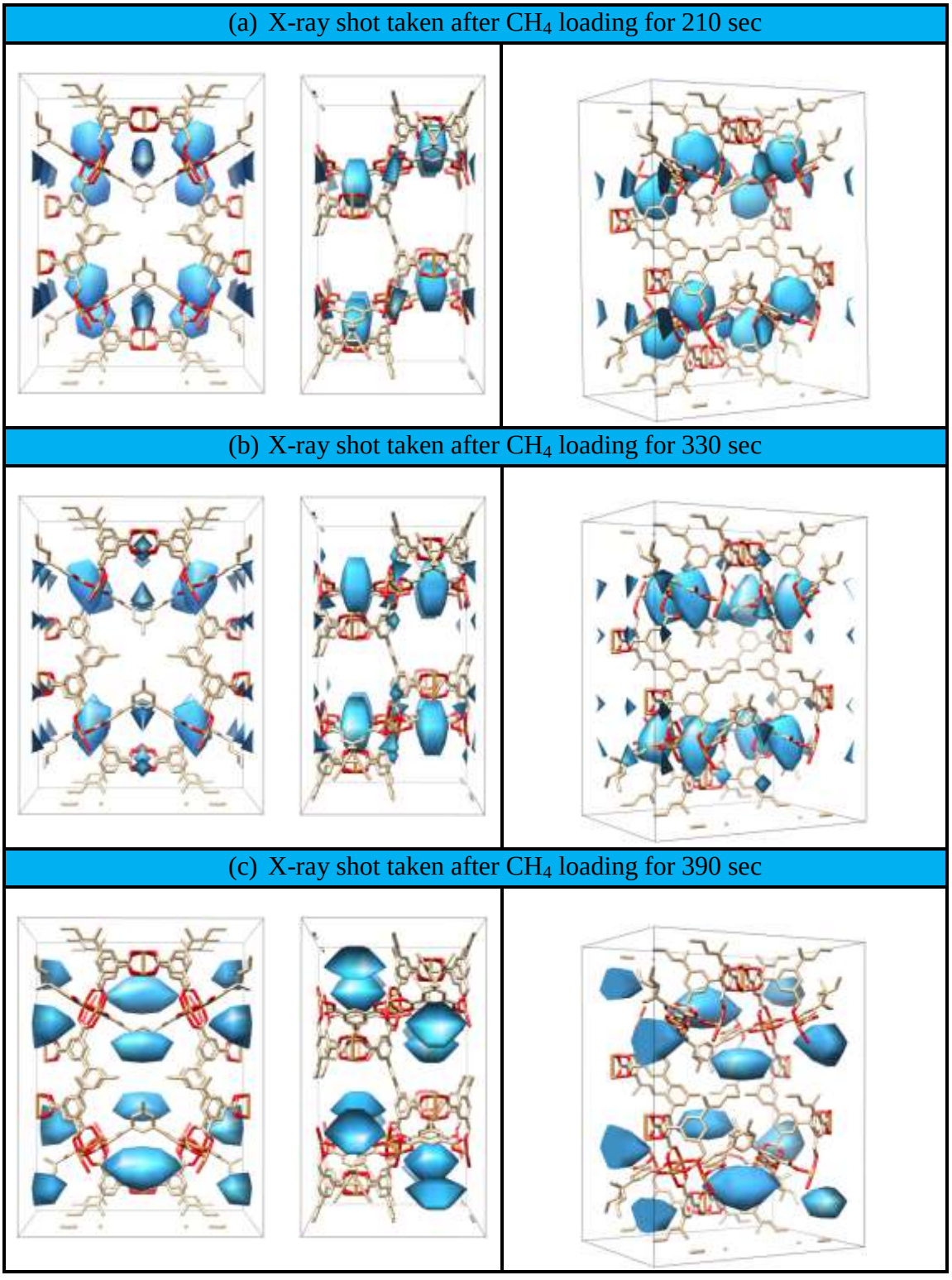

Figure IV. 23 Time-dependent CH_4 migration in PCN-307 at 150K and 1 bar

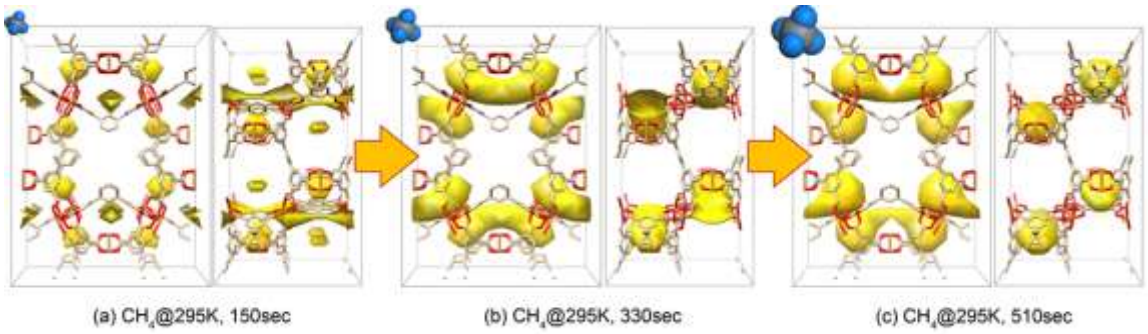

Figure IV. 24 The DED snapshots illustrate the kinetic transition in the CH_4 adsorption process in PCN-306. The perspectives are viewed along the *c*-axis (left) and *a*-axis (right). The CH_4 flow was introduced into the crystals, followed by sequential X-ray measurements after (a) 150 seconds; (b) 330 seconds; (c) 510 seconds, under controlled conditions of 295K and 1 bar. Yellow clouds represent the most significant adsorption regions with contouring at 1.5σ.

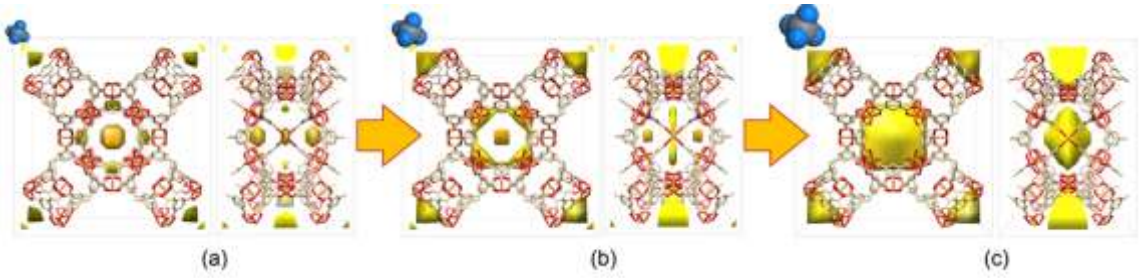

Figure IV. 25 The DED snapshots illustrate the kinetic transition of the CH_4 adsorption process in PCN-12. These are viewed along *c*-axis (left) and *a/b*-axis (right). The CH_4 flow was introduced into the crystals, followed by sequential X-ray measurements after (a) 30 seconds; (b) 150 seconds; (c) 630 seconds, at 295K and 1 bar.

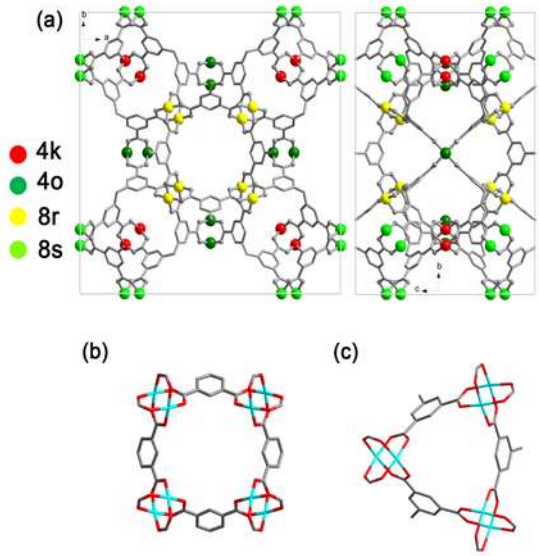

Figure IV. 26 (a) Wyckoff positions labeled for Cu_2 units in PCN-12, viewed along *c*-axis (left) and *a/b*-axis (right).
PCN-12 comprises (b) four-fold window openings (four pairs of Cu_2 units and phenyl rings), and (c) three-fold window openings.

Table IV. 6 The summary of the time-dependent PXRD experiments performed on PCN-306 and PCN-12, including the measurement conditions, the gas loading times, the absolute values of the contour levels, the total volumes and surfaces of the electron clouds regions shown in Figure IV. 24 and Figure IV. 25, and the relative ratios of electron quantity. The contour level is 1.5 σ for PCN-306 and 1.7 σ for PCN-12.

Compound	Condition	Time (sec)	Contour Level	Volume ($Å^3$)	Surface ($Å^2$)	Sur./Vol	Electron Ratio
PCN-306	295K 1bar	150	0.00146	380.9	1005	2.6	0.56
		330	0.00372	1154	1219	1.1	4.29
		510	0.00390	817.6	920.7	1.1	3.18
	150K 1bar	120	0.000735	196.7	777.2	4.0	0.14
		300	0.0110	571.2	754.8	1.3	6.28
		540	0.0158	753.2	1075	1.4	11.9
PCN-12	295K 1bar	30	0.00173	361.8	768.3	2.1	0.63
		150	0.00206	362.3	677.3	1.9	0.75
		630	0.00282	1221	1071	0.9	3.44

In order to deeply study the kinetic transition from *open Cu sites* to other structural spaces, further analysis was done on PCN-12. In addition to the 3-fold window sites (Figure IV. 26c), PCN-12 is also constructed by larger 4-fold openings (Figure IV. 26b), and there are various sizes of cages in the structure. As shown in Figure IV. 26a, PCN-12 comprises four Wyckoff positions of Cu_2 units. As viewed along the *c*-axis, the Cu_2 units labeled with 8s/4k as well as those with 8r/4o build identical symmetrical cages 11 Å wide. The 8s/4o units form large ellipsoidal cages 17Å long, and the 8r/4k units form small cavities 9Å wide. The cages constructed by different sets of open metal sites were not equivalently accessible for CH_4 molecules. The cages consisting of 8r/4o sets and 8s/4k sets were populated with CH_4 whereas those with the 8s/4o and 8r/4k sets were left vacant. This nonequivalence of CH_4 amounts on these open metal sites indicates that gas molecules discriminate among the binding sites in favor of those with nearby multipoint interactions[70] and appropriate spatial accessibility.

Another kinetic transition occurred on this adsorbent. In Figure IV. 25a, the CH_4 molecules were trapped by the open Cu sites 4o and the 4-fold window openings, both of which are the most easily accessible regions on the central channels. In Figure IV. 25b, the transition direction changed from the open Cu sites (Wyckoff 4o) to the larger 4-fold window openings but not the smaller 3-fold sites. The DED contours showed a close ring connecting the area between the open Cu sites and their bordering 4-fold window openings. Further CH_4 loading did not diffuse homogenously into the small volume, which contains the available open Cu sites classified as 4k. Instead, CH_4 molecules

aggregated in the center of the channels to reach the surface minimum (Figure IV. 25c and Table IV. 6).

Consequently, this time-dependent kinetic transition can be recognized at various temperatures and in different adsorbents. Especially for Figure IV. 24b-c,[116] the transition continues at the near equilibrium state. We attribute this unusual behavior, molecular transport from one binding site to another, to an inevitable consequence of thermodynamics. Based on the basic thermodynamic relationship,

$$\Delta G = \Delta H - T\Delta S \qquad [4.3]$$

the transition process will be spontaneous ($\Delta G < 0$) if one of the following conditions are true: (a) $\Delta H < 0$, $\Delta S > 0$, (b) $\Delta H < 0$, $\Delta S < 0$, plus $|T\Delta S| < |\Delta H|$ or (c) $\Delta H > 0$, $\Delta S > 0$, plus $|T\Delta S| > |\Delta H|$

where $\Delta H < 0$ is defined as exothermic heat, and $\Delta S < 0$ refers to the transition to fewer molecular degrees of freedom in the process. According to Wu *et al.*'s report,[73] the CH_4 binding energy of open metal sites is around 25 kJ/mol., roughly identical to that of window sites.[117] This means that $|\Delta H|$ is extremely small. We attribute this discovery to (c); that is, the gas molecules will be able to break away from the potential well if $T\Delta S \geq \Delta H \approx 0$. More precisely, we made an effort to investigate how this entropic driving force pushes gas molecules out of the potential well in the equilibrium states. A localized-to-mobile model,[118-120] considering the adsorbates partially localized and partially mobile, was hypothesized to fit our observations.

In this model simplified with statistical treatment[118] , f is introduced to define the maximum fraction of the adsorbent surfaces on which adsorbates can be localized. θ_l and θ_m are the fractions of truly adsorbed molecules on the localized and mobile areas, respectively. N_{sl}, N_l and $N_m$are the molecular numbers corresponding to f, θ_l and θ_m. The relationship between the above parameters can be expressed as

$$f = N_{sl}/N_s, \quad \theta_m = N_m/N_s, \quad \theta_l = N_l/N_s, \quad \theta = \theta_l + \theta_m$$

where N_s is the maximum number of the molecules that can be adsorbed on all solid surfaces. The partition functions for a localized molecule(q_l) and for a mobile molecule (q_m) are $q_l = q_{vx}q_{vy}q_{vz}\exp\left(-\frac{u_{pl}}{kT}\right)$ [4.4]

$$q_m = \left(\frac{2\pi mkT}{h^2}\right) q_{vz}a_s \exp\left(-\frac{u_{pm}}{kT}\right)[N_s(1-f) - N_m] \quad [4.5]$$

where u_{pm} and u_{pl} are the corresponding potential energy in adsorbed states. q_{vx}, q_{vy}, q_{vz} are the vibrational partition functions in x, y, z directions. $\frac{2\pi mkT}{h^2}$ is the translational partition function. q'_m is the partition function for mobile molecules without size correction, which is given as $q'_m = \left(\frac{2\pi mkT}{h^2}\right) q_{vz}a_s \exp\left(-\frac{u_{pm}}{kT}\right)$.

The molecular distribution over mobile and localized regions can be derived as:[118]

$$\exp\left(\frac{\theta_m}{1-f-\theta_m}\right) = \frac{\theta_l}{(f-\theta_l)q_l} \quad [4.6]$$

In order to present Eq.[4.6] in a figure, the relative value of q'_m and q_l and possible f have to be estimated from Eq.[4.4] and [4.5]. A CH_4 molecule has a mass (m) of 2.66 x10^{-26} kg and a cross-sectional area[121] (a_s) of 0.164nm^2. For simplicity, all vibrational partition functions were assumed to be unity and u_{pm}=u_{pl}. Substituting into

Eq. [4.4] and [4.5], $q'_m/q_l = 254$ was obtained. The distributive ratios of the localized CH_4 (θ_l/θ) were graphically depicted with an assumption of q'_m/q_l =10, 30, 100, 254 in Figure IV. 27a, and f =0.3, 0.5, 0.7, 0.9 in Figure IV. 27b, respectively. All the curves possess a maximum before full coverage ($\theta = 1.0$).

We selected q'_m/q_l = 30 and f = 0.5 as representative (blue trace in Figure IV. 27c). It is expected that θ_l/θ approaches f with a positive slope; nevertheless, an interesting range showing $\theta_l/\theta > f$ occurs at near 85% of the coverage($\theta \approx 0.85$), and thus a negative slope is necessary to complete full coverage. One of the possibilities for the negative slope of $\frac{\Delta\theta_l/\theta}{\Delta\theta}$is molecular transport from a localized area to a mobile area. If the open metal sites and the nearby window pockets are regarded as a localized part and a mobile part for adsorbates respectively, the localized-to-mobile model will match our experimental observations of kinetic transition in PCN-30X and PCN-12. However, if both the open metal sites and the window sites are localized parts, the exponential term in Eq.[4.6] will be absent, resulting in a monotonic increasing function without any negative slopes in Figure IV. 27c (red trace). That also means no molecular transport will happen under the localized-to-localized assumption.

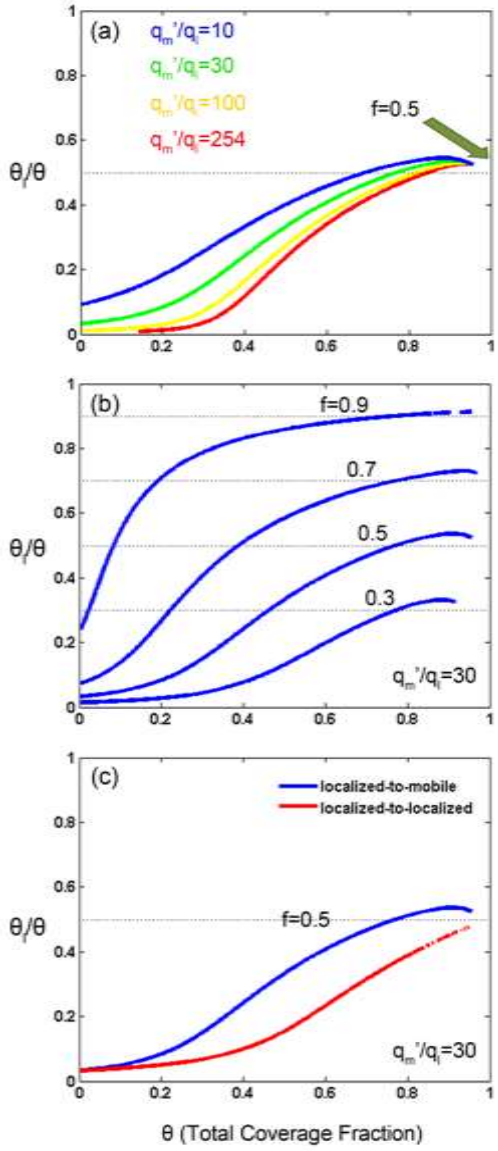

Figure IV. 27 The molecular distribution over localized regions on heterogeneous surfaces (the graphical presentation of Eq.[4.6]): The fraction of the localized adsorbates on the adsorbent surface if (a) the ratio of $\frac{q'_m}{q_l}$ varies; (b) the maximum fraction of localized adsorbates, f, varies. (c) Theoretical derivation for localized-to-mobile case and localized-to-localized case.

In summary, the sequential measurements of *in situ* powder X-ray diffraction give insight into gas kinetic transitions occurring between open metal sites and the neighboring structural spaces. In spite of the fact that the open metal sites possess potential wells and significant exothermic enthalpy, there is another possibility to reach minimum Gibbs energy for the adsorption process by increasing entropy. In this section, we experimentally visualized the abstract concept of this entropy-driven process. The localized-to-mobile mechanism was proposed for the cause of gas kinetic transition, supporting the observations of molecular transport from one site to another.

The basic statistical equations were derived as follows. From the modified statistical treatment for partially localized and partially mobile adsorbates, f is introduced to define the maximum fraction of the adsorbent surfaces on which adsorbates can be localized. θ_l and θ_m are the fractions of truly adsorbed molecules on the localized and mobile areas, respectively. N_{sl}, N_l and $N_m$are the molecular numbers corresponding to f, θ_l and θ_m. The relationship between the above parameters can be expressed as

$$f = N_{sl}/N_s, \quad \theta_m = N_m/N_s, \quad \theta_l = N_l/N_s, \quad \theta_l + \theta_m = \theta$$

where N_s is the maximum number of the molecules that can be adsorbed on the whole solid surfaces. The partition functions for a localized molecule(q_l) and for a mobile molecule (q_m) are

$$q_l = q_{vx} q_{vy} q_{vz} \exp\left(-\frac{u_{pl}}{kT}\right)$$

$$q_m = \left(\frac{2\pi mkT}{h^2}\right) q_{vz} a_s \exp\left(-\frac{u_{pm}}{kT}\right) [N_s(1-f) - N_m] \;=\; q'_m [N_s(1-f) - N_m]$$

where u_{pm} and u_{pl} are the corresponding potential energy in adsorbed states. q_{vx}, q_{vy}, q_{vz} are the vibrational partition functions in x, y, z directions. $\frac{2\pi mkT}{h^2}$ is the translational partition function. q'_m is the partition function for mobile molecules without size correction, which is given as $q'_m = \left(\frac{2\pi mkT}{h^2}\right) q_{vz} a_s \exp\left(-\frac{u_{pm}}{kT}\right)$.

The canonical partition function of the entire localized adsorbate (Q_l) and the entire mobile adsorbate (Q_m) are

$$Q_l = \frac{N_{sl}!\, q_l^{N_l}}{(N_s - N_l)!\, N_l!}$$

$$Q_m = \frac{q_m^{N_m}}{N_m!}$$

If the adsorption reaches the equilibrium, the chemical potentials $\mu_l = -kT \frac{\partial \ln Q_l}{\partial N_l}$ and $\mu_m = -kT \frac{\partial \ln Q_m}{\partial N_m}$ of the two adsorbate types will be equalized. Note Stirling's approximation, $\ln N! = N \ln N - N$.

$$\frac{\partial \ln Q_m}{\partial N_m} = \frac{\partial}{\partial N_m}\left[ln \frac{q_m^{N_m}}{N_m!}\right]$$

$$\frac{\partial \ln Q_l}{\partial N_l} = \frac{\partial}{\partial N_l}\left[\ln \frac{N_{sl}!\, q_l^{N_l}}{(N_{sl} - N_l)!\, N_l!}\right]$$

The molecular distribution over mobile and localized regions can be derived as follows:

$$\frac{\partial \ln Q_l}{\partial N_l} = \frac{\partial}{\partial N_l}\left[\ln \frac{N_{sl}!\, q_l^{N_l}}{(N_{sl} - N_l)!\, N_l!}\right]$$

$$= \frac{\partial}{\partial N_l}[\ln N_{sl}! + N_l \ln q_l - \ln(N_{sl} - N_l)\,! - \ln N_l!]$$

$$= \frac{\partial}{\partial N_l}[[N_{sl}\ln N_{sl} - N_{sl}] + N_l \ln q_l - [(N_{sl} - N_l)\ln(N_{sl} - N_l) - (N_{sl} - N_l)] - [N_l \ln N_l - N_l]]$$

$$= \ln q_l + N_l \frac{\partial \ln q_l}{\partial N_l} - (-1)\ln(N_{sl} - N_l) - (N_{sl} - N_l)\frac{(-1)}{N_{sl} - N_l} + (-1) - \ln N_l - N_l \frac{1}{N_l} + 1$$

$$= \ln q_l + \ln(N_{sl} - N_l) - \ln N_l$$

$$\frac{\partial ln Q_m}{\partial N_m} = \frac{\partial}{\partial N_m}\left[\ln \frac{q_m^{N_m}}{N_m!}\right]$$

$$= \frac{\partial}{\partial N_m}[N_m \ln q_m - \ln N_m!]$$

$$= \frac{\partial}{\partial N_m}[N_m \ln q_m - [N_m \ln N_m - N_m]]$$

$$= \ln q_m + N_m \frac{\partial \ln q_m}{\partial N_m} - \ln N_m - N_m \frac{\partial \ln N_m}{\partial N_m} + 1$$

$$= \ln[q_m{}'(N_s(1-f) - N_m)] + N_m \frac{(-1)}{N_s(1-f) - N_m} - \ln N_m - \frac{N_m}{N_m} + 1$$

$$= \ln[q_m{}'(N_s(1-f) - N_m)] + N_m \frac{(-1)}{N_s(1-f) - N_m} - \ln N_m$$

$$\ln q_l + \ln(N_{sl} - N_l) - \ln N_l = \ln[q_m{}'(N_s(1-f) - N_m)] + N_m \frac{(-1)}{N_s(1-f) - N_m} - \ln N_m$$

$$q_l\,(N_{sl} - N_l)\,\left(\frac{1}{N_l}\right) = q'_m(N_s(1-f) - N_m)\,\exp\left[\frac{(-N_m)}{N_s(1-f) - N_m}\right]\left(\frac{1}{N_m}\right)$$

$$q_l\,(f - \theta_l)\,\left(\frac{1}{\theta_l}\right) = q'_m(1 - f - \theta_m)\,\exp\left[\frac{(-\theta_m)}{(1-f) - \theta_m}\right]\left(\frac{1}{\theta_m}\right)$$

$$\frac{\theta_m}{(1 - f - \theta_m)q'_m}\exp\left(\frac{\theta_m}{1 - f - \theta_m}\right) = \frac{\theta_l}{(f - \theta_l)q_l}$$

4.4.3 Desorption in MOFs

Engines running on CH_4 require an exhaust pressure to operate. The usable working capacity and the regeneration efficiency are as important as the gas uptake performance.[117] In other words, the speed and completeness of desorption is another key indicator to evaluate the industrial applicability of a MOF material for methane storage.

As a result, in Figure IV. 28a and c, the CH_4 molecules sit in the small octahedral cages whereas CO_2 molecules primarily[122] lie on the window openings in the adsorption states. As opposed to the distinctive features for CH_4 and CO_2 adsorption, the maps for these two desorption processes become consistent. Both of the gas residues were detected around the open metal sites (Figure IV. 28b, d and Table IV. 7), exhibiting the final desorbed molecules being stuck around the sites possessing strong electrostatic force.

According to our work on initial adsorption, the open metal site is the first attractor. Additionally, the open metal site is also the last area of significant gas molecule presence in desorption. A site possessing higher adsorption enthalpy will be more attractive and populated than a weaker site by simple Boltzmann statistics. Those sites with very high affinity for gas molecules gives rise to substantial uptake but thus contribute negatively to the desorption process. This explains why both HKUST-1 and MOF-74 performed remarkably in CH_4 uptake, but MOF-74 fared poorly in the test of usable working capacity.[123] Hence, introducing excessive unsaturated metal units which are not nodes of windows is not a good choice in practical design of MOFs with optimal methane working capacity.

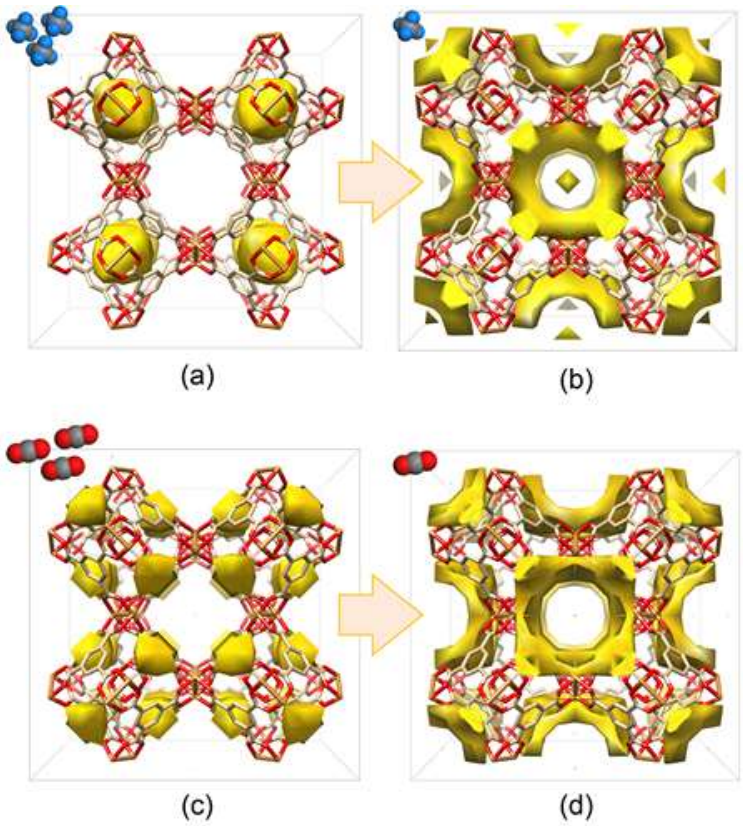

Figure IV. 28 The DED snapshots illustrate the evolution of CH_4/CO_2 desorption in HKUST-1 at 295K. The experiment procedure was controlled as follows: (a) CH_4 loading for 1500 seconds, (b) followed by He flushing for 300 seconds; (c) CO_2 loading for 1500 seconds, (d) followed by He flushing for 300 seconds.

Table IV. 7 The ratios of relative electron quantity detected in the four states corresponding to Figure IV. 28.

Gas	State	Electron Ratio
CH_4	(a)Adsorption	12.2
	(b)Desorption	2.67
CO_2	(c)Adsorption	11.7
	(d)Desorption	3.5

4.4.4 CH_4 Redistribution upon Temperature Change in MOFs

In our computational work (Figure IV. 20, left), the preference of adsorption sites is intensely temperature-dependent. For example, in HKUST-1, the small octahedral cages are positive to adsorption at room temperature, but do not exhibit high adsorption at low temperature (Figure IV. 20). Therefore, it will be valuable to find the characteristic features for optimal adsorption at various environment conditions.

In the powder patterns of PCN-306 (Figure IV. 29), (020), (021) and (202) are the main diffractions coming from the metal clusters. The intensity of the reflections (021) and (202) is decreased dramatically with decreasing temperature. In Figure IV. 30 and Figure IV. 31, the weakening reflections show that additional scattering electrons were collected around the corner sites and the cage sites (Figure IV. 4 c,d), being destructive to the diffraction of metal clusters. The adsorbed CH_4 molecules at the equilibrium states were predominantly mapped in the window pockets at 295K (Figure IV. 30a) and around the large cage along *a*-axis at 150K (Figure IV. 30c). Interestingly, between the two temperatures, the CH_4 density map measured at 200K was partially located at the window openings and partially spread around the cages (Figure IV. 30b). As illustrated in the right-side evolution of Figure IV. 30, the electron density maps shifted from the window pockets to the empty cages stepwise. The state b is regarded as a transitional state between state a and c, redistributed among the surfaces with two types of adsorption sites.

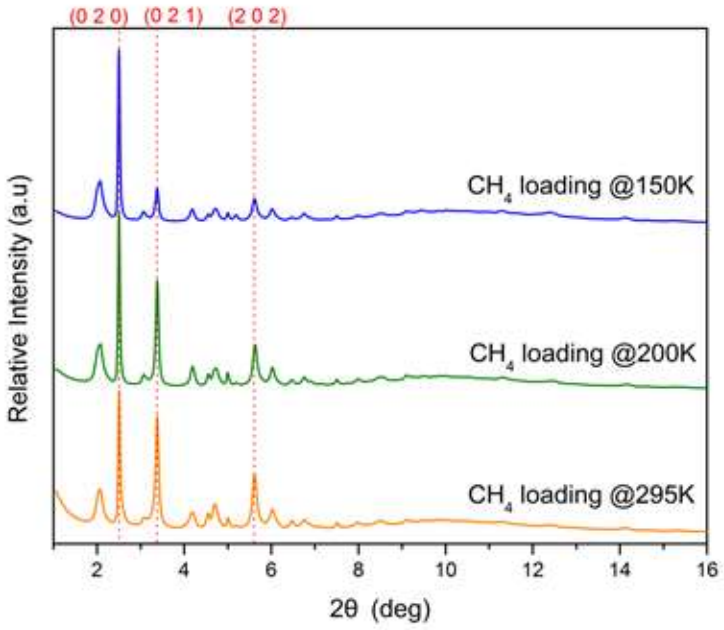

Figure IV. 29 The powder patterns diffracted by CH_4-loaded PCN-306 at various temperatures. (λ=0.72910 Å)

From the neutron studies[77, 83] and high-resolution isotherms[124-125] for MOF materials, it was generally thought that the low energy sites(large pores) do not start to be filled until the high energy sites(small pores) are completely occupied. However, in Figure IV. 30b, CH_4 molecules were observed with a mixed type of adsorption sites, implying that the one-after-one filling order may be incorrect. In the enthalpic view, gas molecules should be trapped at the primary binding sites prior to the secondary sites, releasing as much adsorption heat as possible. In the entropic view, gas molecules should redistribute among several types of sites, reaching as many microstate configurations as

possible. The occupation of mixed adsorption sites is an optimization between enthalpy and entropy to achieve the minimum of free energy.

In the dual-site model,[126] the heterogeneous surface was assumed to consist of two types of sites, denoted as subscript 1 and 2. The adsorption amount (v_{m1}, v_{m2}) at each site is distributively dominated by the ratio of the site fraction (f), the difference in heat of adsorption (Q_1 and Q_2), and the temperature (T). Therefore, the redistribution of gas dsorptive preference (Figure IV. 30) can be expected under the rough condition, instead of an invariant mode:[126]

$$\frac{v_{m1}}{v_{m2}} \sim e^{(Q_2-Q_1)/RT} \qquad [4.7]$$

if (Q_2-Q_1) is small enough with proper choice of temperature range. The temperatures between 295K and 150K happen to be the transitional states, and the transitional states are able to be experimentally observed by our TRDSE work.

On the other hand, the accessibility mentioned during initial adsorption also plays an important role in this temperature dependent evolution. It is marked that some specific positions in the structures possess molecular selectivity. In HKUST-1 (presented in Figure IV. 20) the small octahedral cage was occupied with the molecules at 295K but still available at lower temperatures (even contoured at zero sigma levels). The selectivity originates from the energy barrier formed by the hydrogen atoms located near the window openings. The Arrhenius equation states that higher temperature offers CH_4 molecules more energy to overcome the activation energy barrier, explaining why we only see a large number of molecules accessing the window openings at higher

temperature. Using the same logic for PCN-306, it also can be seen that the window pockets are filled with CH_4 molecules at room temperature, because the energy barrier is easily overcome by the energetic molecules. But at lower temperatures, fewer and fewer molecules have enough kinetic energy to pass through the window openings. The above assertion can be supported by a simulation using *Materials Studio*,[107] which agrees that the energy barriers are hedged near the window openings.

Apart from being a guideline for MOF design aimed at various environments, this finding also provides a visualization of the curvature of what the Clausius-Clapeyron plot (logP v.s.T^{-1}) stands for. Conventionally, the total heat of adsorption (Q_{st}) has been assumed to be independent of temperature on account of the near linearity of Clausius-Clapeyron plot, suggesting an adsorption mode belonging to homogeneous surfaces. On the contrary, more and more instances with significant curvatures on the plot have revealed a considerable temperature coefficient of Q_{st}, which is predictively ascribed to the surface heterogeneity formed by varied energetic sites.[126]

The equilibrium state of CH_4 adsorption migrates from one type of structural feature to another upon temperature change, which implies that the heat of adsorption (Q_{ad}) in MOFs can be a function of temperature due to heterogeneous surfaces. Similar to the kinetic transition process, the thermodynamic evolution is also thought of as a molecular distribution shift, which is governed by the comprehensive concerns of both enthalpy and entropy.

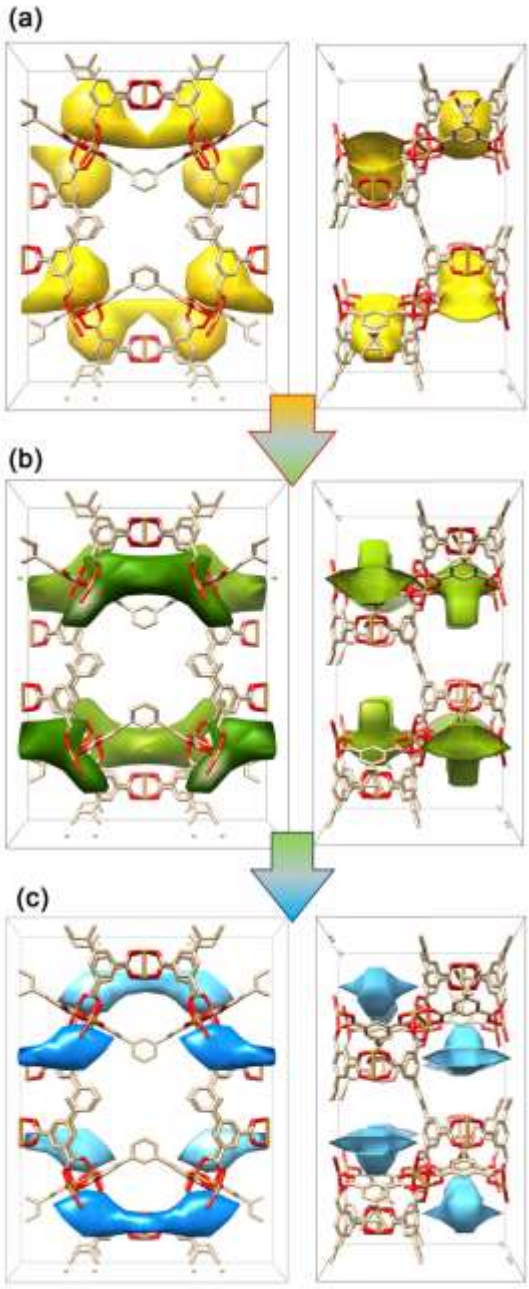

Figure IV. 30 The DED snapshots illustrate the evolution of CH_4 equilibrium states in PCN-306. The CH_4-loaded crystals were diffracted at (a) 295K, (b) 200K, (c) 150K. The right-side images, viewed along the *a*-axis, show clear different distribution around the open metal sites.

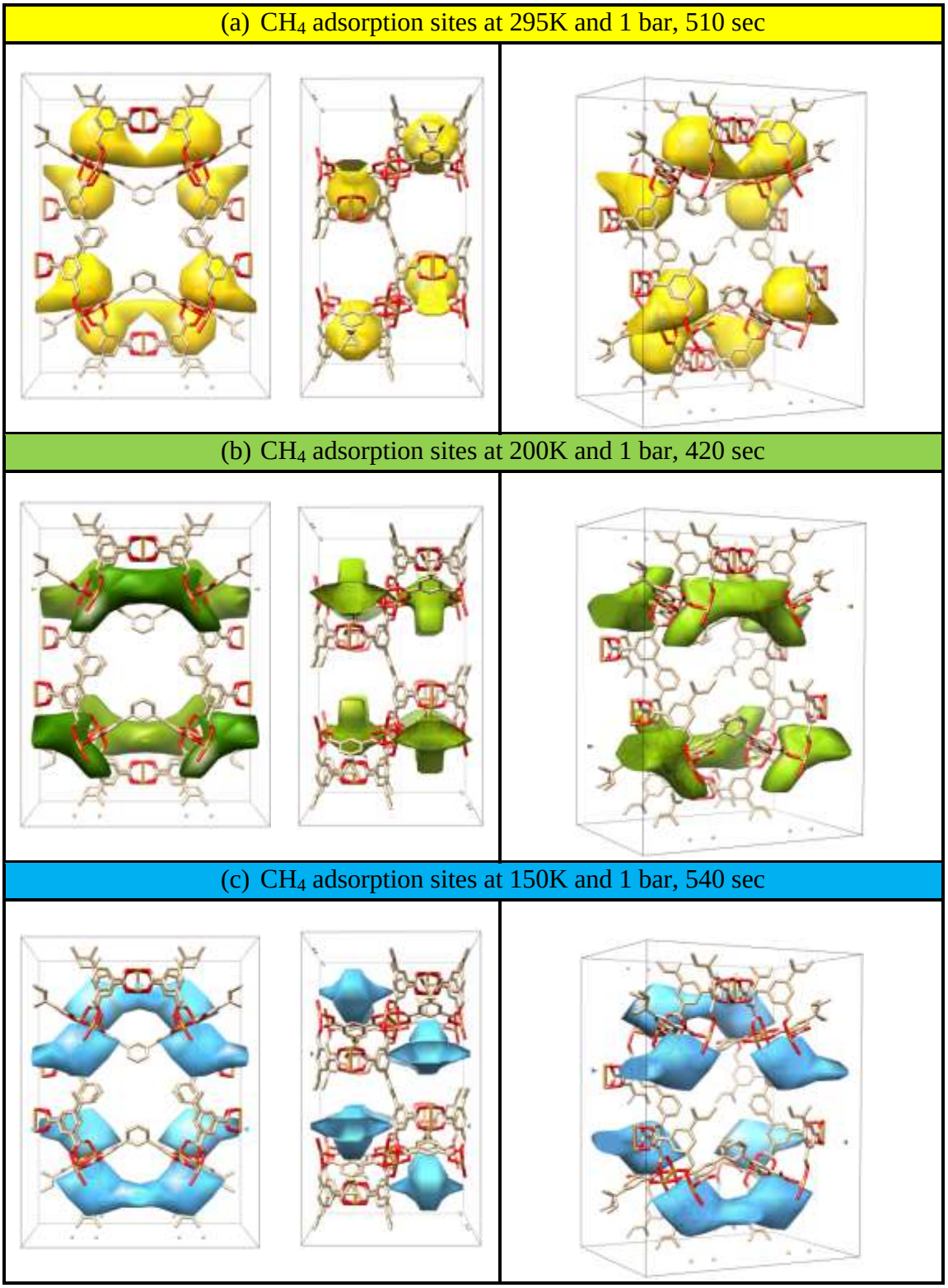

Figure IV. 31 The DED snapshots illustrate the evolution of CH_4 equilibrium states in PCN-306.

4.4.5 Gas Rearrangement at Low Temperature in MOFs

It is well known that adsorption behaviors are dependent on not only the adsorbents but the interactions of the adsorbates as well. In order to magnify the effect of gas-gas interactions, the PXRD data should be collected at lower temperature. No conspicuous changes arose until the temperature was lowered to 150K.

Also by using the DED method, we microscopically found where the CH_4 molecules were positioned. Compared with the DED map of PCN-306, it was contoured additionally near the central rhomboid space in PCN-307 where the four methyl groups build a van der Waal's force field (Figure IV. 32, right). As obtained from the crystal structures, the length and the cross section of the rhomboid cavity are 5.8Å/33.1Å^2 for PCN-306 and 3.3Å/20.3 Å^2 for PCN-307. It follows that at 150K more CH_4 molecules were boxed up in PCN-307 than in PCN-306, owing to the smaller rhomboid openings of PCN-307 against gas escape.

As shown in the *in situ* PXRD patterns (Figure IV. 32, left), there were several nascent peaks sharply growing at the 2θ angles of 12.81°, 14.81°, 16.58°, 18.17°, 21.01°, and 22.30° in the PCN-307 diffraction image (λ=0.72919Å), but none presenting at the same positions in the PCN-306 pattern. Re-indexing including these new peaks was done to check for phase transformation (or space group change). However, it suggested that two components coexist in the pattern. Compared with the plain pattern of PCN-306, new striking reflections were only presented in PCN-307 (Figure IV. 32b). Attempting to find the origin of the new peaks, we found that ordered arrangement of CH_4 is the possible species simultaneously coming with the new peaks.

Although we attached the new peaks to the CH_4 molecules arranged in an orderly fashion in the frameworks, CH_4 at the state of 150K and 1 bar should be in a fluid phase[127-128] without new striking reflections as the plain pattern of PCN-306. The nanoscale materials should not be diffracted as sharp peaks. The origin of the appearance of the new peaks is not completely explained by these hypotheses. We theorize that after achieving the critical density, pressure, and in an area of sufficient interaction with the framework, the CH_4 molecules in the largest space agglomerate to form a sizable block. The CH_4 molecules are close enough to interact with each other, and thus induced to form an ordered arrangement.

If the diffractions are induced by the ordered rearrangement of methane, it might also occur during high-pressure adsorption.[129] It potentially provides some clues on how to compact more molecules in a confined space and enhance the gas uptake. This effect of functionalization in MOFs on CH_4 storage needs further investigation in the future.

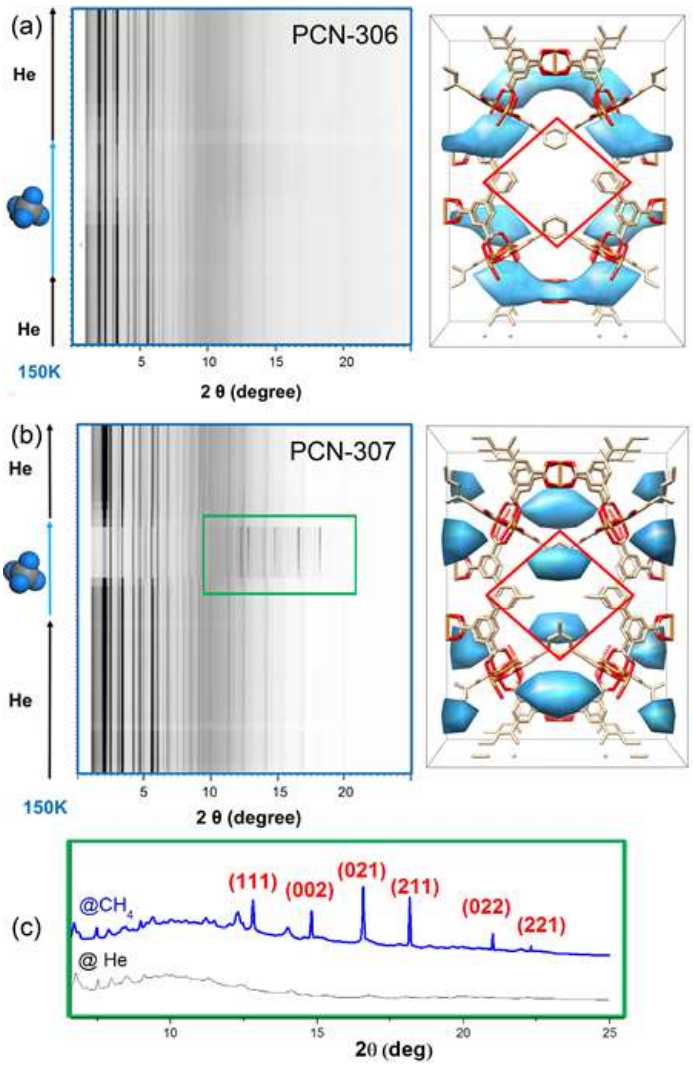

Figure IV. 32 Left of (a)(b) The top view of the *in situ* gas-loading dependent PXRD patterns for PCN-306/PCN-307 at 150K. Right of (a)(b) The corresponding DED maps for CH_4 adsorption. (c) The confined methane phase grown in PCN-307 at 150K (λ=0.72910 Å). With the help of *TOPAS 4.2*, all new reflections were indexed in (c) with a simple cubic unit cell with a=5.65Å , which is slightly shorter than a=5.88Å of the face-centred "phase I" reported in the methane phase diagram.[127-128, 130]

4.4.6 Results of CO_2 Redistribution in MOFs

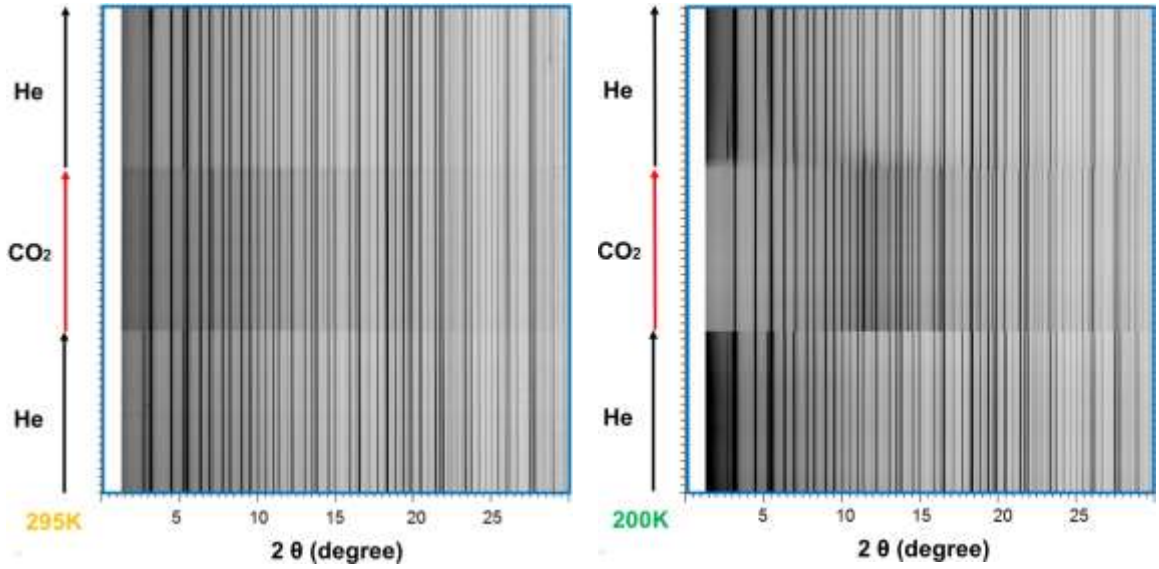

Figure IV. 33 Top view of the *in situ* gas-loading dependent PXRD patterns of activated HKUST-1, as recorded at 295K and 200K.

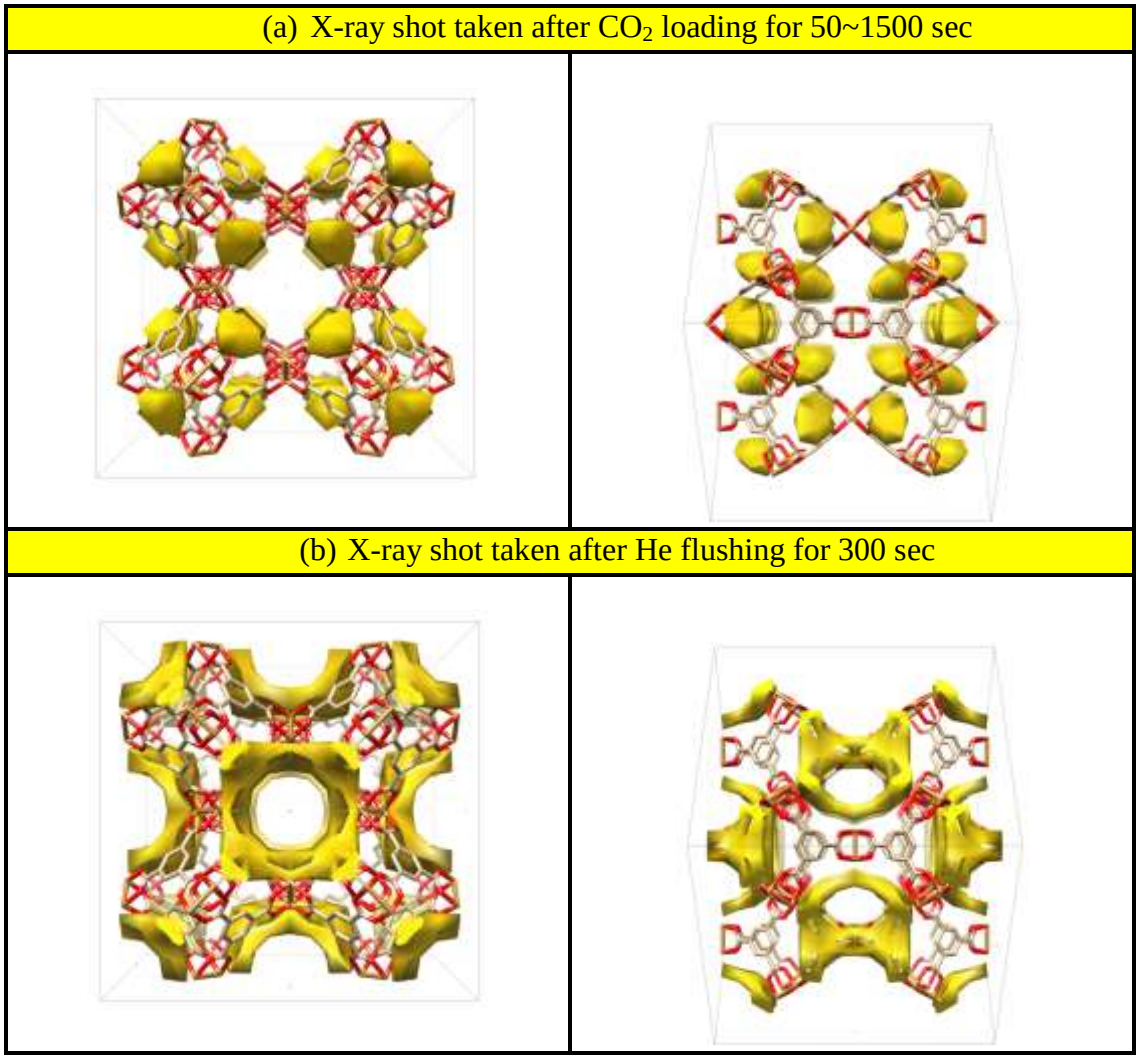

Figure IV. 34 Different perspectives of HKUST-1 and the corresponding DED maps at 295K and 1 bar.

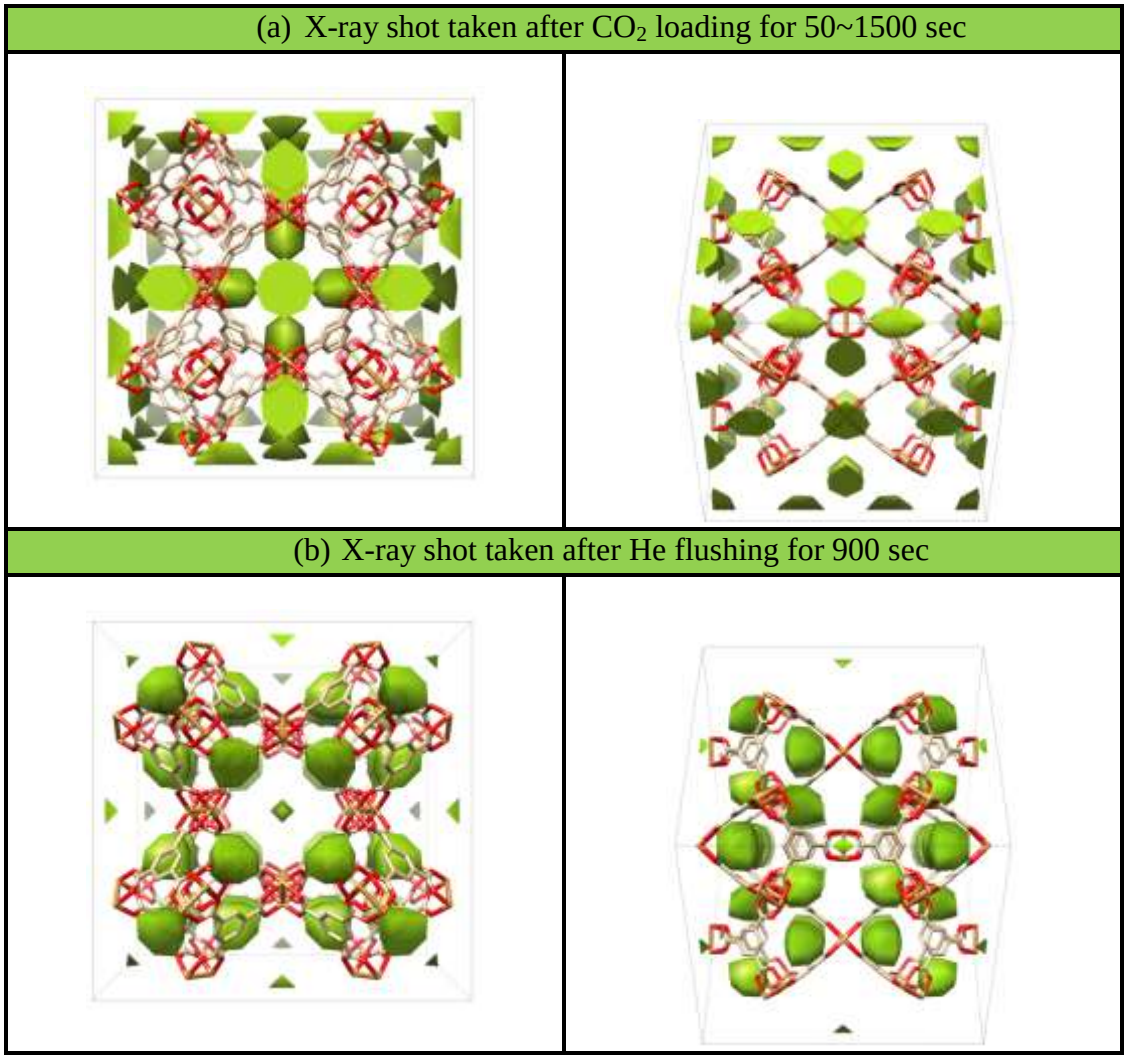

Figure IV. 35 Different perspectives of HKUST-1 and the corresponding DED maps at 200K and 1 bar.

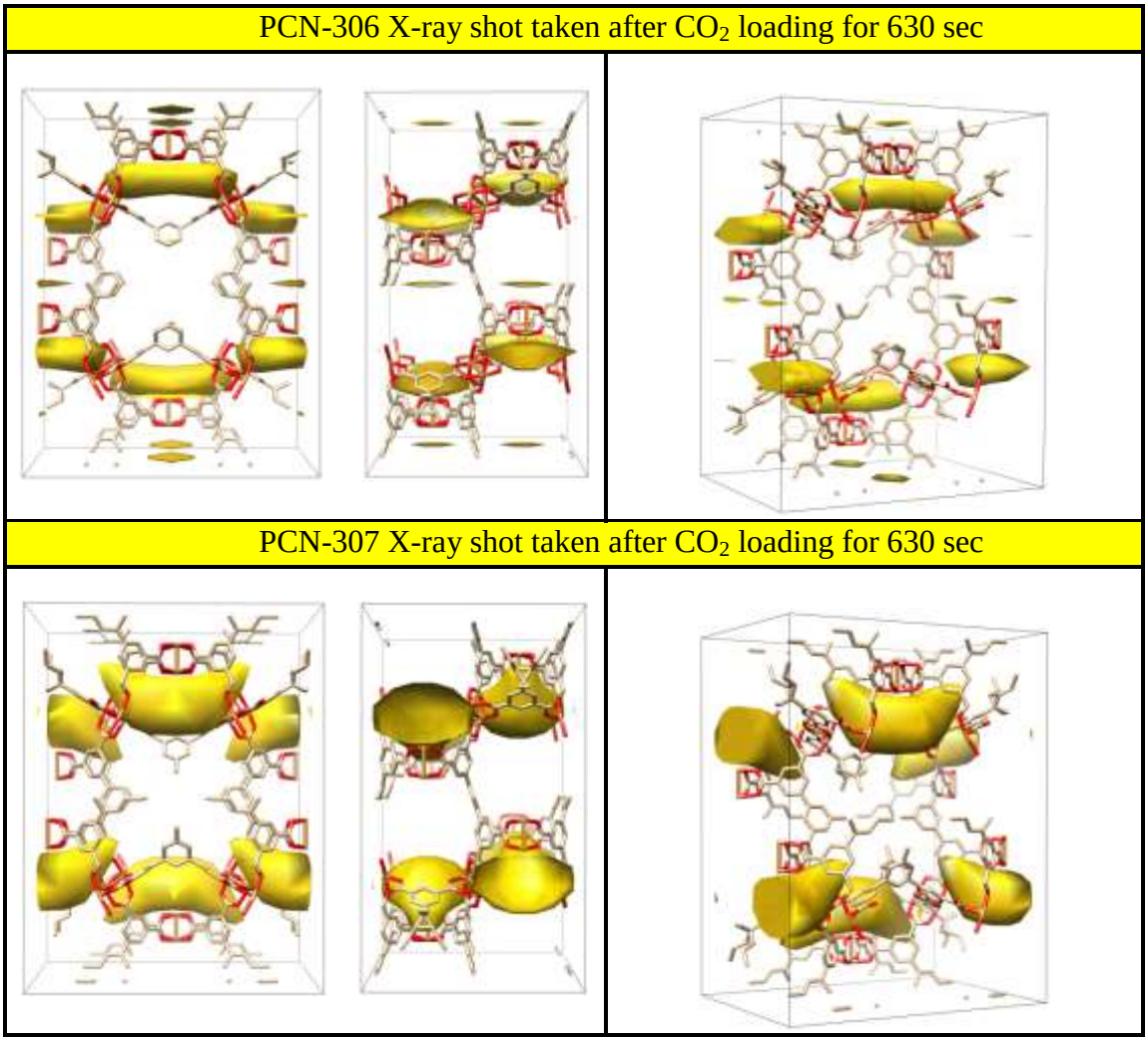

Figure IV. 36 Different perspectives of PCN-306 / PCN-307 and the corresponding DED maps at 295K and 1 bar.

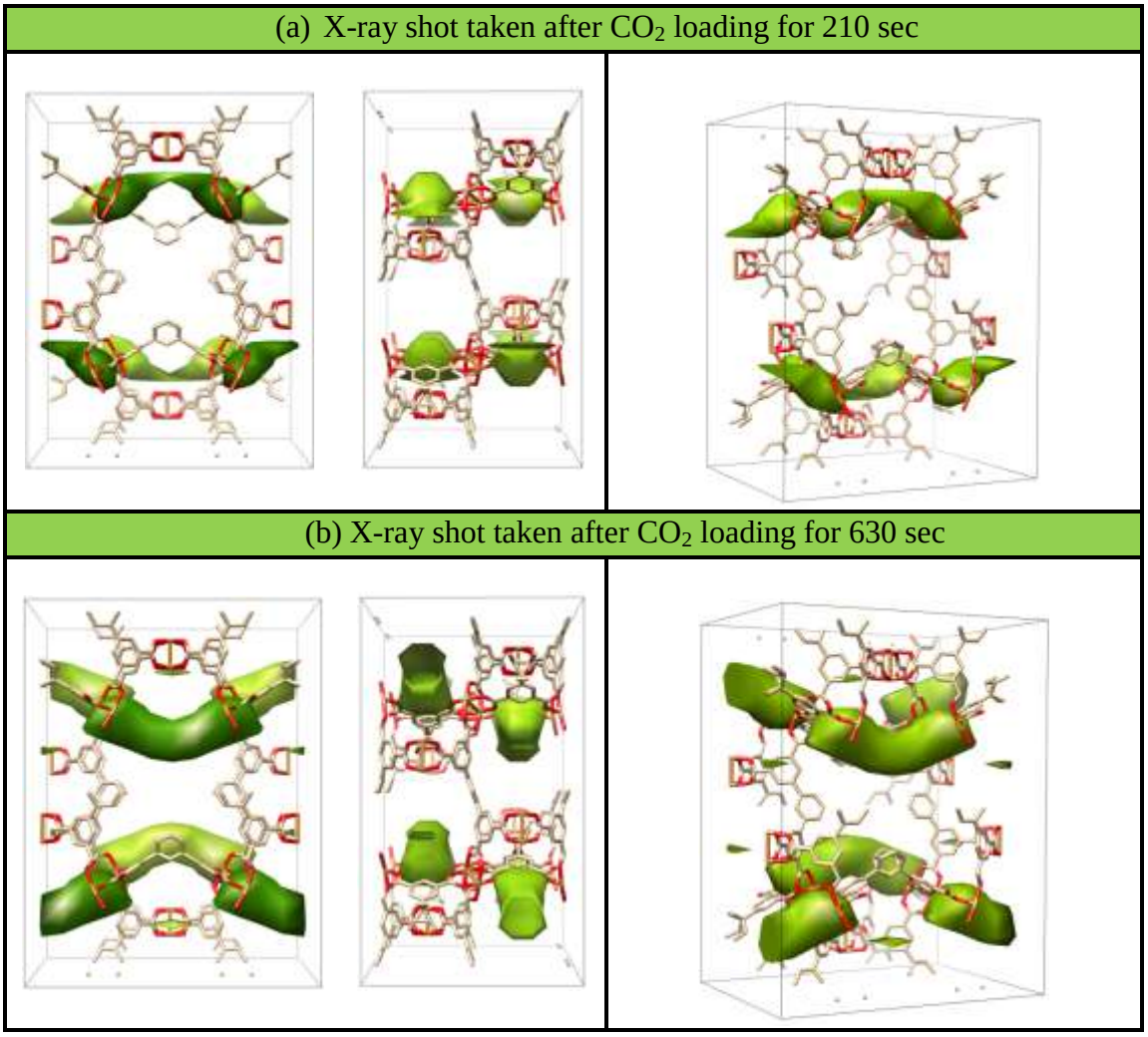

Figure IV. 37 Different perspectives of PCN-306 and the corresponding DED maps at 200K and 1 bar.

4.4.7 Demonstration for a Practical Case: Origin of Selectivity

In addition to CH_4, this TRDSE method can be applied for identification of CO_2 adsorption sites. The top view of the PXRD patterns was shown in Figure IV. 33. The similar results of DED mapping can be found in HKUST-1 (Figure IV. 34 and Figure IV. 35), and PCN-30X (Figure IV. 36 and Figure IV. 37).

PCN-306 and PCN-307 are a pair of structural analogues with comparable chemical properties (Figure IV. 3). The only structural dissimilarity is the methyl groups located on the channels along the *c*-axis (Figure IV. 38). According to the published results,[97] PCN-306/PCN-307 showed little difference in the CH_4 and CO_2 adsorption quantity but noteworthy contrast in CO_2/CH_4 selectivity. It was expected that the structure of PCN-307 featuring methyl groups was favored to select for CO_2 rather than similar CH_4 molecules. In this practical demonstration, the DED mapping was used to investigate this phenomenon. By comparing the DED snapshots of the two compounds (Figure IV. 38), a rational explanation became clear.

The strongest contours of the CO_2 density were identified around the unsaturated metal sites in both materials; but the signals in the window pockets were detected exclusively in PCN-307. In the two structures, the entrance to the window pockets is an equilateral triangle with three 5.7 Å sides. The exit from the pockets is an isosceles triangle with the shortest sides of 5.5 Å for PCN306 and 4.7 Å for PCN-307. The smaller cross section of the exit implies that PCN-307 has a pocket with less leakage, owning a better capacity to keep smaller particles inside as well. Note that the kinetic diameter of CO_2 (3.30Å) is smaller than CH_4 (3.76 Å). Additionally, the unsaturated metal sites,

acting as the first agents, adsorb CO_2 molecules faster than CH_4 molecules because of CO_2's easily induced polarization. Once transferred to the window pockets of PCN-307, the CO_2 molecules seldom escape and concurrently exclude other CH_4 molecules from moving to these thermodynamically stable sites. Not instigated by the induction and attraction of methyl groups, the higher selectivity of CO_2/CH_4 in PCN-307 arises from the proper molecular access and exit constructed by the methyl groups.

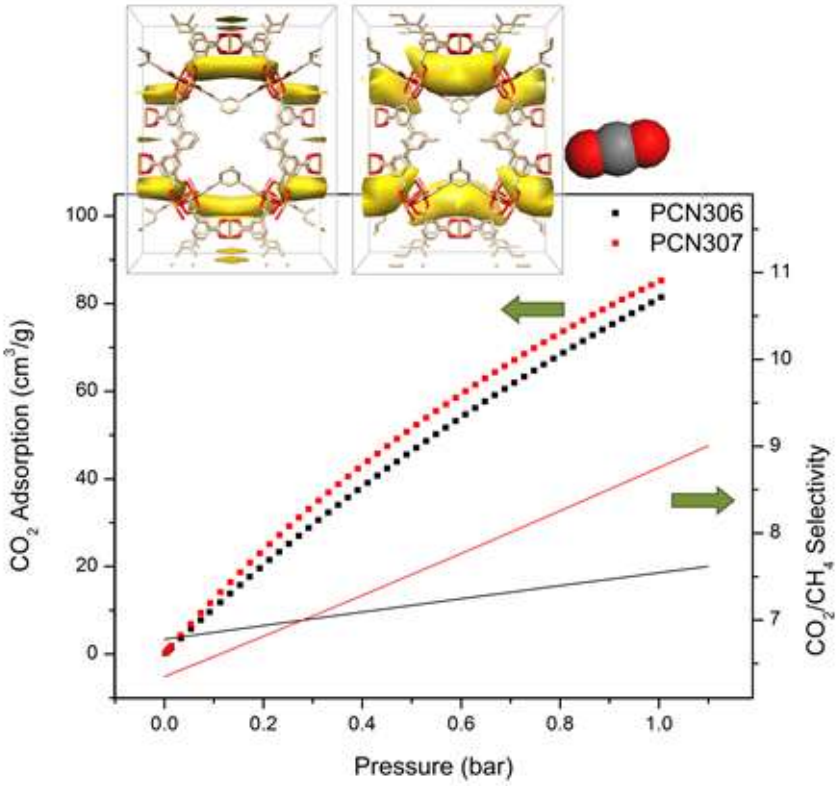

Figure IV. 38 The CO_2 sorption isotherms, the selectivity of CO_2/CH_4 and the corresponding DED maps analyzed for PCN-306/PCN-307 at 1 bar and 295K.

4.5 Conclusion

We have demonstrated a methodology using sequential *in-situ* powder X-ray diffraction measurements to observe dynamic sorption processes in MOFs. The mechanisms of initial adsorption, desorption, and gas rearrangement on temperature change are graphically explicated by the chronological DED maps, demonstrating the TRDSE method. The molecular transport from one site to another is time and temperature dependent, resulting from the enthalpy-/entropy-driven redistribution among the heterogeneous surfaces to achieve the minimum of free energy. Additionally, this method demonstrated experimentally how changes in pore window size and shape produced both temperature based pore sorption selectivity for CH_4 in HKUST-1, and explained CO_2/CH_4 selectivity changes between PCN-306 and 307.

These findings reveal the mechanisms of gas dynamics in MOFs and provide design guidance to customize MOF materials. We outlined several essentials:(i) Introducing excessive unsaturated metal units unrelated to the nodes of windows helps the adsorption kinetics upon initial gas adsorption but contributes negatively to the desorption process and overall working capacity. (ii) Both the molecular redistribution of adsorbates and the spatial accessibility of adsorbents are temperature-dependent, suggesting different positional preferences and design strategies under different temperatures. (iii) Elegant framework geometry might induce gas-gas interactions to compact more molecules, leading to higher gas uptake. (iv) Careful design of window

shape and size can produce both temperature and adsorbate-dependent adsorption selectivity in particular pores in MOFs, in a predictable and now quantifiable way.

Most importantly, the TRDSE method is generally applicable to most crystalline adsorbents, yielding information on distribution ratios of adsorbates at each type of site over time, as temperature and pressure change. It provides a possible pathway to create a MOF database containing the partial adsorption enthalpy of each structural feature. We believe that prospective architectures designed for a specific need can be assembled with possible features selected in the database before hands-on experiments.

CHAPTER V

SUMMARY

Metal-organic polyhedra (MOPs) are a family of isolated molecular self-assemblies with crystalline arrangements, which can be regarded as a bunch of nano-sized containers. In a bio-system, we do not want to see single drug molecule react with each other before transporting to target positions. This confined space of the nano-sized container can separate single drug molecule in different cavity. In this work, we reported a series of MOPs derived from Cu_2 and Mo_2 paddlewheel units and multiple conformers of organic linkers, 3,3'-PDBAD (L^1) and its positional isomer 4,4´- PDBAD (L^2). Temperature modulation, metal units and ligand configurations (bridging angles) lead to 5 MOP formations. Among them, a unique MOP in MOP assembly is a very rare example in MOP field. Site-selective metal exchange in this new structure was also discovered. The site-specific metal substitution provides a good synthetic strategy to broaden the structural diversity and avoids difficulties accessing through the direct synthesis processes.

Besides bio-applications, MOP itself can be considered a design concept. Guest molecules like to be trapped in a cavity possessing similar dimensions. Therefore, we can construct a pre-designed MOP with desired shape/size to selectively target a single molecule. After that, achieving the realisation to include MOPs into MOFs, a new MOF with desired geometry and topology can be formed. Consequently, this design strategy, called Superpolyhedral Building Blocks strategy, was carried out to obtain a MOF with

impressive BET surface area and CO_2 uptake, finding an alternative to inconvenient synthetic processes and to achieve desired structural features.

In order to reduce carbon emissions of the greenhouse gas pollution that warms our planet, methane has been considered an alternative clean energy source. At current stage in development of methane-powered vehicles, one of the challenges comes from the storage capacity of the tank. To maximize the methane uptake with a smallest tank volume, Metal-Organic Frameworks (MOFs) are a family of advanced porous compounds, which can largely increase surface area in the tank for adsorbing gas molecules.

Since MOF structures are highly tailorable for specific applications, perceiving which structural characteristics in MOFs contribute to high methane uptake is very important in the material design. In practical situations, methane molecules do not stay in the storage tank forever. Instead, they go in and out of the tank within a dynamic working cycle. Also, the environmental conditions do not always keep constant. The favored adsorption sites in the host materials might be changed with varied temperature and pressure. While the previous studies are focused on the static states of gas adsorption by using computational calculations, my proposed TRDSE method allows people to observe the gas molecular motions in MOFs at various conditions.

This time-resolved diffraction structure envelope (TRDSE) method has been developed using *in situ* synchrotron powder X-ray diffraction and a customized gas-loaded cell. The MOF powders are packed in a capillary installed on the gas cell where various gas atmospheres can be controlled. At the same time, X-ray exposures

sequentially took a shot on the gas-loaded MOFs. A series of powder X-ray diffraction patterns were recorded under various gas-loading time and temperatures.

From the obtained PXRD patterns, it showed that the diffraction intensity was increased or decreased depending on the different gas-loading time or temperature. The electron density of adsorbed gas molecules can be visualized after Fourier transform. Thus we can see which structural characteristic is favored by the gas molecules. This gives experimental researchers a direction to design their materials for higher methane uptake.

Furthermore, interesting gas kinetic processes were observed in several MOF platforms by TRDSE method: infusion, desorption, and gas redistribution on temperature change. Previously, people thought gas molecules are statically absorbed on attractive sites in host materials. However, we found that the gas molecules firstly arrive at open metal sites and then migrate to larger neighboring spaces upon gas infusion. This guest migration in host MOF materials is the first-seen observation in the literature to my best knowledge. My analysis results also showed that gas molecules favor to redistribute over many types of sites rather than to exclusively occupy the strongest binding sites. Besides MOFs, this TRDSE method can be used for other crystalline materials, which shows its applicability and generality.

REFERENCES

1. He, Y. B.; Zhou, W.; Qian, G. D.; Chen, B. L., Methane storage in metal-organic frameworks. *Chemical Society Reviews* **2014,** *43* (16), 5657-5678.
2. Li, J.-R.; Yu, J.; Lu, W.; Sun, L.-B.; Sculley, J.; Balbuena, P. B.; Zhou, H.-C., Porous materials with pre-designed single-molecule traps for CO_2 selective adsorption. *Nature Communications* **2013,** *4*, 1538-1545.
3. Deng, H.; Grunder, S.; Cordova, K. E.; Valente, C.; Furukawa, H.; Hmadeh, M.; Gándara, F.; Whalley, A. C.; Liu, Z.; Asahina, S.; Kazumori, H.; O'Keeffe, M.; Terasaki, O.; Stoddart, J. F.; Yaghi, O. M., Large-pore apertures in a series of metal-organic frameworks. *Science* **2012,** *336* (6084), 1018-1023.
4. Lu, W.; Yuan, D.; Makal, T. A.; Wei, Z.; Li, J.-R.; Zhou, H.-C., Highly porous metal-organic framework sustained with 12-connected nanoscopic octahedra. *Dalton Transactions* **2013,** *42* (5), 1708-1714.
5. Perry Iv, J. J.; Perman, J. A.; Zaworotko, M. J., Design and synthesis of metal-organic frameworks using metal-organic polyhedra as supermolecular building blocks. *Chemical Society Reviews* **2009,** *38* (5), 1400-1417.
6. Young, M. D.; Zhang, Q.; Zhou, H.-C., Metal–organic polyhedra constructed from dinuclear ruthenium paddlewheels. *Inorganica Chimica Acta* **2015,** *424* (0), 216-220.
7. Yuan, D.; Zhao, D.; Sun, D.; Zhou, H.-C., An isoreticular series of metal–organic frameworks with dendritic hexacarboxylate ligands and exceptionally high gas-

uptake capacity. *Angewandte Chemie International Edition* **2010,** *49* (31), 5357-5361.

8. Li, J.-R.; Timmons, D. J.; Zhou, H.-C., Interconversion between molecular polyhedra and metal−organic frameworks. *Journal of the American Chemical Society* **2009,** *131* (18), 6368-6369.

9. Liu, T.-F.; Zou, L.; Feng, D.; Chen, Y.-P.; Fordham, S.; Wang, X.; Liu, Y.; Zhou, H.-C., Stepwise synthesis of robust metal–organic frameworks via postsynthetic metathesis and oxidation of metal nodes in a single-crystal to single-crystal transformation. *Journal of the American Chemical Society* **2014,** *136* (22), 7813-7816.

10. Sheldrick, G. M., A short history of SHELX. *Acta Crystallographica Section A* **2008,** *64*, 112-122.

11. van der Sluis, P.; Spek, A. L., BYPASS: an effective method for the refinement of crystal structures containing disordered solvent regions. *Acta Crystallographica Section A* **1990,** *46* (3), 194-201.

12. Macrae, C. F.; Edgington, P. R.; McCabe, P.; Pidcock, E.; Shields, G. P.; Taylor, R.; Towler, M.; van De Streek, J., Mercury: visualization and analysis of crystal structures. *Journal of Applied Crystallography* **2006,** *39*, 453-457.

13. Lin, X.; Jia, J.; Zhao, X.; Thomas, K. M.; Blake, A. J.; Walker, G. S.; Champness, N. R.; Hubberstey, P.; Schröder, M., High H_2 adsorption by coordination-framework materials. *Angewandte Chemie International Edition* **2006,** *45* (44), 7358-7364.

14. Li, M.; Li, D.; O'Keeffe, M.; Yaghi, O. M., Topological analysis of metal–organic frameworks with polytopic linkers and/or multiple building units and the minimal transitivity principle. *Chemical Reviews* **2014,** *114* (2), 1343-1370.

15. Millward, A. R.; Yaghi, O. M., Metal-organic frameworks with exceptionally high capacity for storage of carbon dioxide at room temperature. *Journal of the American Chemical Society* **2005,** *127* (51), 17998-17999.

16. Bao, Z. B.; Yu, L. A.; Ren, Q. L.; Lu, X. Y.; Deng, S. G., Adsorption of CO_2 and CH_4 on a magnesium-based metal organic framework. *Journal of Colloid and Interface Science* **2011,** *353* (2), 549-556.

17. Kim, J.; Yang, S. T.; Choi, S. B.; Sim, J.; Kim, J.; Ahn, W. S., Control of catenation in CuTATB-n metal-organic frameworks by sonochemical synthesis and its effect on CO_2 adsorption. *Journal of Materials Chemistry* **2011,** *21* (9), 3070-3076.

18. McDonald, T. M.; D'Alessandro, D. M.; Krishna, R.; Long, J. R., Enhanced carbon dioxide capture upon incorporation of N,N '-dimethylethylenediamine in the metal-organic framework CuBTTri. *Chemical Science* **2011,** *2* (10), 2022-2028.

19. Chen, Y.-P.; Liu, Y.; Liu, D.; Bosch, M.; Zhou, H.-C., Direct measurement of adsorbed gas redistribution in metal–organic frameworks. *Journal of the American Chemical Society* **2015,** *137* (8), 2919-2930.

20. Fujita, M.; Yazaki, J.; Ogura, K., Preparation of a macrocyclic polynuclear complex, $[(en)Pd(4,4'\text{-bpy})]_4(NO_3)_8$ (en = ethylenediamine, bpy = bipyridine),

which recognizes an organic molecule in aqueous media. *Journal of the American Chemical Society* **1990,** *112* (14), 5645-5647.

21. Chakrabarty, R.; Mukherjee, P. S.; Stang, P. J., Supramolecular coordination: self-assembly of finite two- and three-dimensional ensembles. *Chemical Reviews* **2011,** *111* (11), 6810-6918.

22. Cook, T. R.; Zheng, Y.-R.; Stang, P. J., Metal–organic frameworks and self-assembled supramolecular coordination complexes: comparing and contrasting the design, synthesis, and functionality of metal–organic materials. *Chemical Reviews* **2012,** *113* (1), 734-777.

23. Sun, Q.-F.; Sato, S.; Fujita, M., An $M_{18}L_{24}$ stellated cuboctahedron through post-stellation of an $M_{12}L_{24}$ core. *Nature Chemistry* **2012,** *4* (4), 330-333.

24. Han, Y.; Li, J.-R.; Xie, Y.; Guo, G., Substitution reactions in metal-organic frameworks and metal-organic polyhedra. *Chemical Society Reviews* **2014,** *43* (16), 5952-5981.

25. Tranchemontagne, D. J.; Ni, Z.; O'Keeffe, M.; Yaghi, O. M., Reticular chemistry of metal–organic polyhedra. *Angewandte Chemie International Edition* **2008,** *47* (28), 5136-5147.

26. Prakash, M. J.; Lah, M. S., Metal-organic macrocycles, metal-organic polyhedra and metal-organic frameworks. *Chemical Communications* **2009,** (23), 3326-3341.

27. Hamilton, T. D.; Papaefstathiou, G. S.; Friščić, T.; Bučar, D.-K. i.; MacGillivray, L. R., Onion-shell metal−organic polyhedra (MOPs): a general approach to

decorate the exteriors of MOPs using principles of supramolecular chemistry. *Journal of the American Chemical Society* **2008,** *130* (44), 14366-14367.

28. Fang, Y.; Murase, T.; Sato, S.; Fujita, M., Noncovalent tailoring of the binding pocket of self-assembled cages by remote bulky ancillary groups. *Journal of the American Chemical Society* **2012,** *135*, 613–615.

29. Schmidtendorf, M.; Pape, T.; Hahn, F. E., Stepwise Preparation of a molecular square from NR,NR- and NH,O-substituted dicarbene building blocks. *Angewandte Chemie International Edition* **2012,** *51* (9), 2195-2198.

30. Nakamura, T.; Ube, H.; Shiro, M.; Shionoya, M., A Self-ssembled multiporphyrin cage complex through three different zinc(II) center formation under well-balanced aqueous conditions. *Angewandte Chemie International Edition* **2013,** *52* (2), 720-723.

31. Clegg, J. K.; Cremers, J.; Hogben, A. J.; Breiner, B.; Smulders, M. M. J.; Thoburn, J. D.; Nitschke, J. R., A stimuli responsive system of self-assembled anion-binding $Fe_4L_6^{8+}$ cages. *Chemical Science* **2013,** *4* (1), 68-76.

32. Pluth, M. D.; Bergman, R. G.; Raymond, K. N., Acid catalysis in basic solution: a supramolecular host promotes orthoformate hydrolysis. *Science* **2007,** *316* (5821), 85-88.

33. Pluth, M. D.; Bergman, R. G.; Raymond, K. N., Catalytic deprotection of acetals in basic solution with a self-assembled supramolecular "nanozyme". *Angewandte Chemie International Edition* **2007,** *46* (45), 8587-8589.

34. Hastings, C. J.; Pluth, M. D.; Bergman, R. G.; Raymond, K. N., Enzymelike catalysis of the Nazarov cyclization by supramolecular encapsulation. *Journal of the American Chemical Society* **2010,** *132* (20), 6938-6940.

35. Brown, C. J.; Miller, G. M.; Johnson, M. W.; Bergman, R. G.; Raymond, K. N., High-turnover supramolecular catalysis by a protected ruthenium(II) complex in aqueous solution. *Journal of the American Chemical Society* **2011,** *133* (31), 11964-11966.

36. Lu, W.; Yuan, D.; Yakovenko, A.; Zhou, H.-C., Surface functionalization of metal-organic polyhedron for homogeneous cyclopropanation catalysis. *Chemical Communications* **2011,** *47* (17), 4968-4970.

37. Kumazawa, K.; Biradha, K.; Kusukawa, T.; Okano, T.; Fujita, M., Multicomponent assembly of a pyrazine-pillared coordination cage that selectively binds planar guests by intercalation. *Angewandte Chemie* **2003,** *115* (33), 4039-4043.

38. Yoshizawa, M.; Tamura, M.; Fujita, M., Diels-Alder in aqueous molecular hosts: unusual regioselectivity and efficient catalysis. *Science* **2006,** *312* (5771), 251-254.

39. Smulders, M. M. J.; Jiménez, A.; Nitschke, J. R., Integrative self-sorting synthesis of a $Fe_8Pt_6L_{24}$ cubic cage. *Angewandte Chemie International Edition* **2012,** *51* (27), 6681-6685.

40. Yoshizawa, M.; Klosterman, J. K.; Fujita, M., Functional molecular flasks: new properties and reactions within discrete, self-assembled hosts. *Angewandte Chemie International Edition* **2009,** *48* (19), 3418-3438.

41. Osuga, T.; Murase, T.; Fujita, M., Triple-decker Au_3–Ag–Au_3–Ag–Au_3 ion cluster enclosed in a self-assembled cage. *Angewandte Chemie International Edition* **2012,** *51* (49), 12199-12201.

42. Mal, P.; Breiner, B.; Rissanen, K.; Nitschke, J. R., White phosphorus is air-stable within a self-assembled tetrahedral capsule. *Science* **2009,** *324* (5935), 1697-1699.

43. Ni, Z.; Yassar, A.; Antoun, T.; Yaghi, O. M., Porous metal-organic truncated octahedron constructed from paddle-wheel squares and terthiophene links. *Journal of the American Chemical Society* **2005,** *127* (37), 12752-12753.

44. Northrop, B. H.; Zheng, Y.-R.; Chi, K.-W.; Stang, P. J., Self-organization in coordination-driven self-assembly. *Accounts of Chemical Research* **2009,** *42* (10), 1554-1563.

45. Cotton, F. A.; Lin, C.; Murillo, C. A., Supramolecular arrays based on dimetal building units. *Accounts of Chemical Research* **2001,** *34* (10), 759-771.

46. Eddaoudi, M.; Kim, J.; Wachter, J. B.; Chae, H. K.; O'Keeffe, M.; Yaghi, O. M., Porous metal-organic polyhedra: 25 Å cuboctahedron constructed from 12 $Cu_2(CO_2)_4$ paddle-wheel building blocks. *Journal of the American Chemical Society* **2001,** *123* (18), 4368-4369.

47. Smulders, M. M. J.; Riddell, I. A.; Browne, C.; Nitschke, J. R., Building on architectural principles for three-dimensional metallosupramolecular construction. *Chemical Society Reviews* **2013,** *42* (4), 1728-1754.

48. Li, J.-R.; Zhou, H.-C., Bridging-ligand-substitution strategy for the preparation of metal-organic polyhedra. *Naure Chemistry* **2010,** *2* (10), 893-898.

49. Li, J.-R.; Zhou, H.-C., Metal-organic hendecahedra assembled from dinuclear paddlewheel nodes and mixtures of ditopic linkers with 120 and 90° bend Angles. *Angewandte Chemie International Edition* **2009,** *48* (45), 8465-8468.

50. Marcus Frederick Charles Ladd, R. A. P., Structure determination by X-ray crystallography. **2003**, 187-90.

51. Yuan, Z.; Zhao, J.; Wang, Z.-X., Flexibility analysis of enzyme active sites by crystallographic temperature factors. *Protein Engineering* **2003,** *16* (2), 109-114.

52. Friedman, R.; Caflisch, A., Pepsinogen-like activation intermediate of plasmepsin II revealed by molecular dynamics analysis. *Proteins: Structure, Function, and Bioinformatics* **2008,** *73* (4), 814-827.

53. Gana, R.; Rao, S.; Huang, H.; Wu, C.; Vasudevan, S., Structural and functional studies of S-adenosyl-L-methionine binding proteins: a ligand-centric approach. *BMC Structural Biology 13* (1), 6-19.

54. Kokkinidis, M.; Glykos, N. M.; Fadouloglou, V. E.; Christo, C.; Tatyana, K.-C., Chapter 7 - Protein flexibility and enzymatic catalysis. In *Advances in Protein Chemistry and Structural Biology*, Academic Press: Vol. 87, 181-218.

55. Eyal, E.; Chennubhotla, C.; Yang, L.-W.; Bahar, I., Anisotropic fluctuations of amino acids in protein structures: insights from X-ray crystallography and elastic network models. *Bioinformatics* **2007,** *23* (13), i175-i184.

56. Cui, X.; Khlobystov, A. N.; Chen, X.; Marsh, D. H.; Blake, A. J.; Lewis, W.; Champness, N. R.; Roberts, C. J.; Schröder, M., Dynamic equilibria in solvent-mediated anion, cation and ligand exchange in transition-metal coordination polymers: solid-state transfer or recrystallisation? *Chemistry - A European Journal* **2009,** *15* (35), 8861-8873.

57. Aime, S.; Botta, M.; Fasano, M.; Marques, M. P. M.; Geraldes, C. F. G. C.; Pubanz, D.; Merbach, A. E., Conformational and coordination equilibria on DOTA complexes of lanthanide metal ions in aqueous solution studied by ^{1}H-NMR spectroscopy. *Inorganic Chemistry* **1997,** *36* (10), 2059-2068.

58. Friedman, R.; Caflisch, A., Pepsinogen-like activation intermediate of plasmepsin II revealed by molecular dynamics analysis. *Proteins: Structure, Function, and Bioinformatics* **2008,** *73* (4), 814-827.

59. Yuan, Z.; Zhao, J.; Wang, Z.-X., Flexibility analysis of enzyme active sites by crystallographic temperature factors. *Protein Engineering* **2003,** *16* (2), 109-114.

60. Gana, R.; Rao, S.; Huang, H.; Wu, C.; Vasudevan, S., Structural and functional studies of S-adenosyl-L-methionine binding proteins: a ligand-centric approach. *BMC Structural Biology* **2013,** *13* (1), 6-20.

61. Sasai, H.; Arai, T.; Satow, Y.; Houk, K. N.; Shibasaki, M., The first heterobimetallic multifunctional asymmetric catalyst. *Journal of the American Chemical Society* **1995,** *117* (23), 6194-6198.

62. Anaya de Parrodi, C.; Walsh, P. J., All kinds of reactivity: recent breakthroughs in metal-catalyzed alkyne chemistry. *Angewandte Chemie International Edition* **2009,** *48* (26), 4679-4682.

63. Li, J.-R.; Ma, Y.; McCarthy, M. C.; Sculley, J.; Yu, J.; Jeong, H.-K.; Balbuena, P. B.; Zhou, H.-C., Carbon dioxide capture-related gas adsorption and separation in metal-organic frameworks. *Coordination Chemistry Reviews* **2011,** *255*, 1791-1823.

64. Makal, T. A.; Li, J. R.; Lu, W.; Zhou, H. C., Methane storage in advanced porous materials. *Chemical Society reviews* **2012,** *41* (23), 7761-79.

65. Zhang, M.; Bosch, M.; Gentle Iii, T.; Zhou, H.-C., Rational design of metal-organic frameworks with anticipated porosities and functionalities. *Crystal Engineering Communication* **2014,** *16* (20), 4069-4083.

66. Rowsell, J. L.; Spencer, E. C.; Eckert, J.; Howard, J. A.; Yaghi, O. M., Gas adsorption sites in a large-pore metal-organic framework. *Science* **2005,** *309* (5739), 1350-4.

67. Vaidhyanathan, R.; Iremonger, S. S.; Shimizu, G. K. H.; Boyd, P. G.; Alavi, S.; Woo, T. K., Direct observation and quantification of CO_2 binding within an amine-functionalized nanoporous solid. *Science* **2010,** *330* (6004), 650-653.

68. Zhou, C.; Cao, L.; Wei, S.; Zhang, Q.; Chen, L., A first principles study of gas adsorption on charged CuBTC. *Computational and Theoretical Chemistry* **2011,** *976*, 153-160.

69. Xiang, S.; Zhou, W.; Gallegos, J. M.; Liu, Y.; Chen, B., Exceptionally high acetylene uptake in a microporous metal−organic framework with open metal sites. *Journal of the American Chemical Society* **2009,** *131* (34), 12415-12419.

70. Cui, P.; Ma, Y. G.; Li, H. H.; Zhao, B.; Li, J. R.; Cheng, P.; Balbuena, P. B.; Zhou, H. C., Multipoint interactions enhanced CO_2 uptake: a zeolite-like zinc-tetrazole framework with 24-nuclear zinc cages. *Journal of the American Chemical Society* **2012,** *134* (46), 18892-18895.

71. Xu, Q.; Liu, D.; Yang, Q.; Zhong, C.; Mi, J., Li-modified metal-organic frameworks for CO_2/CH_4 separation: a route to achieving high adsorption selectivity. *Journal of Materials Chemistry* **2010,** *20* (4), 706-714.

72. Grajciar, L. s.; Wiersum, A. D.; Llewellyn, P. L.; Chang, J.-S.; Nachtigall, P., Understanding CO_2 adsorption in CuBTC MOF: comparing combined DFT-ab initio calculations with microcalorimetry experiments. *The Journal of Physical Chemistry C* **2011,** *115* (36), 17925-17933.

73. Wu, H.; Simmons, J. M.; Liu, Y.; Brown, C. M.; Wang, X.-S.; Ma, S.; Peterson, V. K.; Southon, P. D.; Kepert, C. J.; Zhou, H.-C.; Yildirim, T.; Zhou, W., Metal-organic frameworks with exceptionally high methane uptake: where and how is methane stored? *Chemistry – A European Journal* **2010,** *16* (17), 5205-5214.

74. Duren, T.; Bae, Y. S.; Snurr, R. Q., Using molecular simulation to characterise metal-organic frameworks for adsorption applications. *Chemical Society reviews* **2009,** *38* (5), 1237-1247.

75. Liu, D.; Zhong, C., Understanding gas separation in metal-organic frameworks using computer modeling. *Journal of Materials Chemistry* **2010,** *20* (46), 10308-10318.

76. Dubbeldam, D.; Frost, H.; Walton, K. S.; Snurr, R. Q., Molecular simulation of adsorption sites of light gases in the metal-organic framework IRMOF-1. *Fluid Phase Equilibria* **2007,** *261*, 152-161.

77. Wu, H.; Zhou, W.; Yildirim, T., Methane sorption in nanoporous metal-organic frameworks and first-order phase transition of confined methane. *The Journal of Physical Chemistry C* **2009,** *113* (7), 3029-3035.

78. Wu, H.; Zhou, W.; Yildirim, T., High-capacity methane storage in metal-organic frameworks M_2(dhtp): the important role of open metal sites. *Journal of the American Chemical Society* **2009,** *131* (13), 4995-5000.

79. Getzschmann, J.; Senkovska, I.; Wallacher, D.; Tovar, M.; Fairen-Jimenez, D.; Düren, T.; van Baten, J. M.; Krishna, R.; Kaskel, S., Methane storage mechanism in the metal-organic framework $Cu_3(btc)_2$: an in situ neutron diffraction study. *Microporous and Mesoporous Materials* **2010,** *136*, 50-58.

80. Hulvey, Z.; Lawler, K. V.; Qiao, Z.; Zhou, J.; Fairen-Jimenez, D.; Snurr, R. Q.; Ushakov, S. V.; Navrotsky, A.; Brown, C. M.; Forster, P. M., Noble gas

adsorption in copper trimesate, HKUST-1: an experimental and computational study. *The Journal of Physical Chemistry C* **2013,** *117* (39), 20116-20126.

81. Yildirim, T.; Hartman, M., Direct observation of hydrogen adsorption sites and nanocage formation in metal-organic frameworks. *Physical Review Letters* **2005,** *95* (21).

82. Wu, H.; Zhou, W.; Yildirim, T., Hydrogen storage in a prototypical zeolitic imidazolate framework-8. *Journal of the American Chemical Society* **2007,** *129* (17), 5314-5315.

83. Peterson, V. K.; Liu, Y.; Brown, C. M.; Kepert, C. J., Neutron powder diffraction study of D_2 sorption in Cu_3(1,3,5-benzenetricarboxylate)$_2$. *Journal of the American Chemical Society* **2006,** *128* (49), 15578-15579.

84. Peterson, V. K.; Brown, C. M.; Liu, Y.; Kepert, C. J., Structural study of D_2 within the trimodal pore system of a metal organic framework. *The Journal of Physical Chemistry C* **2011,** *115* (17), 8851-8857.

85. Lee, H.; Choi, Y. N.; Choi, S. B.; Seo, J. H.; Kim, J.; Cho, I. H.; Gang, S.; Jeon, C. H., In situ neutron powder diffraction and X-ray photoelectron spectroscopy analyses on the hydrogenation of MOF-5 by Pt-doped multiwalled carbon nanotubes. *The Journal of Physical Chemistry C* **2014,** *118* (11), 5691-5699.

86. Carrington, E. J.; Vitorica-Yrezabal, I. J.; Brammer, L., Crystallographic studies of gas sorption in metal-organic frameworks. *Acta crystallographica Section B: Structural science* **2014,** *70*, 404-422.

87. Yakovenko, A. A.; Wei, Z.; Wriedt, M.; Li, J.-R.; Halder, G. J.; Zhou, H.-C., Study of guest molecules in metal-organic frameworks by powder X-ray diffraction: analysis of difference envelope density. *Crystal Growth & Design* **2014,** *14* (11), 5397-5407.

88. von Schnering, H. G.; Nesper, R., How nature adapts chemical structures to curved surfaces. *Angewandte Chemie, International Edition* **1987,** *26* (11), 1059-1080.

89. Mackay, A. L., Periodic minimal surfaces. *Nature* **1985,** *314* (6012), 604-606.

90. Andersson, S.; Hyde, S. T.; Larsson, K.; Lidin, S., Minimal surfaces and structures: from inorganic and metal crystals to cell membranes and biopolymers. *Chemical Reviews* **1988,** *88* (1), 221-242.

91. Brenner, S.; McCusker, L. B.; Baerlocher, C., Using a structure envelope to facilitate structure solution from powder diffraction data. *Journal of Applied Crystallography* **1997,** *30* (6), 1167-1172.

92. von Schnering, H. G.; Nesper, R., Nodal surfaces of Fourier series: fundamental invariants of structured matter. *Z. Physik B - Condensed Matter* **1991,** *83* (3), 407-412.

93. Yakovenko, A. A.; Reibenspies, J. H.; Bhuvanesh, N.; Zhou, H.-C., Generation and applications of structure envelopes for porous metal-organic frameworks. *Journal of Applied Crystallography* **2013,** *46* (2), 346-353.

94. Serre, C.; Bourrelly, S.; Vimont, A.; Ramsahye, N. A.; Maurin, G.; Llewellyn, P. L.; Daturi, M.; Filinchuk, Y.; Leynaud, O.; Barnes, P.; Férey, G., An explanation

for the very large breathing effect of a metal-organic framework during CO_2 adsorption. *Advanced Materials* **2007,** *19* (17), 2246-2251.

95. Chui, S. S., A chemically functionalizable nanoporous material $[Cu_3(TMA)_2(H_2O)_3]_n$. *Science* **1999,** *283* (5405), 1148-1150.

96. Wang, X.-S.; Ma, S.; Forster, P. M.; Yuan, D.; Eckert, J.; López, J. J.; Murphy, B. J.; Parise, J. B.; Zhou, H.-C., Enhancing H_2 uptake by "close-packing" alignment of open copper sites in metal-organic frameworks. *Angewandte Chemie International Edition* **2008,** *47* (38), 7263-7266.

97. Liu, Y.; Li, J.-R.; Verdegaal, W. M.; Liu, T.-F.; Zhou, H.-C., Isostructural metal-organic frameworks assembled from functionalized diisophthalate ligands through a ligand-truncation strategy. *Chemistry – A European Journal* **2013,** *19* (18), 5637-5643.

98. Chupas, P. J.; Chapman, K. W.; Kurtz, C.; Hanson, J. C.; Lee, P. L.; Grey, C. P., A versatile sample-environment cell for non-ambient X-ray scattering experiments. *Journal of Applied Crystallography* **2008,** *41* (4), 822-824.

99. Petříček, V.; Dušek, M.; Palatinus, L., Crystallographic computing system JANA2006: general features. *Zeitschrift fur Kristallographie* **2014,** *229* (5), 345.

100. Cox, D. E.; Hastings, J. B.; Thomlinson, W.; Prewitt, C. T., Application of synchrotron radiation to high resolution powder diffraction and Rietveld refinement. *Nuclear Instruments and Methods in Physics Research* **1983,** *208*, 573-578.

101. Brenner, S.; McCusker, L. B.; Baerlocher, C., The application of structure envelopes in structure determination from powder diffraction data. *Journal of Applied Crystallography* **2002,** *35* (2), 243-252.

102. Palatinus, L.; Chapuis, G., SUPERFLIP– a computer program for the solution of crystal structures by charge flipping in arbitrary dimensions. *Journal of Applied Crystallography* **2007,** *40* (4), 786-790.

103. Pettersen, E. F.; Goddard, T. D.; Huang, C. C.; Couch, G. S.; Greenblatt, D. M.; Meng, E. C.; Ferrin, T. E., UCSF Chimera--a visualization system for exploratory research and analysis. *Journal of computational chemistry* **2004,** *25* (13), 1605-1612.

104. Goddard, T. D.; Huang, C. C.; Ferrin, T. E., Visualizing density maps with UCSF Chimera. *Journal of structural biology* **2007,** *157* (1), 281-287.

105. Michalska, K. Electron density maps and their interpretation. http://www.man.poznan.pl/CBB/CWICZENIA/CHEM/SERP-4/practical-4.html.

106. For example, contours at a sigma level of 1 would depict a closed surface which wraps grid points possessing $\rho(x,y,z)$ values greater than one standard deviation unit above the mean. Understandably, lower sigma level would increase the volume built by the closed surface and give more noises; in contrast, higher sigma level would decrease the volume and eliminate much significant information.

107. Accelerys, *Materials Studio Release Notes, Release 5.5.1*. Accelrys Software, Inc.: San Diego, 2010.

108. Casewit, C. J.; Colwell, K. S.; Rappe, A. K., Application of a universal force field to organic molecules. *Journal of the American Chemical Society* **1992,** *114* (25), 10035-10046.

109. Casewit, C. J.; Colwell, K. S.; Rappe, A. K., Application of a universal force field to main group compounds. *Journal of the American Chemical Society* **1992,** *114* (25), 10046-10053.

110. Rappe, A. K.; Casewit, C. J.; Colwell, K. S.; Goddard, W. A.; Skiff, W. M., UFF, A full periodic table force field for molecular mechanics and molecular dynamics simulations. *Journal of the American Chemical Society* **1992,** *114* (25), 10024-10035.

111. Rappe, A. K.; Colwell, K. S.; Casewit, C. J., Application of a universal force field to metal complexes. *Inorganic Chemistry* **1993,** *32* (16), 3438-3450.

112. D. Frenkel, B. S., *Understanding Molecular Simulation: From Algorithms to Applications*. Academic Press: San Diego, CA, 2002.

113. Note that the DED maps were contoured at a relative cut-off level (sigma unit), not an absolute cut-off level (e/Å ^{3}). We only can say the primary adsorption sites are changed from open metal sites to window sites. But we cannot say the methane molecules break away from the open metal sites and transfer to the window sites. Here we stated that the methane molecules migrate from open metal sites to windows because we confirmed the absolute cut-off level at 0.003 and found that the volume of the electron clouds at open metal sites was indeed decreased.

114. Lucena, S. M.; Mileo, P. G.; Silvino, P. F.; Cavalcante, C. L., Jr., Unusual adsorption site behavior in PCN-14 metal-organic framework predicted from Monte Carlo simulation. *Journal of the American Chemical Society* **2011,** *133* (48), 19282-5.

115. George, A. R.; Catlow, C. R. A.; Thomas, J. M., A computational investigation of the sorption of methane into zeolitic structures. *Microporous Materials* **1997,** *11*, 97-105.

116. For the case of PCN-12, the gas adsorption did not reach the equilibrium yet. But for that of PCN-306, we found the electron density is almost unchanged, even it was contoured at the absolute levels of electron density.

117. Mason, J. A.; Veenstra, M.; Long, J. R., Evaluating metal-organic frameworks for natural gas storage. *Chemical Science* **2014,** *5* (1), 32.

118. Lyklema, J., Modified statistical treatment of partially mobile adsorbates. *Journal of the Chemical Society, Faraday Transactions 2* **1977,** *73* (7), 1646-1650.

119. Al-Muhtaseb, S. A.; Ritter, J. A., A statistical mechanical perspective on the temperature dependence of the isosteric heat of adsorption and adsorbed phase heat capacity. *The Journal of Physical Chemistry B* **1999,** *103* (38), 8104-8115.

120. Hill, T. L., Statistical mechanics of multimolecular adsorption II. Localized and mobile adsorption and absorption. *The Journal of Chemical Physics* **1946,** *14* (7), 441-453.

121. Livingston, H. K., The cross-sectional areas of molecules adsorbed on solid surfaces. *Journal of Colloid Science* **1949,** *4* (5), 447-458.

122. Note that CO_2 molecules can be detected at the open metal sites and small octahedral cages by contouring lower than 1 sigma, which are minor adsorption sites for CO_2 adsorption.

123. Peng, Y.; Krungleviciute, V.; Eryazici, I.; Hupp, J. T.; Farha, O. K.; Yildirim, T., Methane storage in metal-organic frameworks: current records, surprise findings, and challenges. *Journal of the American Chemical Society* **2013,** *135* (32), 11887-11894.

124. Krawiec, P.; Kramer, M.; Sabo, M.; Kunschke, R.; Fröde, H.; Kaskel, S., Improved hydrogen storage in the metal-organic framework $Cu_3(BTC)_2$. *Advanced Engineering Materials* **2006,** *8* (4), 293-296.

125. Vishnyakov, A.; Ravikovitch, P. I.; Neimark, A. V.; Bülow, M.; Wang, Q. M., Nanopore structure and sorption properties of Cu-BTC metal-organic framework. *Nano Letters* **2003,** *3* (6), 713-718.

126. Huang, Y.-Y., The temperature dependence of isosteric heat of adsorption on the heterogeneous surface. *Journal of Catalysis* **1972,** *25* (1), 131-138.

127. Bini, R.; Pratesi, G., High-pressure infrared study of solid methane: phase diagram up to 30 GPa. *Physical Review B* **1997,** *55* (22), 14800-14809.

128. Hazen, R. M.; Mao, H. K.; Finger, L. W.; Bell, P. M., Structure and compression of crystalline methane at high pressure and room temperature. *Applied Physics Letters* **1980,** *37* (3), 288.

129. Lachet, V.; Boutin, A.; Pellenq, R. J. M.; Nicholson, D.; Fuchs, A. H., Molecular simulation study of the structural rearrangement of methane adsorbed in aluminophosphate $AlPO_4$-5. *Journal of Physical Chemistry* **1996,** *100* (21), 9006-9013.

130. Press, W., Structure and phase transitions of solid heavy methane (CD_4). *The Journal of Chemical Physics* **1972,** *56* (6), 2597.